



Statistical Physics of Water in Hydrophobic Nano-Confinement and at Proteins Interfaces

Valentino Bianco

ADVERTIMENT. La consulta d'aquesta tesi queda condicionada a l'acceptació de les següents condicions d'ús: La difusió d'aquesta tesi per mitjà del servei TDX (www.tdx.cat) i a través del Dipòsit Digital de la UB (diposit.ub.edu) ha estat autoritzada pels titulars dels drets de propietat intel·lectual únicament per a usos privats emmarcats en activitats d'investigació i docència. No s'autoritza la seva reproducció amb finalitats de lucre ni la seva difusió i posada a disposició des d'un lloc aliè al servei TDX ni al Dipòsit Digital de la UB. No s'autoritza la presentació del seu contingut en una finestra o marc aliè a TDX o al Dipòsit Digital de la UB (framing). Aquesta reserva de drets afecta tant al resum de presentació de la tesi com als seus continguts. En la utilització o cita de parts de la tesi és obligat indicar el nom de la persona autora.

ADVERTENCIA. La consulta de esta tesis queda condicionada a la aceptación de las siguientes condiciones de uso: La difusión de esta tesis por medio del servicio TDR (www.tdx.cat) y a través del Repositorio Digital de la UB (diposit.ub.edu) ha sido autorizada por los titulares de los derechos de propiedad intelectual únicamente para usos privados enmarcados en actividades de investigación y docencia. No se autoriza su reproducción con finalidades de lucro ni su difusión y puesta a disposición desde un sitio ajeno al servicio TDR o al Repositorio Digital de la UB. No se autoriza la presentación de su contenido en una ventana o marco ajeno a TDR o al Repositorio Digital de la UB (framing). Esta reserva de derechos afecta tanto al resumen de presentación de la tesis como a sus contenidos. En la utilización o cita de partes de la tesis es obligado indicar el nombre de la persona autora.

WARNING. On having consulted this thesis you're accepting the following use conditions: Spreading this thesis by the TDX (www.tdx.cat) service and by the UB Digital Repository (diposit.ub.edu) has been authorized by the titular of the intellectual property rights only for private uses placed in investigation and teaching activities. Reproduction with lucrative aims is not authorized nor its spreading and availability from a site foreign to the TDX service or to the UB Digital Repository. Introducing its content in a window or frame foreign to the TDX service or to the UB Digital Repository is not authorized (framing). Those rights affect to the presentation summary of the thesis as well as to its contents. In the using or citation of parts of the thesis it's obliged to indicate the name of the author.

Statistical Physics of Water in Hydrophobic Nano-Confinement and at Proteins Interfaces

Valentino Bianco

Tesis Doctoral

Programa de Doctorado en Física

Departament de Física Fonamental

Facultat de Física Universitat de Barcelona

2013

Supervisor Dr. Giancarlo Franzese

... to Ginevra.

Contents

Abstract	1
Resumen en Castellano	3
1 Introduction on water	7
1.1 Importance of water	7
1.2 Polymorphism and polyamorphism	8
1.3 Different scenarios for supercooled water behavior	10
1.4 State of the art on hydration water at low temperature	13
2 A coarse-grain model for a confined water monolayer	17
2.1 The need of coarse-grain approach	17
2.2 The model	18
2.2.1 Coarse grain of the volume	19
2.2.2 Isotropic interaction	19
2.2.3 Directional HB interaction	20
2.2.4 HB cooperativity	21
2.2.5 Volume dependence on HBs	22
2.3 Monte Carlo simulation	23
2.3.1 Metropolis algorithm	24
2.3.2 Wolff algorithm	25
2.3.3 Internal units	27
3 Thermodynamic results	29
3.1 TMD line and Spinodals	29
3.2 Thermodynamic response functions	31
3.2.1 Isothermal compressibility	31
3.2.2 Isobaric specific heat	33
3.2.3 Thermal expansion coefficient	35
3.3 The Widom line	37
3.4 The Liquid-Liquid 1 st order phase transition and the Liquid-Liquid critical point	39

4	Percolation approach to supercooled water	47
4.1	Site-bond correlated percolation	48
4.2	Percolation probability	51
4.3	Cluster distribution	54
4.4	Mean cluster size	58
4.5	Connectivity length	60
4.6	Scaling analysis	62
5	Role of interfacial HBs on protein stability	65
5.1	Overview on protein stability	65
5.1.1	Thermodynamics of proteins unfolding	66
5.1.2	Protein phase diagram	67
5.2	Models for protein unfolding	70
5.2.1	Hydrophobic effect	70
5.2.2	Pressure effects	74
5.3	Coarse-graining the water-water interaction at protein interface	74
5.3.1	Monte Carlo algorithm	77
5.4	Phase diagram of a solvated homopolymer	78
5.4.1	Tune of strength of interfacial HB and hydration shell density	82
6	Conclusions	87
	Appendix A: Usefull thermodynamic relations	89
	Appendix B: Theory of scaling fields	91
	Appendix C: Histogram reweighting method	95
	Bibliography	95
	Curriculum Vitae	119

List of abbreviations

HB	hydrogen bond
HDL	high-density liquid
LDL	low-density liquid
LG	liquid-gas
LL	liquid-liquid
LLCP	liquid-liquid critical point
MC	monte carlo
n.n.	next neighbor
SR	stability region
TMD	temperature of maximum density

Abstract

Water is commonly associated with life. This substance affects the living beings in countless aspects and length scales, ranging from molecular biology to climatology. Water exhibits a long series of anomalous behaviors. These anomalies can be rationalized as a consequence of a second critical point in the supercooled region of the liquid phase. Nevertheless, the large part of the phase diagram of supercooled water is to date experimentally inaccessible for the inevitable crystallization of the bulk liquid. Confinement of water in nano-structures is a possible way to prevent the crystallization of molecules.

In this thesis we present a coarse-grain model to describe the physical behavior of water at hydrophobic interfaces. The essential feature of the model is the description of water-water interaction via directional and cooperative components of the hydrogen bond (HB). We explore the phase diagram of supercooled water nanoconfined between hydrophobic walls. Our results, grounded in statistical physics methods and Monte Carlo simulations, show the presence of a line of first order phase transition in the temperature-pressure plane separating two liquid phases and ending in a liquid-liquid critical point (LLCP). The LLCP universality class approaches the one of the Ising model in two dimensions in the thermodynamic limit, while large deviations are observed for strong confinement. Below the LLCP we find the locus of maxima of correlation length (the Widom line) of the system. Near the LLCP we find a large increase of the thermodynamic response functions consistent with the anomalous behaviors of water.

These predictions are confirmed by a percolation description of water molecules based on the definition of cluster of correlated degrees of freedom. Along the phase transition line and the Widom line we recover a power law cluster distribution. At the LLCP the scaling of the percolation quantities agree with the Ising critical exponents.

The density, energy and entropy fluctuations that are at the base of the anomalies of water and the existence of its LLCP have also consequences in the context of protein stability. General thermodynamic prediction asserts the existence of a close stability region (SR) in temperature-pressure plane for the native folded state of a protein. Experimental

evidences support this theory showing hot-, cold- and pressure-denaturation. Water behavior at the protein interface is expected to be the driving force for the folding-unfolding process. To shed light on this mechanism we study the SR of a folded hydrophobic polymer solvated in the coarse-grain water. Tuning the water-water interaction at the interface and the density of the hydration shell we find an elliptic protein SR in the temperature-pressure plane, qualitatively consistent with available experimental data. Our work contributes to the ongoing debate about the role of hydration water in stabilizing the native protein state. We show here that the physics of water, and in particular its energy, density and entropy fluctuations are sufficient to rationalize the existence of a protein SR with respect to temperature and pressure.

Resumen en Castellano

El agua recubre 2/3 de la Tierra, afecta su clima y morfología, es fundamental en muchas tecnologías y disuelve casi todas las sustancias químicas, por lo menos en parte. A pesar de ser la sustancia más corrosiva, es fisiológicamente inocua y es el componente principal de los seres vivos: el 60% del peso del cuerpo humano de un adulto se debe a su contenido de agua. La mayor parte de este porcentaje de agua se encuentra confinada en las células, y la restante fluye en la sangre y en estrechos canales debajo de los tejidos finos. Muchos seres vivos necesitan agua debido al hecho que ésta participa en la mayoría de los procesos biológicos: en el metabolismo de los nutrientes y su transporte a los tejidos, en la eliminación de los residuos celulares y en la comunicación entre células. Datos recientes demuestran que la dinámica del agua desarrolla un papel fundamental en los procesos biológicos, como la determinación de la tasa de plegamiento de las proteínas.

A pesar de su importancia y abundancia, y de innumerables estudios, su comportamiento sigue siendo difícil de entender respecto a los fluidos simples, del tipo argón. El agua tiene más de sesenta anomalías. Por ejemplo, su fluidez aumenta al aumentar la presión y su densidad disminuye al bajar la temperatura; tiene una capacidad extraordinaria de absorber calor, esencial para regular la temperatura de máquinas, de nuestro cuerpo y del planeta mismo. Su capacidad calorífica y su compresibilidad presentan un mínimo en 35°C y 46°C respectivamente, y ambas aumentan al bajar la temperatura como si fueran divergentes a una temperatura alrededor de -45°C, así como su expansividad térmica que se hace negativa debajo de 0°C. El agua puede permanecer líquida, en un estado metaestable a temperaturas tan bajas como -20°C en insectos, -37°C en gotas suspendidas en las nubes y -47°C en plantas. Además en laboratorio es posible observar el agua sobreenfriada a -41°C a presión atmosférica y a -92°C a 2 kbar.

Entre las posibles explicaciones de este comportamiento anómalo encontramos cuatro teorías básicas

- El escenario del límite de estabilidad, que está fundado sobre la hipótesis de un

cambio de la pendiente de la espinodal líquido-gas, de positiva a altas temperaturas a negativa a bajas temperatura.

- El escenario del punto crítico líquido-líquido, que supone la existencia de una transición de fase del primer orden entre dos líquidos metaestables en la región súper-enfriada. Esta transición acaba en un punto crítico líquido-líquido.
- El escenario sin singularidad, que relaciona el incremento anómalo de la compresibilidad con el comportamiento de la línea de temperatura de máxima densidad.
- El escenario sin punto crítico, que se basa en la existencia de una transición de fase orden-desorden, con una posible discontinuidad en la densidad, que se extiende a presión negativa hasta el límite de estabilidad del agua sobre-enfriada.

Los objetivos de esta tesis son: i) explorar el diagrama de fases de baja temperatura de aguas confinadas; ii) investigar el comportamiento del agua de hidratación en la interfaz con proteínas; iii) analizar como la region de estabilidad de las proteínas depende de las interacciones interfaciales. Conforme a esto hemos desarrollado un modelo de grano-grueso capaz de captar algunas características microscópicas de la interacción agua-agua in una interfaz hidrofobicas que permiten entender el papel del agua en la estabilidad de las proteínas.

Resultados obtenidos

A continuación, mostramos una lista de todos los resultados principales obtenidos en esta tesis. La mayoría de los resultados se obtuvieron utilizando simulaciones Monte Carlo

En el capítulo 3, hemos analizado el diagrama de fases por baja temperatura de una mono-capa de agua confinada entre paredes paralelas hidrófobas. Hemos calculado las líneas de temperatura de máxima y mínima densidad, y la región donde se encuentra el máximo de la longitud de correlación, que define la línea de Widom. Encontramos dos líneas de extremos para cada función de respuesta termodinámicas: una línea, a baja temperatura, de extremos más fuerte, que se solapa con la línea Widom, otra línea, a alta temperatura, de extremos más débiles. Esos resultados están de acuerdo con resultados experimentales y validan el modelo. Encontramos un punto crítico líquido-líquido en la región sobre-enfriada, al final de una línea de transición de primer orden entre dos fases líquidas que se caracterizan por diferentes valores de la energía y densidad. El punto crítico pertenece a la clase de universalidad Ising en dos dimensiones sólo por tamaño de las paredes muy grandes.

Sorprendentemente, reduciendo el tamaño de la monocapa confinada sin variar la distancia entre las paredes, es decir aumentando el confinamiento, la clase de universalidad desvia hacia la de Ising en tres dimensiones. Este efecto es debido a (i) la elevada cooperatividad de la red de puentes de hidrogeno y (ii) a su bajo número de coordinación a bajas temperaturas que hace que la monocapa tenga un comportamiento similar a lo del agua no confinada dentro de la primera capa de coordinación.

En el capítulo 4, presentamos una descripción geométrica de la región de moléculas correladas en la monocapa sobreenfriada. Los clusters de moléculas están construidas siguiendo el enfoque de percolación propuesto por Kastelein-Fortuin y Coniglio-Klein. La probabilidad de que dos moléculas pertenezcan al mismo grupo depende de las condiciones termodinámicas de temperatura y presión. Nuestros resultados enseñan que la línea de transición líquido-líquido y la línea Widom se caracterizan por una línea de percolación, donde la distribución de los clúster decae según ley de potencia. Esta línea marca la región donde las fluctuaciones de puentes de hidrogeno se extienden por toda la red. A baja presión la percolación está relacionada con la reordenación tetraédrica local de la red de puentes de hidrogeno. A alta presión la línea de percolación se asocia a la rápida formación de puentes de hidrogeno, dando lugar a discontinuidad en la densidad, asociado a la transición de fase líquido-líquido. Los análisis de las cantidades de percolación en la región crítica confirman la existencia de un punto crítico que pertenece a la clase de universalidad de Ising en dos dimensiones.

En el capítulo 5, hemos adoptado el modelo de grano-grueso en el contexto de plegamiento de proteínas. Sin entrar en el complejo mecanismo de plegamiento de proteínas hemos estudiado cómo la red de puentes de hidrogeno puede estabilizar el estado nativo de una proteína. Los elementos fundamentales del modelo son: la variación de la interacción agua-agua en la interfaz hidrofóbica, el aumento de densidad del agua interfacial al aumentar la presión. El modelo muestra que la proteína se desnatura a alta temperatura, a baja temperatura, a alta presión y a baja presión, reproduciendo las características de desnaturación observadas en los experimentos. La región de estabilidad de la proteína, tiene una forma elíptica de acuerdo con la teoría. Hemos estudiado por fin la dependencia de la región de estabilidad de los parámetros, encontrando que la variación de la energía de puentes de hidrogeno a la interfaz y la compresibilidad de la capa de hidratación son mecanismos fundamentales para reproducir una región de estabilidad cerrada en el plano temperatura-presión.

Chapter 1

Introduction on water

1.1 Importance of water

Water covers 2/3 of the Earth, affect its climate and morphology, it is critical in many technologies and dissolves almost all chemicals, at least in part [1]. Despite being the most corrosive substance, it is physiologically harmless and is the main component of living beings: approximately 60% by weight of an adult human body is due to its water content. Most of this water ($\simeq 60\%$) are confined in cells, while the remaining water flows below tissues and in narrow blood vessels [2,3]. Living beings need water because it is involved in most biological processes: in the metabolism of nutrients and their transport to the tissues, in the disposal of cellular waste, and in the communication between cells [4]. Enzymes and proteins need to be suspended in solution to change their conformation and to adopt their active structures, and water governs the rate of recognition that proteins, nucleic acids and membranes have of ligands and drugs [5]. Our failure in fully understanding the behavior of water is one of the main limitation we have in predicting protein structures and in designing drugs. For example, recent data show that the dynamics of water plays a fundamental role in biological processes, such as determining the proteins-folding rate [6]. Also, the hydrophobic collapse of proteins and the rapid folding of their secondary structure are mediated by the water molecules that are in the proximity of the amino acids [7]. Other examples come from the protein-protein interactions that are affected by the dynamics of the hydration-water layer [8].

Despite its importance and countless studies, the behavior of water remains poorly understood with respect to simple fluids, such as argon [9]. Water has more than sixty anomalies. For example, its diffusion increases with increasing pressure and its density decreases with decreasing temperature below 4 °C. As a consequence, the ice floats on

liquid water and lakes freeze from the top when the outside temperature goes down, while water at 4 °C sinks toward the bottom allowing the fish to keep swimming and living. Water has, also, an extraordinary capacity to absorb heat, essential for regulating the temperature of engines, of our body and of our planet [10]. Again, this property is essential for the life in cold waters, because it makes water, near freezing, not much susceptible to temperature changes, keeping the bottoms of lakes at 4 °C despite the outside temperature can go far below 0 °C, thanks to the ice layer on the surface.

The anomalous behavior of heat transfer and volume changes in water is emphasized by its heat capacity and compressibility that have a minimum at 35 °C and 46 °C, respectively. Both quantities increase upon decreasing temperature as if they were diverging at a temperature around -45 °C [10]. Furthermore, its thermal expansion coefficient turns negative below 0 °C [10] (Fig. 1.1).

Another peculiar property of water is that, contrary to what we could think, water does not freeze easily at 0 °C and tends to stay liquid at moderately negative temperatures. How far below 0 °C water can remain liquid in a *supercooled*, metastable state depends on several conditions. For example, water can be liquid at temperatures as low as -20 °C when confined in insects bodies, or -37 °C in the drops forming the clouds [11], or -47 °C when confined in plants [12]. The best records for bulk are achieved in laboratory where it is possible to observe supercooled water at -41 °C at atmospheric pressure [13] and at -92 °C at 2 kbar [14].

1.2 Polymorphism and polyamorphism

The possible explanations for this anomalous behavior are numerous and controversial [15]. It is clear that the main characteristic of the molecules of H₂O is its ability to form hydrogen bonds (HB), but the very definition of this type of bond is controversial as much as its experimental measurement [16]. The common understanding is that on average each molecule forms four HBs, each with very short life-time in a such a way that they are continuously formed and broken while water molecules diffuse in the liquid phase.

These bonds strengthen the attraction among molecules, resulting in values for the melting point, boiling point and enthalpy of vaporisation of H₂O higher than what would be expected by comparing with hydrides of elements in the same groups as O, i.e. S, Se, and Te [16]. Being the typical bond distance smaller than the van der Waals radius, the formation of HBs implies a balance among dispersive forces—at their repulsive distance—and

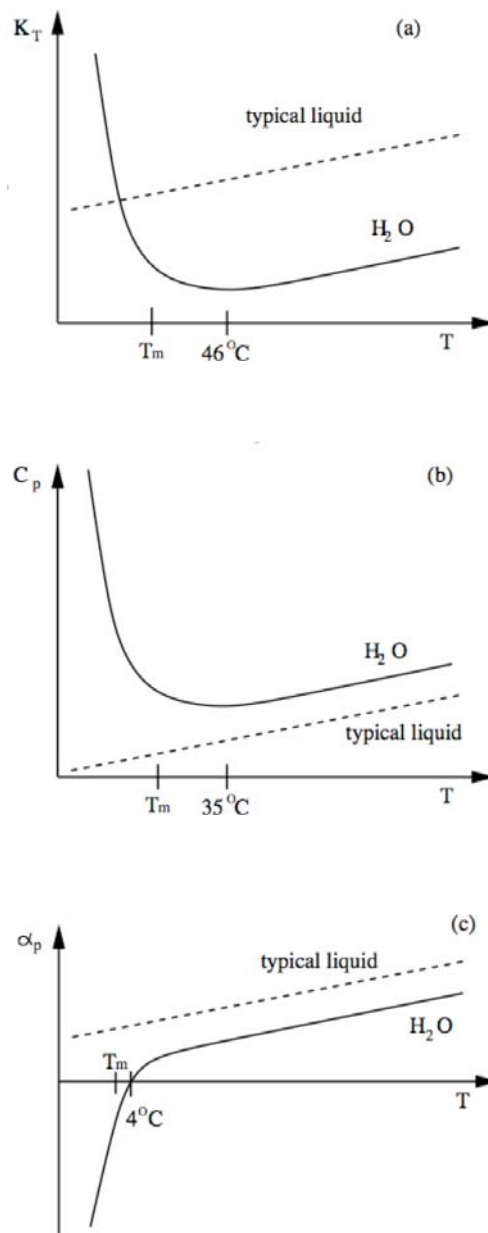


Figure 1.1: Schematic dependence on temperature at atmospheric pressure of (a) the isothermal compressibility $K_T \equiv -(1/V)(\partial V/\partial P)_T$ proportional to fluctuations of molar volume, (b) the specific heat $C_P \equiv (\partial H/\partial T)_P$ proportional to the fluctuations of entropy and (c) the thermal expansion coefficient $\alpha_P \equiv (1/V)(\partial V/\partial T)_P$ proportional to the cross-fluctuations of volume and entropy. The behavior of a normal fluid (indicated by the dashed line) is approximately an extrapolation of the behavior of liquid water at high temperature. Anomalies exhibited by water are apparent above the melting temperature T_m and become more striking when the fluid is supercooled below T_m .

electrostatic attractive forces [17] with a partial covalent nature [18]. As a consequence, the four water molecules, that are H-bonded to a central one, tend to repel each other and to form a tetrahedral structure. This structure possibly propagates at the second shell of the central water molecule, giving origin to an “open” structure. This tetrahedral structure is characterized by a density that is lower than the “closed” structure achieved when the HBs are broken at high pressure [19]. A fully developed tetrahedral network is well observed in ice Ih (hexagonal ice) and Ic (cubic ice). These are only two of the more than 16 crystal forms of water. Water is, therefore, a *polymorph* [20].

Just as there are crystalline polymorphs, there are also *polyamorphic* forms of water, i.e. different forms of amorphous ice (glass) of water. These are observable below $-123\text{ }^{\circ}\text{C}$ when the liquid is cooled with a rate of $106\text{ }^{\circ}\text{C}/\text{sec}$. To date, there have been observed three distinct forms of amorphous ice: low, high and very high density (LDA, HDL and VHDA) with discontinuity in volume of 27% (LDA -HAD) and 11% (VHDA-HAD) [21].

1.3 Different scenarios for supercooled water behavior

The presence of open and closed structures, has led to different interpretations of the behavior of supercooled water (Fig. 1.2). These can be divided into two main categories:

1. one hypothesizes that water separates into two liquid phases of different density through a transition analogous to the transformation between gas and liquid and with a possible singularity;
2. another assumes that the two local configurations are never separated into two phases.

Interpretations of type (i) account for the coexistence of a low density liquid (LDL) phase, with a structure similar to LDA ice, and a high density liquid (HDL) phase, similar to HDA ice. Due to the anti-correlation between the fluctuation of molecular volume and entropy, the HDL-LDL transition has a negative slope in the pressure-temperature (P - T) plane. Among the scenarios that involve the liquid-liquid (LL) phase transition are

- (a) the scenario with a LL critical point at $P > 0$ [22];
- (b) the scenario with a LL critical point at $P < 0$ [23];
- (c) the “critical point-free” scenario, in which the LL transition extends to the limit of stability (spinodal) of the liquid with respect to the gas at $P < 0$ [15].

In these scenarios the anomalous increase of response functions is a consequence of approaching the LL coexistence line, with a real divergence at the LL critical point or along the LL spinodal line. For the cases (a) and (b), at temperatures above the LL critical temperature the thermodynamic response functions increase near the temperature $T_W(P)$ of maximum correlation length. The line $T_W(P)$ in the P - T plane is called “Widom line” [24,25] and departs from the critical point, being its analytic continuation¹. Extremely close to the Widom line, the functions are rounded and remain finite.

In the critical point-free scenario [15], on the other hand, the liquid-gas spinodal at $P < 0$ crosses the LL spinodal leading to a change of slope of the stability limit of the liquid. A similar mechanism, with a reentrant spinodal was originally proposed in the “stability-limit” scenario [29], that relates the increase in response functions to the reentrant behavior of the temperature of maximum density (TMD) line. Nevertheless this scenario reveals some thermodynamic inconsistencies [30], that can be cured by interpreting the low- T spinodal as a LL spinodal. Hence, although absent in its original formulation, the LL transition phase was introduced later for thermodynamic consistency also in the stability-limit scenario [31].

To the category (ii) belongs the “singularity-free” interpretation [41]. In this scenario the anomalies are the effect of anti-correlation between the fluctuation of molecular volume and entropy, due to the fact that forming a H-bonded structure leads to a volume increase with an entropy decrease. The large increase in the response functions (Fig. 1.1) observed in experiments, in this interpretation, is an apparent singularity rounded in a maximum in correspondence to the continuous density change.

Recently, it has been shown [42] that the singularity-free interpretation holds for a coarse-grained water-like model (the mono-atomic-water model [43]), in contrast to another scenario called “weak crystallization theory” [44]. In Ref. [42] it is shown that the coupling constant required for fitting the results with the weak crystallization theory would be

¹A fluid-fluid critical point (CP) is found generally at the end of a first order phase transition line characterized by the coexistence of two thermodynamic distinct phases. In correspondence of the CP the correlation length ξ diverge. From classical thermodynamics it is known that beyond the critical point, in the supercritical region, does not exist any physical observable able to distinguish one phase respect to the other. Nevertheless, in this region is it possible to find a locus spanning from the critical point where ξ has a maxima. This locus is known as “Widom line” [24] and can be considered as the analytic continuation of the coexistence line.

The Widom line does not define a transition between two distinct thermodynamic phases, in the sense that no singularity is present in internal energy or in its derivative crossing this locus. However it marks a change in dynamical and structural properties of the system [26] analogous to the one observed crossing the coexistence line.

Curiously, in the original works of Widom, Rowlinson and Stillinger [27,28] the authors study the liquid-vapor phase transition finding a line of symmetry, comparable with those found hitherto only in lattice models (particle-hole symmetry), that is not strictly related with the supercritical behavior of ξ .

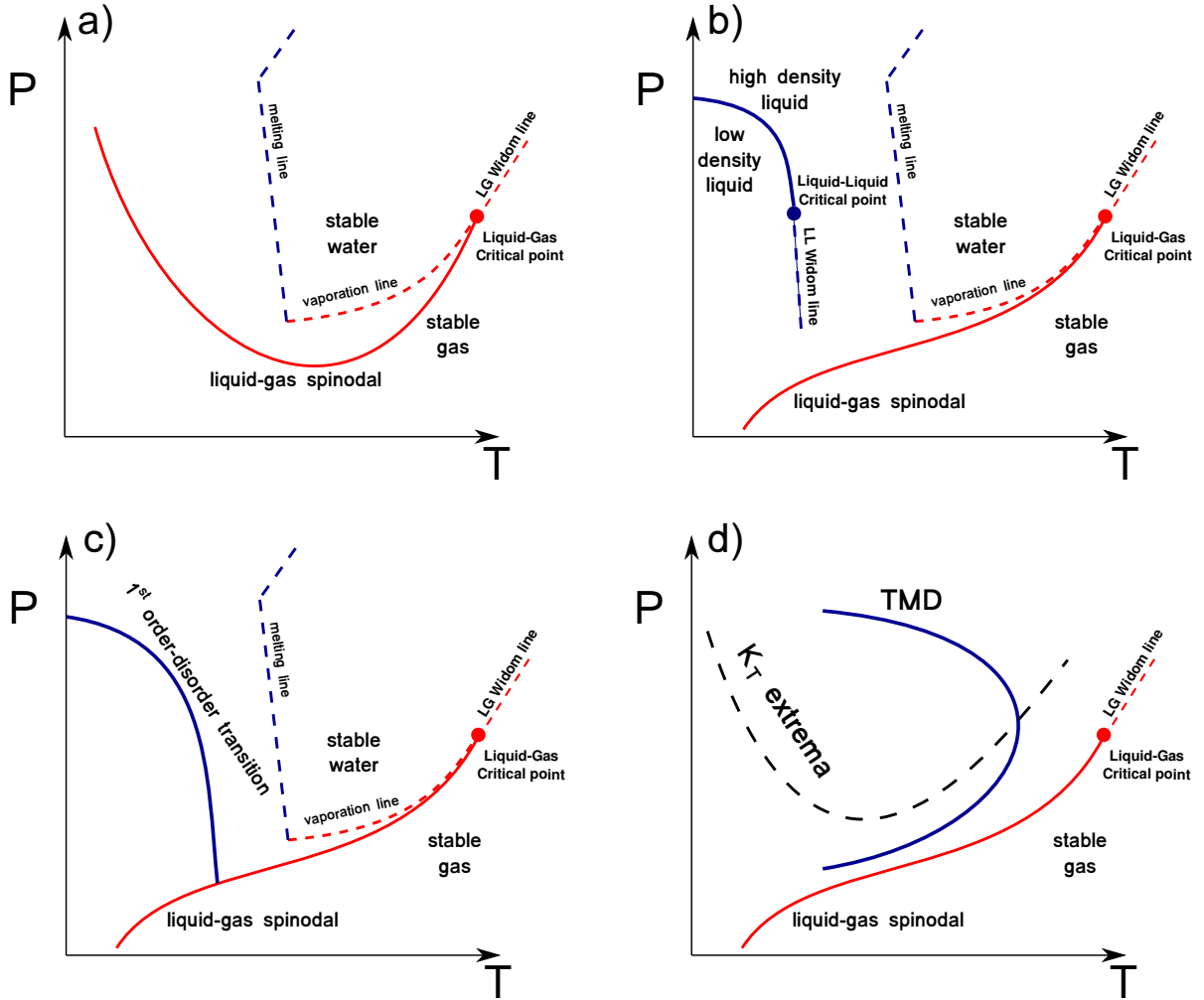


Figure 1.2: Schematic view of different thermodynamic models on the origin on water anomalies in the $T - P$ plane.

a) The stability limit scenario [29] hypothesizes that the liquid-to-gas spinodal, with positive slope at high T , merges with the stability limit of stretched and supercooled water, with negative slope at low T . The reentrant behavior originates from the intersection of the spinodal with the TMD line.

b) The liquid-liquid critical point scenario [22] supposes the existence of a second critical point for liquid water in the supercooled region as ending point of a negatively sloped first order transition line, separating two metastable liquids at different densities: the low-density liquid (LDL) at low P and T , and the high-density liquid (HDL) at high P and T . Several numerical results with different water models are consistent with this scenario [22, 23, 32–39].

c) The critical-point-free scenario [40] hypothesizes an order-disorder transition, with a possible discontinuity in density, that extends at negative pressure up to the stability limit of supercooled water.

d) The singularity-free scenario [41] relates the anomalous increase in K_T with the reentrant behavior of the TMD line, without any divergence in K_T and with a locus of constant maxima in C_P .

unphysical. The weak crystallization theory has been proposed also for another water model [44], the ST2 model [45], however several works have shown with different approaches that the ST2 model follows the scenario with a metastable LL critical point [35, 37–39, 46–48].

Recently, it has been shown [49] that the all the scenarios in categories (i) and (ii) result from a common physical mechanism, and that two key physical quantities determine which scenario describes water: (i) the strength of the directional component of the HB and (ii) the strength of the cooperative component of the HB. Furthermore, estimates from experimental data for HBs [49] lead to predict the occurrence of the scenario described in (a).

1.4 State of the art on hydration water at low temperature

All these scenarios rationalize the anomalies of water and compare well with the experimental data, but predict different phase diagrams, with different implications for the behavior of the water interface. For example, the presence of a LL critical point implies the presence of a Widom line. Along this line the density fluctuations determine structural changes that could explain recent experimental results of water confined in nanoscopic structures [50–52] and hydration water of proteins and DNA to almost -53 °C [53–58].

At these low temperatures, “bulk” water exists only in the solid state, but the confinement and the presence of interfaces distorts the formation of the network of HBs and lowers the freezing temperature [59]. This allows to explore the dynamics and thermodynamics of confined water, although the interpretation of experimental results is still controversial [53, 56, 59–66].

Liquid water hydrating proteins has been found at temperatures as low as -113 °C, at atmospheric pressure [52]. At these extremely low temperatures some interesting dynamic phenomena occur [67–71] suggesting a possible relationship between the dynamics of biological macromolecules and water around them [72, 73].

At low T , proteins exist in a state without conformational flexibility and are biologically inactive. In the literature, this state is commonly called “glass”. At approximately -53 °C hydrated proteins regain their flexibility and their biological activity. This dynamic transition is common in many biopolymers and is understood to be due to the strong coupling with the mobility of hydration water, which shows a similar dynamic transition at the same T [53, 56, 57, 62, 63, 69, 74–76]. Experiments studying the translational correlation time of the hydration water of a lysozyme protein [53], DNA [56] and RNA [57] have shown

that at about $-53\text{ }^\circ\text{C}$ (220 K) the dynamics of hydration water changes from non-Arrhenius (at high T) to Arrhenius (at low T), i.e. the dynamics has an activation energy that depends on T at high T , and is a constant at low T .

Simulations of lysozyme and DNA in hydration water (using the TIP5P-water model) [77] have found (i) that the fluctuations of mean square deviation for the hydrogens of lysozyme and DNA change functional form at $T_p \sim 245\text{ K}$, (ii) the specific heat of the total system (water and biopolymer) exhibits a maximum at $T \sim 250 \pm 10\text{ K}$ for both molecules, (iii) the structure of hydration water, as measured by a local tetrahedral order parameter, has a maximum increase around the same temperature, $T_Q = 245 \pm 10\text{ K}$, (iv) the diffusivity of hydration water exhibited a dynamic change from a non-Arrhenius to Arrhenius at a temperatures $T_x \sim 245 \pm 10\text{ K}$ for lysozyme and $T_x \sim 250 \pm 10\text{ K}$ for the DNA. These temperatures are much higher than the glass transition temperature, estimated for TIP5P at $T_g = 215\text{ K}$ [78]. The coincidence of these temperatures, all higher than T_g , suggests an interesting relationship between the thermodynamics and structural changes of the hydration water and fluctuations of proteins.

Similar results have been found also in confined water. Confined water is of fundamental importance in biological, geological and technological processes, including disciplines such as electro-chemistry or photo-catalysis [79]. In the past years experiments have revealed a dynamic change at $T \simeq 223 \pm 2\text{ K}$ for water confined in silica nano-pores (with a radius of 2 nm) by studying the structural relaxation time (with neutron scattering) [50] and the self-diffusion coefficient (with nuclear magnetic resonance) [52]. These dynamical changes observed in water confined in silica nanopores disappear at a pressure between 1200 and 1600 bar [70].

Results from simulations of water models (TIP5P and ST2) and of water-like models [24] have suggested that a possible explanation for disappearance of the dynamical changes may be the presence of a LL critical point. The simulations exhibit the same physical behavior as the experiments, and the change in the diffusion coefficient in the simulations vanishes at pressures higher than the pressure of the LL critical point. The authors interpret their simulation results as a consequence of the shape of the low- T LL spinodal line that flattens out above the LL critical point [24].

Therefore, although the results are argument of debate [60–63, 77], numerical and experimental evidences point to a strong dynamic effect of the first layers of water molecules on macromolecules, due to the hydration interaction. Understanding these interactions, which play a dominant role in many physical, chemical and biological agents requires knowledge

of the structure of the first layers of interfacial water at the molecular level [80]. Depending on whether the surface is hydrophilic or hydrophobic, the structure of the network of HBs of water is affected, being characterized by interruptions that give water its unique interface (e.g., surface tension) [81].

The study of the properties of water near a hydrophobic surface is a strong topic of debate, e.g. [82–84]. Understanding the water structure at the interface of a hydrophobic surface of nanoscopic size [85, 86] has important implications for the folding of proteins [87–90].

Experiments for water hydrating hydrophobic surfaces have been interpreted sometimes in favor of the formation of a depletion layer of water molecules [91–93], sometimes in favor of the reorientation of molecules [6, 83, 94–96] and sometimes only indicating the formation of “nano-bubbles” of local depletion [97, 98].

Water near hydrophilic surfaces behaves in a way that could be quite different from water at hydrophobic interfaces. Some authors suggest that near a hydrophobic surface water has a local LDL structure (low density and tetrahedral), while near a hydrophilic surface is more closed, as in regions of high density (HDL) [99]. Experiments show that water molecules close to hydrophilic surfaces have residence times longer than near hydrophobic surfaces [100], and that water confined between two hydrophilic surfaces, separated by 2nm, has a viscosity several orders of magnitude greater than “bulk” water [101, 102]. These differences have important implications in applications such as microfluidics or the development of biomaterials, where water produces a hydrophilic pressure that favors the adherence of bone grafts [103].

Simulations can substantiate hypothesis (see for example ref. [104]), but are based on specific models [105] and it is difficult to see whether their results have the character of universality that experimental data suggest. To this goal it could be relevant to analyze the results of a coarse-grained water model that can be studied analytically and, by tuning a few parameters, could be able to reproduce the results of different atomistic models.

Chapter 2

A coarse-grain model for a confined water monolayer

2.1 The need of coarse-grain approach

In the previous chapter we have seen that the anomalies properties of water can be interpreted as related to the occurrence of a liquid-liquid critical point (LLCP) in the supercooled region. However, to date it is experimentally unfeasible to keep bulk water liquid in the region where the LLCP is predicted. The reason is that the homogeneous nucleation time ¹, at that thermodynamic conditions, is smaller with respect to the resolution time of the experiments. A possible way to prevent crystallization is to confine water in hydrophilic or hydrophobic nano-structures [65, 66, 106]. In particular, the confinement of water in quasi-one or two dimensions (2D) is allowing to the discovery of new and controversial phenomena in experiments [70, 107–110] and the relationship between confined water and bulk water is presently widely debated. For these reasons it is important the study models that allows us to change and tune at will parameters that would be difficult to handle experimentally. These studies could shed light on the underlying mechanics that are responsible for the peculiar properties of water.

In this chapter we define a coarse-grained model for a water monolayer confined between two hydrophobic flat walls. In the second part of the chapter we describe the method

¹In a liquid system, due to thermal fluctuations, there is non-zero probability that particles form a nucleus of ordered crystalline phase. Below the melting temperature T_m the crystal phase is thermodynamically favored having a smaller free energy with respect a liquid droplet with the same number of particles. Nevertheless there is a competition between the free energy gain, proportional to volume cluster, and the free energy cost to form an a crystal-liquid interface proportional to the nucleus surface. The critical radius R_c represents the minimum size of a stable crystal cluster and the homogeneous nucleation time τ is the time needed to form such critical nucleus.

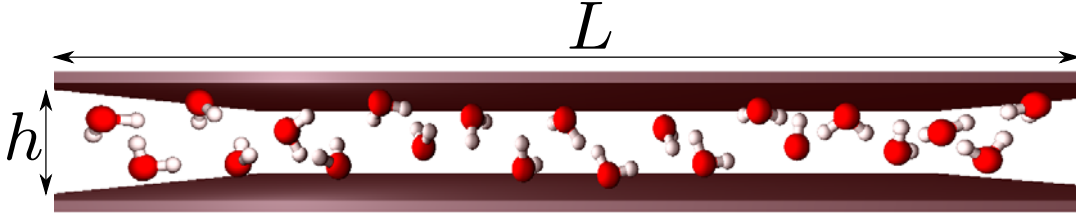


Figure 2.1: Schematic view of a section of the water mono-layer confined between hydrophobic walls of size $L \times L$ separated by $h \sim 0.5$ nm.

we adopt to study the model. Specifically, we use here Monte Carlo (MC) simulations to generate an artificial dynamic in order to bring the system to thermodynamic equilibrium, according to the Boltzmann statistic, as quickly as possible. To this goal, we adopt a "cluster" MC dynamics. Methods based on cluster move [111–113], i.e. contemporary change of the status of several degrees of freedom, can speed up computation, especially near a critical point. In particular, we follow a cluster MC dynamics based on a percolation approach that will be introduced in details in Chapter 4, where we will show how the approach allows us to estimate relevant thermodynamic quantities, beside speeding up the simulations.

In particular we combine the cluster MC dynamics with standard Metropolis MC to explore the accessible phase space in a very efficient and fast way. Our simulation approach is less expensive, in terms of CPU time, than other MC techniques and is able to equilibrate at very low temperatures also systems made of millions of molecules, something that is unfeasible with other methods, including Molecular Dynamics.

2.2 The model

To analyze the thermodynamic properties of water in confinement we consider a monolayer of water molecules between hydrophobic walls of area L^2 separated by $h \approx 0.5$ nm (Fig. 2.1). Atomistic simulations [114–117] show that water under these conditions does not crystallize, but arranges in an disordered liquid layer, whose projection on one of the surfaces has square symmetry (Fig. 2.1), with each water molecule having four nearest neighbors. The molecules maximize their intermolecular distance by occupying different distances from the two walls.

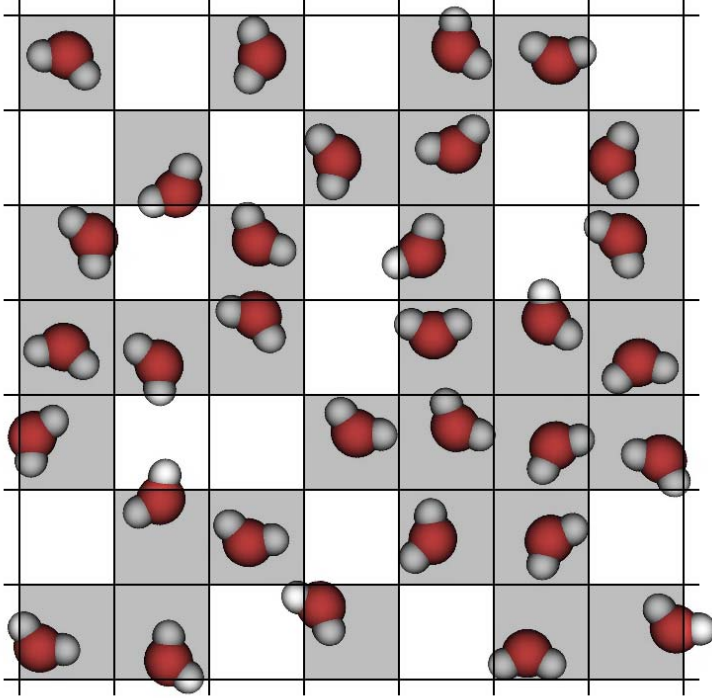


Figure 2.2: Coarse-graining of space divided in 7^2 cells. Grey cells are considered to be liquid-like cells, with occupation number $n = 1$. White cells represent gas-like cells corresponding to $n = 0$.

2.2.1 Coarse grain of the volume

The first step in formulating the model is to discretize space dividing the total available volume V into a fixed number N_0 of cells, each with volume $v \equiv V/N_0$. This is done on a length scale such that each cell contains at most one molecule, with hard core volume v_0 . Because we consider the constant pressure P , constant temperature T , constant number of molecules N , the volume V is a function of P and T , with $V \geq Nv_0$ where v_0 is the hard-core volume of a molecule. We neglect the position of the water molecules inside the cell and associate to the cell a variable $n = 0$ if the cell density $v_0/v \leq 0.5$ (gas-like cell) and $n = 1$ if $v_0/v > 0.5$ (liquid-like cell). A representative picture is given in Fig. 2.2.

2.2.2 Isotropic interaction

The long range and isotropic interaction between water molecules occupying cells i and j at distance r_{ij} is given by two main components: the electrostatic attraction due to fluctuating induced dipoles (van der Waals forces); the hard core repulsion due to the Pauli exclusion principle. Such effects are well described by the truncated Lennard-Jones

potential $U(r)$ [118] (Fig. 2.3)

$$U(r) = \begin{cases} \infty & \text{for } r_{ij} < r_0 \\ 4\epsilon \left[\left(\frac{r_0}{r_{ij}} \right)^{12} - \left(\frac{r_0}{r_{ij}} \right)^6 \right] & \text{for } r_0 \leq r_{ij} \leq 25r_0 \end{cases} \quad (2.1)$$

modified introducing an hard wall at the hard core radius $r_0 \sim v_0^{1/3}$ and a cutoff at distance $25r_0$. ϵ represents the characteristic energy and in internal units it is equal to 1. The distance r_{ij} is measured in cell size unit.

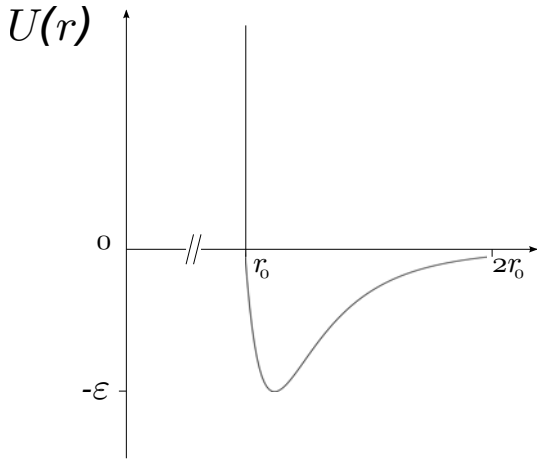


Figure 2.3: Truncated Lennard-Jones Potential.

2.2.3 Directional HB interaction

Hydrogen bonding accounts for many of the peculiar properties of water. It is a special directional interaction which occurs when hydrogen atoms are covalently bonded to an electronegative atom such as oxygen. The hydrogen atom has a small size and a single electron, because of this the electronegative and electro-positive parts of the atom, separated furthest away one other, are significantly unshielded and can interact other charged atoms. In order to describe HB formation we associate to each water molecules i four bonding variables $\sigma_{ij} = 1, \dots, q$ facing nearest neighbors molecules j . Each variable $\sigma_{i,j}$ can participate to a HB, being four the maximum number of HBs. From experiments we learn that a water molecule can form more than four HBs, but that only four can be associated to the low-energy tetrahedral configuration made of a water molecule and its hydration shell.

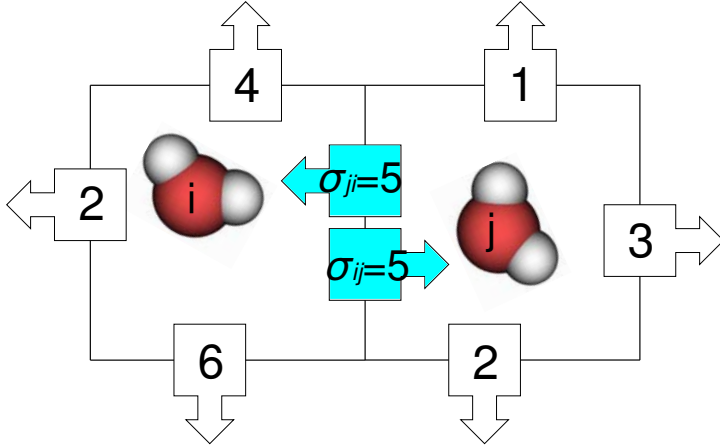


Figure 2.4: Scheme of directional interaction of HB. The state of a molecule i is completely characterized by the occupation number n_i , and four bonding variables, each one for the next neighbor cell. A HB is formed when two facing bonding variables (represented here by squares with numbers, with an arrow pointing toward the facing molecule) are in the same bonding state (represented by the number within the square). For example, the two molecules i and j in the figure form a HB, being their facing bonding variables in the same state $\sigma_{ij} = \sigma_{ji} = 5$.

Additional (“bifurcated”) HBs will increase the energy associated to the molecule and will form at angles that are inconsistent with the tetrahedral configuration. We include in our description only “tetrahedral” HBs. The tetrahedral HBs can be associated to a configuration where the O–H–O atoms deviates less than 30° from the perfect alignment. Hence, the bonded state corresponds to $1/6$ of all the possible configurations of the O–H–O atoms in the plane they define. We, therefore, choose $q = 6$ in such a way that only $1/6$ of the σ_{ij} states is associated to a bonded state. As a consequence each molecule has $q^4 = 1296$ bonding states. From the experiments we know that the formation of a HB decreases the energy of the system and its entropy [30]. The model includes this behavior by assuming that two nearest neighbor molecules i and j form a HB, reducing the energy of the system by a quantity $J > 0$, if the variables $\sigma_{i,j}$ and $\sigma_{j,i}$, one on each molecule and each facing the other, are in the same state. Hence we add to the Hamiltonian the term (sketched in Fig. 2.4)

$$JN_{\text{HB}} \equiv J \sum_{\langle ij \rangle} n_i n_j \delta_{\sigma_{ij}, \sigma_{ji}} \quad (2.2)$$

where N_{HB} is the number of HBs.

2.2.4 HB cooperativity

Experiments suggest that the formation of HB is a cooperative process [119, 120], as discussed in Ref. [49]. Formation of a single bond leads to further polarization of the atoms

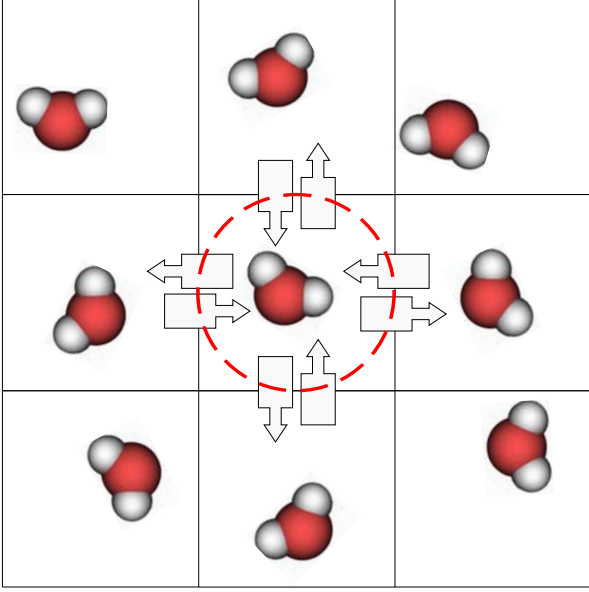


Figure 2.5: Scheme of cooperative interaction of HB involving all the bonding variables σ_{ij} of the molecule i at the center of the figure.

involved [121]. As a result, successive bonds have a lower energy, and form more readily. To include this effect, the model assumes that the energy decreases of a quantity $0 < J_\sigma < J$ when any two of the four variables $\sigma_{i,j}$ on the same molecules i are in the same state

$$J_\sigma N_{\text{coop}} \equiv J_\sigma \sum_i n_i \sum_{(l,k)_i} \delta_{\sigma_{ik}, \sigma_{il}} \quad (2.3)$$

where the first sum is over all occupied cells, the second sum is over each of the six different pairs of the four indices σ_{ij} of a molecule i (Fig. 2.5). The fact that $J_\sigma < J$ guarantees that this interaction implies a rearrangement of all the HBs formed by the molecule i , being an effective many-body interaction.

Hence the Hamiltonian of the model is

$$\mathcal{H} = U(r) - JN_{\text{HB}} - J_\sigma N_{\text{coop}} = U(r) - J \sum_{\langle ij \rangle} n_i n_j \delta_{\sigma_{ij}, \sigma_{ji}} - J_\sigma \sum_i n_i \sum_{(l,k)_i} \delta_{\sigma_{ik}, \sigma_{il}}. \quad (2.4)$$

2.2.5 Volume dependence on HBs

Experimental interpretations suggest that tetrahedrally bonded water molecules form locally a low density structure up to the second shell [19]. Increasing the pressure or the

temperature, the local density increases as a consequence of the disruption of the tetrahedral structure, i.e. as a consequence of the breaking of the tetrahedral HBs considered here. A simple way to include this effect in the model is to assume that the volume per molecule $v = V/N$ depends linearly on the number of HBs N_{HB}

$$v = V/N \equiv (V_0 + N_{\text{HB}}v_{\text{HB}})/N \quad (2.5)$$

where $v_0 = V_0/N$ is the molecular volume without accounting for the HBs, depending on P and T , and v_{HB} is the volume increase per HB given by the difference in volume between the local low-density tetrahedral structure and the compact structure in absence of HBs. Experiments show that $v_{\text{HB}} = v_0/2$ is a reasonable choice [122].

Without loss of generality, we set $4\epsilon = 1$ and $v_0 = 1$, which set only absolute scales for temperature T and pressure P . As discussed in ref [49], we estimate the covalent component of HB to be $J/4\epsilon = 0.5$ and cooperative HB term to be $J_\sigma/4\epsilon = 0.05$.

2.3 Monte Carlo simulation

The system is studied using MC simulations in NPT thermodynamic ensemble (constant number of particles N , pressure P and temperature T). The phase space is sampled using the Metropolis algorithm [123] and Wolff algorithm [112]. We assume the system to be homogeneous setting all occupation number $n_i = 1$ because we are not interested in study the diffusive dynamic of the model. Nevertheless our results do not change significantly considering partially hydrated surface. Simulations are carried out for square systems with size L ranging from 50 to 400, i.e. the number of water molecules N ranges from 2500 to 160 000. The total number of degrees of freedom is $4N + 1$.

The general scheme of MC simulation is to evolve the system generating new configurations that can be accepted or rejected with a certain probability. Depending on the thermodynamic ensemble, such probability is calculated in order to get the expected microstate distribution probability at the equilibrium. In the NPT ensemble, the probability of a microstate with energy E and volume V is proportional to

$$p = e^{-\beta(E+PV)} \quad (2.6)$$

where $\beta \equiv 1/(k_B T)$ and k_B is the Boltzmann constant. The partition function is given by the sum (or the integral in case of continuum spectrum of degrees of freedom) of the

microstate probability over all possible configurations of energy and volume. The thermodynamic potential associate to the NPT ensemble is the Gibbs free energy

$$G \equiv E - TS + PV \quad (2.7)$$

where S is the entropy of the system. In general the acceptance probability to pass from a configuration x_m to a configuration x_n is proportional to $\exp[-\beta(G(x_n) - G(x_m))]$.

2.3.1 Metropolis algorithm

Metropolis algorithm consists in select randomly one of the $4N$ bonding variables σ_{ij} or the molecular volume v trying to change its value. In a single MC step $4N$ spin flips and one volume change are performed. Spin flip entails a possible change in number of cooperative bonds ΔN_{coop} and in number of HBs ΔN_{HB} . The acceptance probability p_v depends on enthalpy variation

$$\Delta H \equiv \Delta E + P\Delta V = (J - Pv_{\text{HB}})\Delta N_{\text{HB}} + J_\sigma \Delta N_{\text{coop}} \quad (2.8)$$

with the following relation

$$p_v \equiv \begin{cases} 1 & \text{if } \Delta H \leq 0 \\ e^{-\beta\Delta H} & \text{if } \Delta H > 0 \end{cases} . \quad (2.9)$$

Small cell size variations are chosen such that $\Delta r/r_0 \in [-0.01; 0.01]$, and the move is accepted with probability p_v

$$p_v = \begin{cases} 1 & \text{if } \Delta G \leq 0 \\ e^{-\beta\Delta G} & \text{if } \Delta G > 0 \end{cases} \quad (2.10)$$

where ΔG is the Gibbs energy change

$$\Delta G = \Delta E_{LJ} + P\Delta V_{LJ} - T\Delta S \quad (2.11)$$

and ΔE_{LJ} is the change in Lennard-Jones energy, $\Delta V_{LJ} = N[(r + \Delta r)^2 - r^2]$ the volume change and $\Delta S = -2NT \ln(1 + \Delta r/r)$ the entropy change associate to the volume change.

2.3.2 Wolff algorithm

Wolff algorithm is based on the definition of cluster of correlated degrees of freedom, described in section 4.1. A cluster is built with the following step:

1. choose randomly a molecule i and at random one of its four variable σ_{ij} ; this is the first element of the cluster; let be \tilde{q} its bonding state;
2. if the remaining arms of the molecule i are in the bonding state \tilde{q} add them to the cluster with probability $p_{J_\sigma} = 1 - \exp(-\beta J_\sigma)$;
3. check the value q^* of the arm of the next neighbor (n.n.) molecule facing the initial arm. If $J_{\text{eff}} = J - Pv_{\text{HB}} > 0$ and $\tilde{q} = q^*$, add it to the cluster with probability $p_J = 1 - \exp(-\beta J_{\text{eff}})$; if $J_{\text{eff}} < 0$ and $\tilde{q} \neq q^*$, add it to the cluster with probability p_J ;
4. repeat steps 1, 2 and 3 with the new elements added to the cluster, checking new variables that have not been checked before in all directions, until no more variables are added to the cluster;
5. if $J_{\text{eff}} > 0$, choose randomly a new bonding value q' and flip all the elements of the cluster; otherwise if $J_{\text{eff}} < 0$ change each arm according to the rule

$$\sigma^{\text{new}} \equiv (\sigma^{\text{old}} + q') \pmod{q} . \quad (2.12)$$

The update of the volume is done with same procedure described in the previous section. It is possible to prove that the MC dynamics described by the previous steps respects the requirements of detailed balance and ergodicity of a valid MC dynamics and guarantee the correct exploration of phase space according to the Boltzmann distribution [124].

Independently of the adopted algorithm, simulations are carried out along isobars starting from high T ($T \sim 1\epsilon/k_B$) with a random initial condition. Once the system is equilibrated, the final configuration is adopted as initial configuration for $T' \equiv T - \Delta T$ with a $\Delta T \in [10^{-6}; 0.05]$, following an annealing procedure. The thermodynamic equilibrium is reached when all the average thermodynamic quantities remain constant, within a given tolerance ($\sim 10^6$ MC steps), over many successive MC steps, and probing that the fluctuation-dissipation relations (3.5) and (3.7) are satisfied. Each state point is sampled over $10^3 \div 10^5$ (depending on the size L) statically independent configurations. Two configurations are

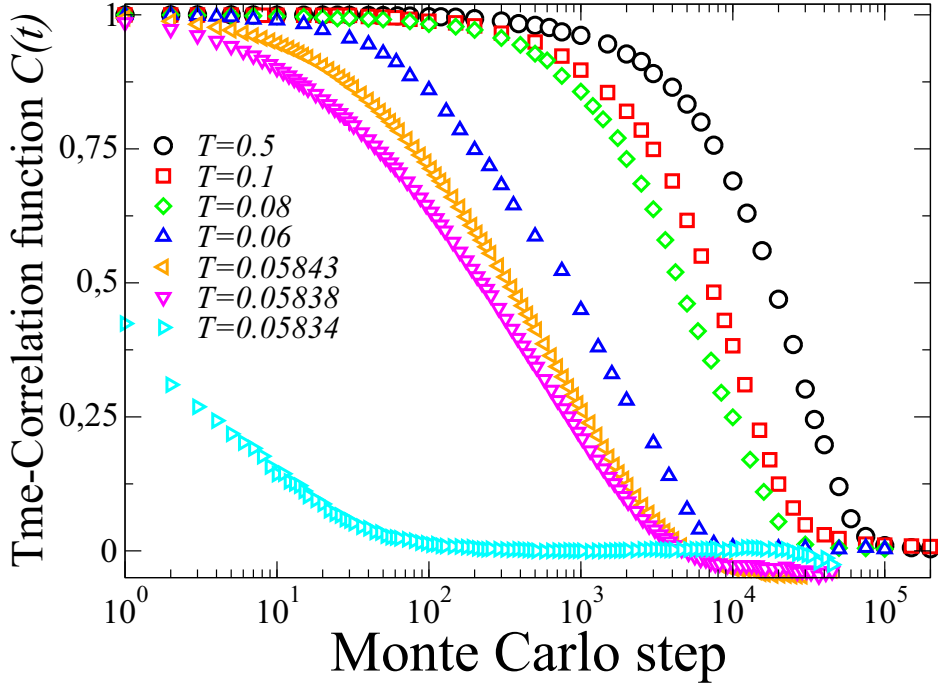


Figure 2.6: Time-correlation function $C(t)$ for $N = 10000$ water molecules at the pressure $P = 0.6$ using the Wolff algorithm. Below the percolation threshold, here for $0.05834 \leq T < 0.05838$ the correlation time τ drastically reduces. Pressure is expressed in ϵ/v_0 , temperatures in ϵ/k_B and $C(t)$ is dimensionless.

assumed to be uncorrelated after a time 2τ (in Monte Carlo step unit) so that the auto-correlation function $C(\tau) = 1/e$

$$C(t) \equiv \frac{1}{4N} \sum_{i=1}^N \sum_{j=1}^4 \frac{\langle \sigma_{ij}(t) \sigma_{ij}(0) \rangle - \langle \sigma_{ij} \rangle^2}{\langle \sigma_{ij}^2 \rangle - \langle \sigma_{ij} \rangle^2}. \quad (2.13)$$

The calculation of τ allows us to estimate how many MC steps are necessary in order to get a statistically independent new configuration. At high T there is no particular advantage in using Wolff algorithm. In this conditions, as we will see later, the average cluster size is small and the routine used to build up the cluster takes more CPU time respect the simplest scheme of Metropolis resulting in slightly longer simulations. Reversely, at low T , and in particular close a critical point, Wolff algorithm is particularly useful because it avoids the critical-slowing down (Fig. 2.6).

2.3.3 Internal units

All the calculated quantities we show in chapters 3, 4 and 5 are expressed in internal units.

- Temperature unit: $4\epsilon/k_B$;
- Pressure unit: $4\epsilon/v_0$;
- Density unit: $1/v_0$;
- Specific heat unit: k_B ;
- Compressibility unit: $v_0/4\epsilon$;
- Thermal expansivity unit: $k_B/4\epsilon$;
- Free energy unit: 4ϵ .

Chapter 3

Thermodynamic results

In this chapter we show the thermodynamic results and the phase diagram for confined water within the framework of the model introduced in Chapter 2. We analyze the behavior of density, thermodynamic response functions and correlation length identifying the critical region and the Widom line. By finite size scaling of the appropriate order parameter, we find a liquid-liquid critical point (LLCP) in the universality class of the two-dimensional (2D) Ising model in the limit of infinite walls.

3.1 TMD line and Spinodals

We calculate the density ρ of the system

$$\rho \equiv \frac{N}{V} \tag{3.1}$$

as function of T along isobars. For a broad range of P , we find a maximum and a minimum of density along each isobar 3.1 according to experimental evidences ¹. These maxima and minima identify for each P the temperature of maximum density (TMD) and the temperature of minimum density (TminD) (Fig. 3.2). At low values of T a discontinuous change in ρ is observed for $1 > P \geq 0.5$, as it would be expected in correspondence of the HDL-LDL phase transition. At very high pressures ($P > 1$) the system behaves as a normal liquid, with monotonically increase of ρ upon decrease of T .

We estimate the liquid-to-gas (LG) spinodal at $P < 0$ for low T (Fig. 3.1) as the temperature along an isobar at which we find a discontinuous jump of ρ to zero value. LG

¹For an exhaustive collection of experimental data look at the reference [12] and the Martin Chaplin web site <http://www.lsbu.ac.uk/water/index.html>.

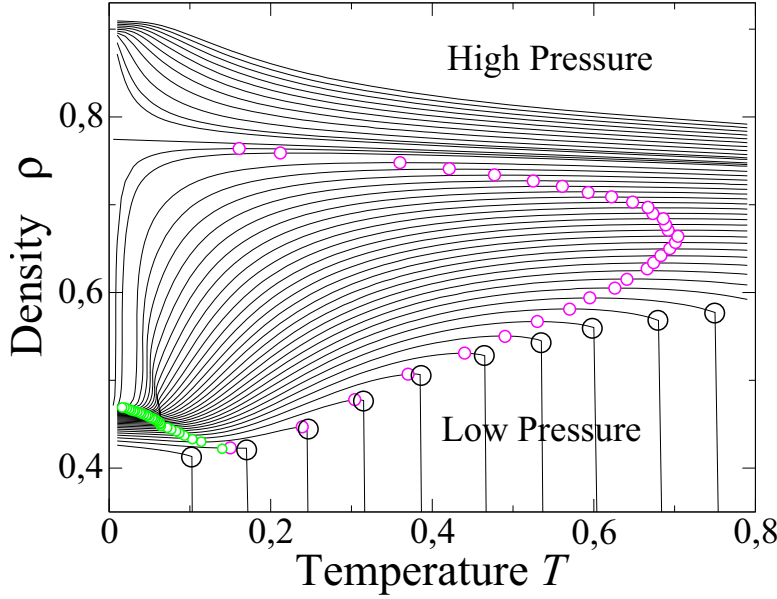


Figure 3.1: Isobaric density variation for 10^4 water molecule. Lines join simulated state points (~ 150 for each isobar). P increases from -0.5 (lower curve) to 1.5 (higher curve). Along each isobar we locate the maximum ρ (magenta small circles at high T) and the minimum ρ (green small circles at low T) and the liquid-gas LG spinodal (black large circles at low P). All the quantities are expressed in internal units.

spinodal identifies the locus of the stability limit of liquid phase with respect to the gas phase: below this curve is no longer possible to equilibrate the system in the liquid phase. The (LG) spinodal continues at positive pressures merging with the liquid-gas critical point (data not shown).

The LG spinodal is recovered also as envelope of isochores [12], shown in panel (b) of Fig. 3.1. Indeed we can write

$$dP = \left(\frac{\partial P}{\partial T} \right)_{\xi} dT + \left(\frac{\partial P}{\partial \xi} \right)_T d\xi \quad (3.2)$$

being ξ a generic intensive property. Along the spinodal we have

$$\left(\frac{dP}{dT} \right)_{\text{sp}} = \left(\frac{\partial P}{\partial T} \right)_{\xi} + \left(\frac{\partial P}{\partial V} \right)_T \left(\frac{\partial V}{\partial \xi} \right)_T \left(\frac{\partial \xi}{\partial T} \right)_{\text{sp}}. \quad (3.3)$$

At the spinodal isothermal compressibility (see eq 3.5) diverge, so that $(\partial P/\partial V) = 0$. Therefore eq. 3.3 means that the $P - T$ projection of spinodal curve is an envelope of constant- ξ lines as long as both $(\partial V/\partial \xi)_T$ and the $\xi - T$ projection of the spinodal have finite slopes. Because volume, enthalpy and entropy vary smooth along the spinodal, the former condition is satisfied when ξ is one of these three quantities.

A second envelope of isochores is found at lower T and higher P , pointing out the liquid-to-liquid (LL) spinodal. Actually the HDL-LDL spinodal collapse on the top of the

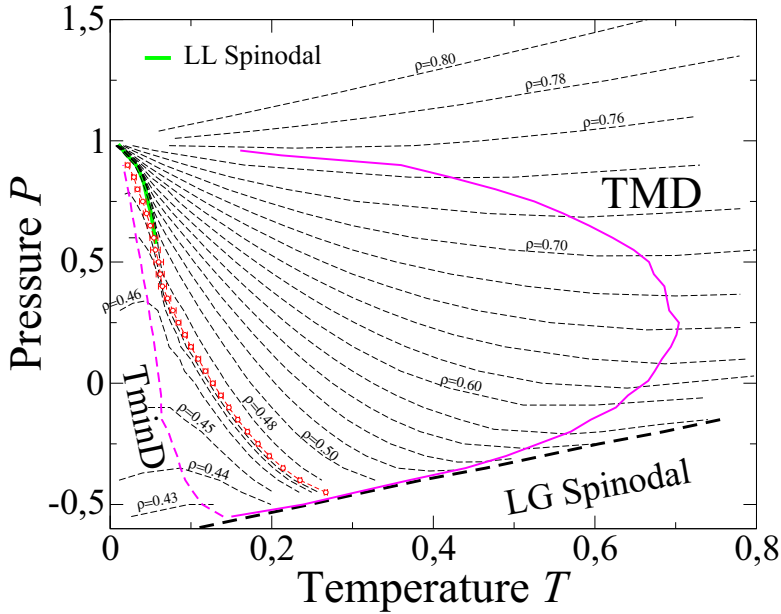


Figure 3.2: Loci of TMD, TminD, liquid-gas spinodal and liquid-liquid spinodal in TP plane. Lines represent the isochores of the system from $\rho = 0.43$ (bottom) to $\rho = 0.80$ (top). TMD and TminD correspond to the loci of minima and maxima, respectively, along isochores in the TP plane. We estimate the critical isochore at $\rho \sim 0.47$ (red circles). All the isochores with $0.47 < \rho < 0.76$ intersect with the critical isochore for $P \leq 0.5$ along the LL spinodal (tick green) line. All the quantities are expressed in internal units.

LDL-HDL spinodal and it is not possible to distinguish inside our numerical resolution. Nevertheless we clearly see that isochores are gathering around the points ($T \sim 0.06, P \sim 0.5$) and ($T = 0, P = 1$), marking two possible critical regions.

The TMD approaches the LG spinodal, without touching it, and continues in the TminD as in experiments [125] and other models [126, 127].

3.2 Thermodynamic response functions

3.2.1 Isothermal compressibility

We calculate the isothermal compressibility by its definition and by the fluctuation-dissipation theorem

$$K_T \equiv - \left(\frac{\partial \ln \langle V \rangle}{\partial P} \right)_T \quad (3.4)$$

and by the fluctuation-dissipation theorem

$$K_T = \frac{\langle \Delta V^2 \rangle}{k_B T V} \quad (3.5)$$

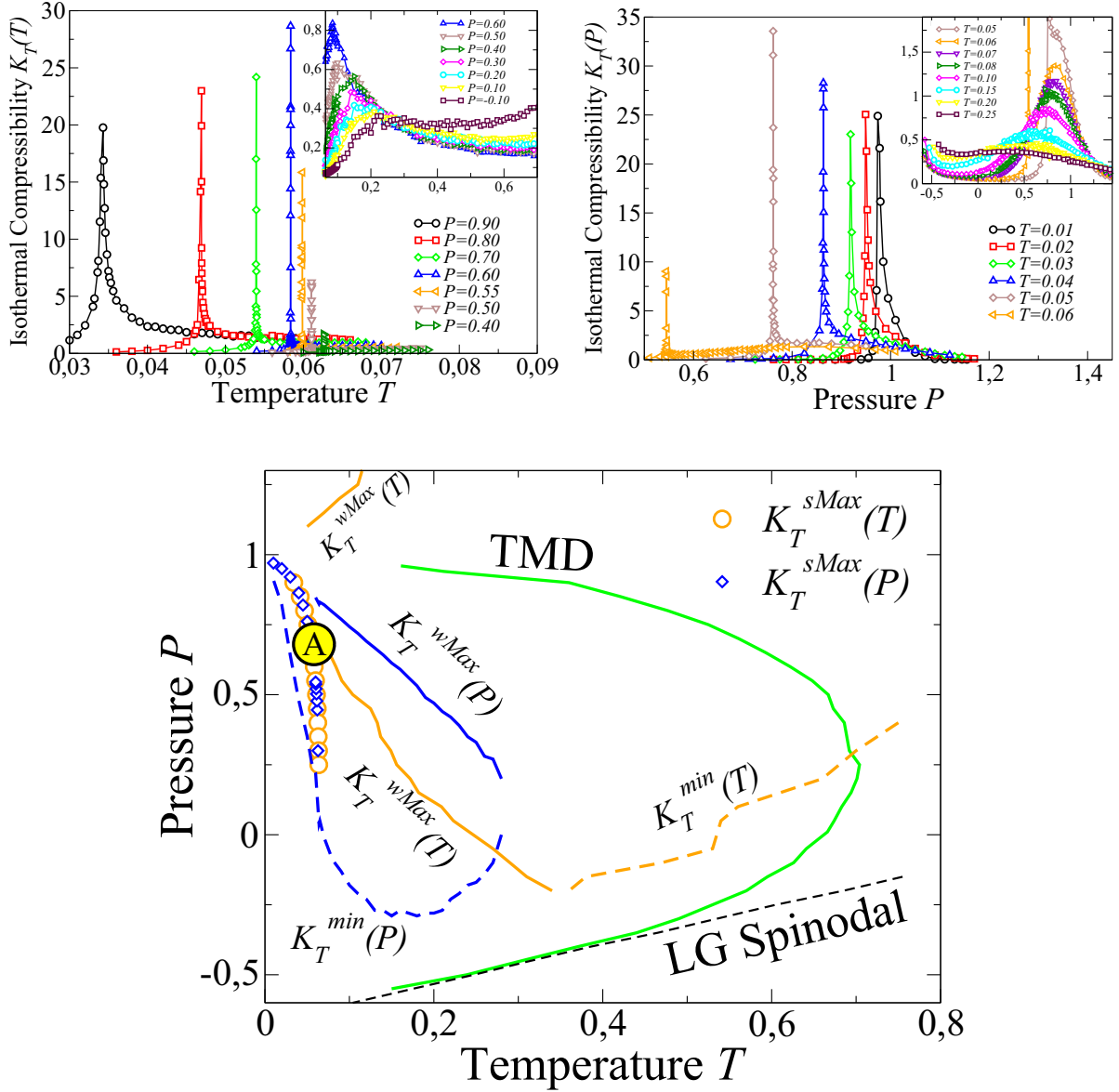


Figure 3.3: **Top-left panel:** The isothermal compressibility $K_T(T)$ at constant P displays strong maxima $K_T^{sMax}(T)$ at low T and high P (main panel), weak maxima $K_T^{wMax}(T)$ at higher T extending at lower P and merging with minima $K_T^{min}(T)$ occurring at higher T and higher P (inset). **Top-right panel:** Also the isothermal compressibility $K_T(P)$ at constant T displays strong maxima $K_T^{sMax}(P)$ and weak maxima $K_T^{wMax}(P)$ merging with minima $K_T^{min}(P)$ (inset), but the minima in this case extend to lower T and in a wide range of P . **Bottom panel:** The strong maxima (symbols), weak maxima (solid lines) and minima (dashed lines) of $K_T(T)$ (orange) and $K_T(P)$ (blue) form loci in TP plane that relate to each other and intersect with the TMD line following thermodynamic relations discussed in the text. The large yellow circle with label A identifies the region where $K_T^{sMax}(T)$ and $K_T^{sMax}(P)$ converge and display the largest maxima, consistent with the occurrence of a critical point in a finite-size system.

along isobars $K_T(T)$ and along isotherms $K_T(P)$ (Fig. 3.3), where $\langle V \rangle$ is the average volume, $\langle \Delta V^2 \rangle$ the volume fluctuations and k_B the Boltzmann constant. We find two loci of extrema for each quantity $K_T(T)$ and $K_T(P)$: one of strong maxima and one for weak maxima. The loci of stronger maxima in $K_T(T)$ and $K_T(P)$, respectively $K_T^{\text{sMax}}(T)$ and $K_T^{\text{sMax}}(P)$, overlap within the error bar with the LL spinodal. The maxima $K_T^{\text{sMax}}(T)$ and $K_T^{\text{sMax}}(P)$ increase in the range of $P \in [0.55; 0.6]$ and $T \in [0.05; 0.06]$ (Fig. 3.3), consistent with the existence of a critical region. The stronger maxima disappear at low P for $P < 0.4$.

We find also loci of weaker maxima, $K_T^{\text{wMax}}(T)$ and $K_T^{\text{wMax}}(P)$ and minima $K_T^{\text{min}}(T)$ and $K_T^{\text{min}}(P)$. The loci of extrema of $K_T(T)$ and $K_T(P)$ do not coincide in the $T - P$ plane:

- the locus of weaker maxima along isotherms $K_T^{\text{wMax}}(P)$ merges with the locus of minima $K_T^{\text{min}}(P)$ in the point where the slope of both loci is $\partial P / \partial T \rightarrow \infty$. Furthermore, both loci approach to the LL spinodal at high P ;
- the locus of weaker maxima along isobars $K_T^{\text{wMax}}(T)$ approaches the LL spinodal where K_T exhibits the strongest maxima, and merges with the locus of minima $K_T^{\text{min}}(T)$ where the slope of both loci is $\partial P / \partial T \rightarrow 0$ (data at high P and T not shown in Fig 3.3). This locus intersects the TMD in its turning point. Indeed, as reported in ref. [41] and in the section 6, the temperature dependence of K_T along the TMD line is related to the slope of TMD line

$$\left(\frac{\partial K_T}{\partial T} \right)_{P, \text{TMD}} = \frac{1}{V} \frac{\partial^2 V / \partial T^2}{(\partial P / \partial T)_{\text{TMD}}} \quad (3.6)$$

where $(\partial K_T / \partial T)_{P, \text{TMD}}$ is the derivative of K_T calculated at the TMD line and $(\partial P / \partial T)_{\text{TMD}}$ is the slope of TMD line. Hence the locus of extrema in K_T , where $(\partial K_T / \partial T)_P = 0$, crosses TMD line where the slope $(\partial P / \partial T)_{\text{TMD}}$ is infinite. The change from maxima to minima in weak extrema of $K_T(T)$ is consistent with the change in slope of the TMD line, as described in Ref. [41, 128].

The weak maxima of $K_T(T)$ and $K_T(P)$ increase as they approach the LL spinodal. All loci of extrema in K_T are summarized in Fig. 3.3.

3.2.2 Isobaric specific heat

Next we calculate the isobaric specific heat

$$C_P \equiv \left(\frac{\partial \langle H \rangle}{\partial T} \right)_P = \frac{\langle \Delta H^2 \rangle}{k_B T} \quad (3.7)$$

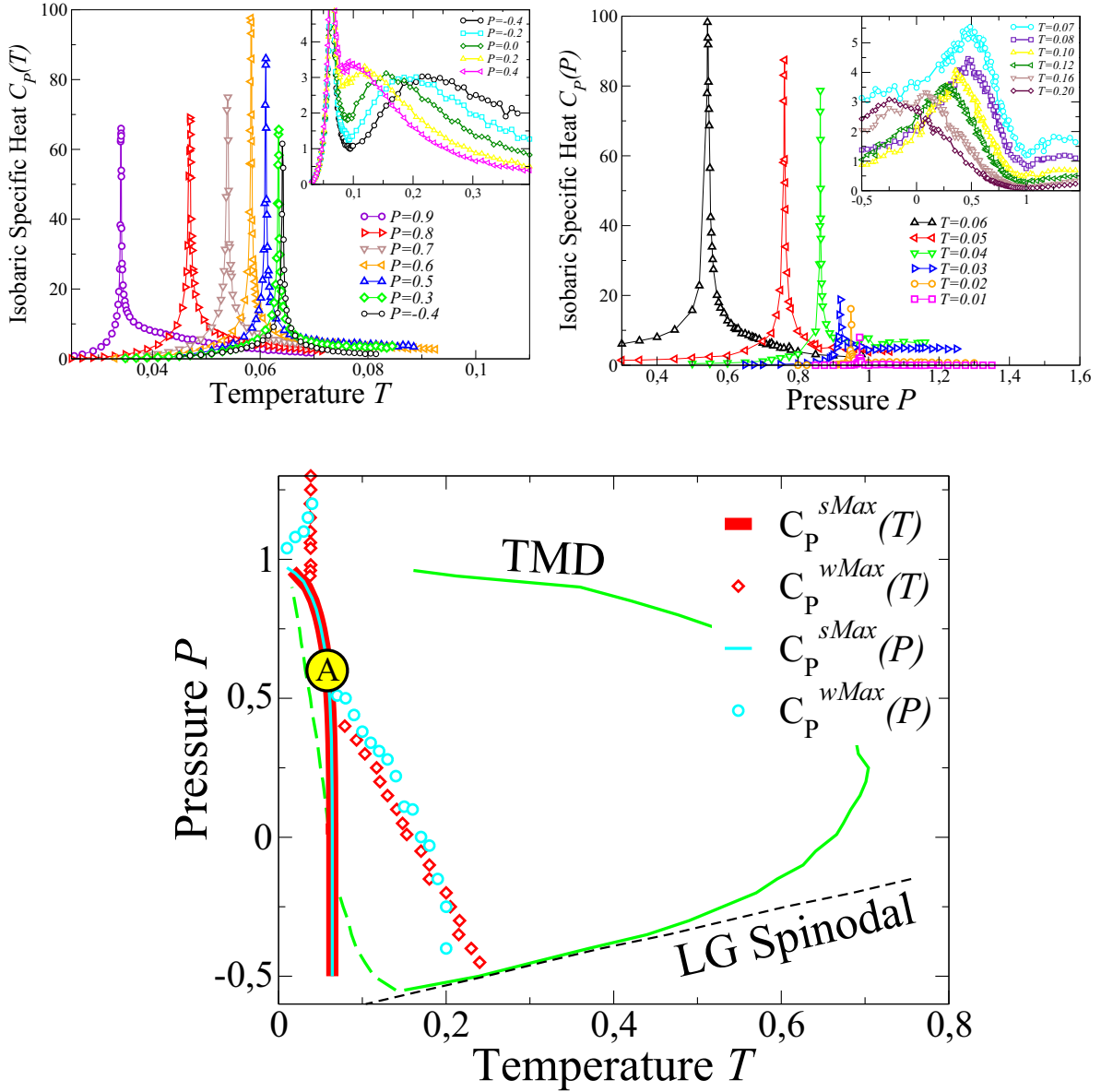


Figure 3.4: **Top-left panel:** loci of stronger maxima in C_P (weaker in the inset) along isobars. **Top-right panel:** loci of stronger maxima in C_P (weaker in the inset) along isotherms. **Bottom panel:** projection of C_P maxima in $T - P$ plane. The large circle with A identifies the region where C_P shows the strongest maximum.

along isotherms and isobars (Fig. 3.4), where $\langle H \rangle \equiv \langle \mathcal{H} \rangle + P\langle V \rangle$ is the average enthalpy, $\langle \Delta H^2 \rangle$ the enthalpy fluctuations. We find two maxima at low P . At high- T the maxima are broader and weaker than those at low- T . As discussed in Ref. [129,130], the maxima at high T are related to maxima in fluctuation of the HB number N_{HB} , while the maxima at low T are a consequence of maxima in the number N_{coop} of cooperative HBs. The strong maxima at constant P $C_P^{\text{sMax}}(T)$ and constant T $C_P^{\text{sMax}}(P)$ overlap for all the considered pressures, and are more pronounced in the range $P \in [0.5; 0.6]$ and $T \in [0.06; 0.07]$. The weak maxima $C_P^{\text{wMax}}(P)$ and $C_P^{\text{wMax}}(T)$ increase approaching the LL spinodal and have their larger maxima at the same state points of the strong maxima, consistent with the occurrence of a critical point for a finite system (Fig. 3.4). The weak maxima overlap for all positive pressures, branching off at negative pressures. At negative pressures $C_P^{\text{wMax}}(P)$ bends toward the turning point of the TMD line, as discussed in section 6 and in Ref. [127]. Indeed, according to the relation

$$\left(\frac{\partial C_P}{\partial P} \right)_T = T \left(\frac{\partial P}{\partial T} \right)_{TMD} \frac{\partial^2 V}{\partial P \partial T} \quad (3.8)$$

in case of intersection between the locus of extrema $(\partial C_P / \partial P)_T = 0$ and the TMD line, it results that $(\partial P / \partial T)_{TMD} = 0$.

3.2.3 Thermal expansion coefficient

We calculate also the the thermal expansivity

$$\alpha_P \equiv \left(\frac{\partial \ln \langle V \rangle}{\partial T} \right)_P \quad (3.9)$$

along isotherms and isobars (Fig. 3.5). As for the other response functions, we find two locus of strong minima, $\alpha_P^{\text{sMin}}(P)$ and $\alpha_P^{\text{sMin}}(T)$ respectively along isotherms and isobars, showing a divergent behavior in the same region where we find the strong maxima of K_T and C_P . From this region two loci of weaker minima depart:

- We find that the locus of weak minima along isobars $\alpha_P^{\text{wMin}}(T)$ bends toward the turning point of the TMD.
- The locus of weaker minima along isotherms $\alpha_P^{\text{wMin}}(P)$, merges with the locus of maxima $\alpha_P^{\text{wMax}}(P)$ at the state point where the slope of both loci is $\partial P / \partial T \rightarrow \infty$.

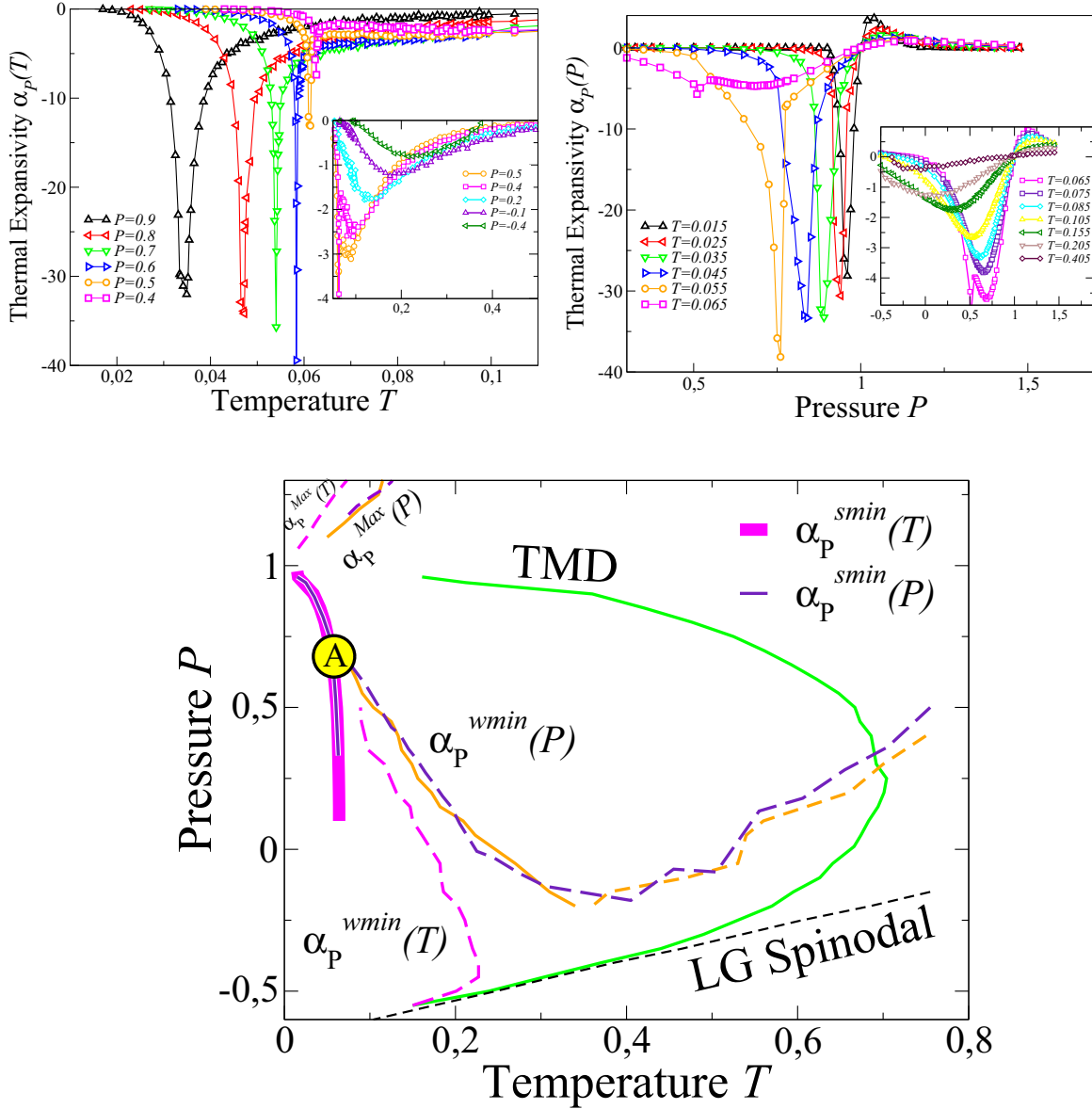


Figure 3.5: **Top-left panel:** loci of extrema in α_P along isobars. Weaker minima are shown in the inset. **Top-right panel:** loci of extrema in α_P along isotherms. Weaker minima are shown in the inset. **Bottom panel:** projection of extrema in α_P in $T - P$ plane. Orange lines are the loci of weaker extrema K_T^{wMax} and K_T^{min} (see bottom panel of Fig. 3.3). The large circle with A identifies the region where the divergent minimum in α_P is observed.

According to the thermodynamic relation, discussed in Appendix A,

$$\left(\frac{\partial\alpha_P}{\partial P}\right)_T = -\left(\frac{\partial K_T}{\partial T}\right)_P \quad (3.10)$$

we find that the locus of extrema in thermal expansivity along isotherms coincides, within the error bars, with the locus of extrema of isothermal compressibility along isobars.

3.3 The Widom line

All the loci of extrema of response functions converge toward the same region (labeled A in Fig. 3.3, 3.4 and 3.5). Moreover, all the maxima along these loci increase in their values by approaching the region A. Because the increase of response functions is related to the increase of fluctuations and this is, in turn, related to the increase of correlation length ξ , we calculate the spatial correlation function

$$G(r) \equiv \frac{1}{4N} \sum_{|\vec{r}_i - \vec{r}_l| = r} \langle \sigma_{ij}(\vec{r}_i) \sigma_{lk}(\vec{r}_l) \rangle - \langle \sigma_{ij} \rangle^2 \quad (3.11)$$

to estimate ξ . The states of the water molecule, as well as the density ρ , the energy E and the entropy S of the system, are completely described by the bonding variables σ_{ij} . The function $G(r)$ accounts for the fluctuations in ρ , E and S and allows us to evaluate the correlation length because the order parameter of the LLPT should be related to a linear combination of density and energy, as we will discuss later. The function $G(r)$ is, therefore, better than the density-density correlation function for estimating the correlation length of the system.

We observe an exponential decay of $G(r)$ at high temperatures in a broad range of pressures.

$$G(r) \sim e^{-r/\xi} . \quad (3.12)$$

Approaching the region A, the correlation function can be written as

$$G(r) \sim r^{d-2+\eta} e^{-r/\xi} \quad (3.13)$$

where d is the dimension of the system. When ξ is of the order of the system size, the exponential prefactor approaches a constant leaving the power-law as the dominant con-

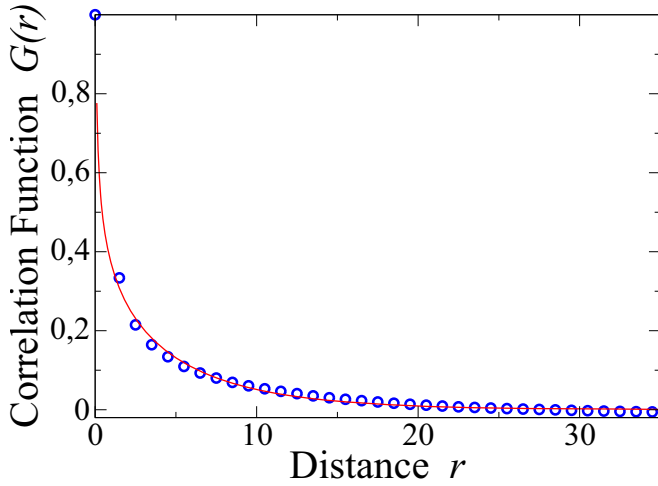


Figure 3.6: Correlation function $G(r)$ near the LLCP. Data are fitted with the power law in Eq. (3.13) with the fitting parameter $\eta \sim 0.25 \pm 0.04$, consistent with the critical exponent of Ising universality class $\eta = 1/4$ for $d = 2$.

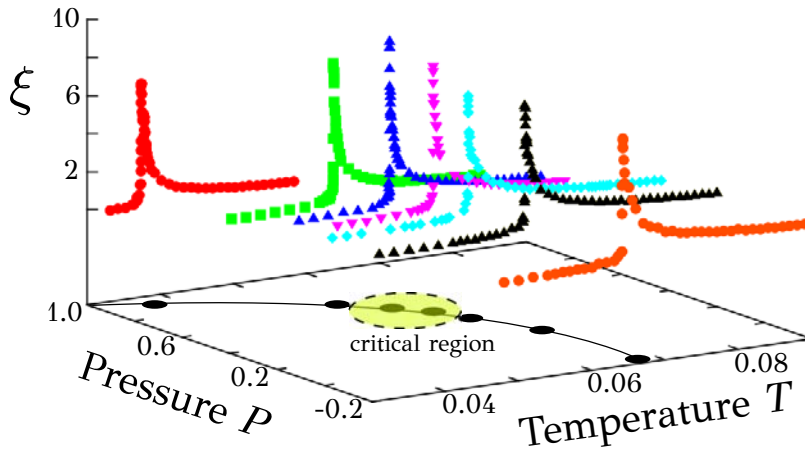


Figure 3.7: Correlation length ξ along isobars for $N = 10^4$ water molecules. The Widom line is identified by the locus of maxima in ξ originating from the LLCP.

tribution for the decay. Our calculations (Fig. 3.6) at $T \sim 0.06$ and $P \sim 0.6$ show that the behavior of $G(r)$ is consistent with the one expected near a critical point belonging to the Ising universality class in two dimension.

We estimate ξ using relations (3.12) and (3.13). Our calculations are consistent within the error bars with the values that can be calculated from the relation [131]

$$\xi^2 = \frac{\int r^2 G(r) dr}{\int G(r) dr}. \quad (3.14)$$

We observe that ξ has a maximum along isobars (Fig. 3.7), and the strongest maxima in ξ falls in the critical region, that coincides with the region A that we find based on our response function analysis (Figs. 3.3-3.5). The line of maxima coincides with the low- T locus of maxima in C_P for all pressures, and overlap with low- T extrema in K_T and α_P close the critical region. At higher P and lower T the maxima in correlation length marks

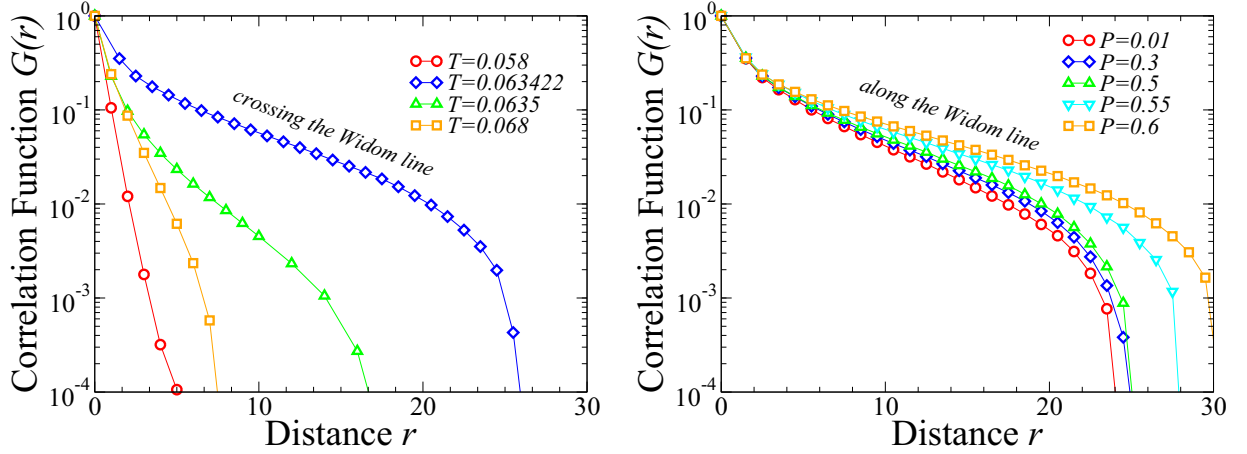


Figure 3.8: **Left panel:** correlation function $G(r)$ for different temperatures crossing the Widom line at low pressure ($P = 0.3$). The non monotonic behavior reflects the non monotonic behavior in correlation length ξ . **Right panel:** Correlation function $G(r)$ for different pressures along the Widom line up to the LLCP.

the occurrence of a first order phase transition, associate with a maxima in all response functions. At lower P the maxima in ξ identifies the Widom line of the system [24, 25, 27], observed as long as the metastable liquid phase exists. Along the Widom line a large deviation of $G(r)$ with respect the exponential decay is observed (Fig. 3.8).

3.4 The Liquid-Liquid 1st order phase transition and the Liquid-Liquid critical point

The observation of convergence of loci of stronger maxima and ξ^{Max} to the point A, and the increase of extrema along these loci is consistent with the identification of A with a LLCP at the end of a first-order LLPT line in the P - T phase diagram along which the density, the energy and the entropy of the liquid are discontinuous, as discussed in previous works [49, 89, 90, 129, 130, 132–137].

According to mixed-field finite-size scaling theory [138–141], a density-driven fluid–fluid phase transition is described by an order parameter

$$M \equiv \rho + su \tag{3.15}$$

where ρ represents the leading term, u is the energy density (both in internal units) and s is the field mixing parameter. Such linear combination is necessary in order to get the right

symmetry of the order parameter distribution, at the critical point, between the ordered and disordered phases. This order parameter accounts for the change in density and energy between the HDL and LDL close the critical point (Fig. 3.9).

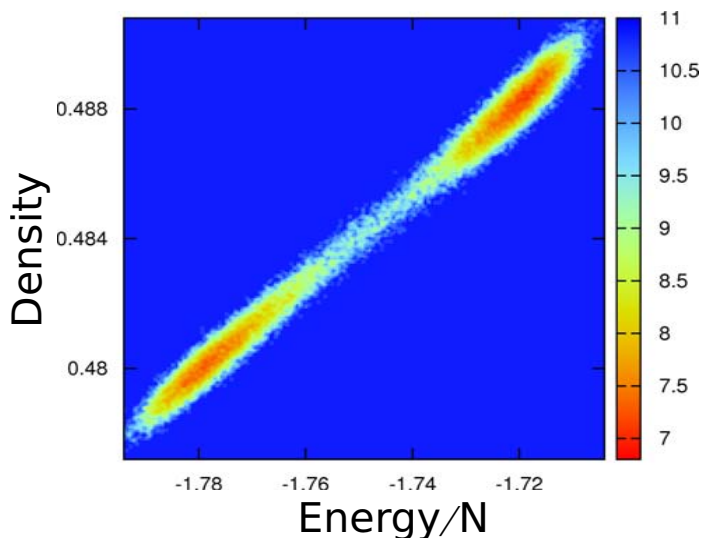


Figure 3.9: Color-coded Gibbs free energy $G/k_B T$ in the energy-density plane, close the liquid-liquid critical point. We calculate G from the relation $G/k_B T = -\ln P(E, \rho)$, where k_B is the Boltzmann constant and $P(E, \rho)$ is the probability distribution of states with given values of E and ρ . The Gibbs free energy under these conditions has two basins separated by a barrier $\Delta G \simeq k_B T$. This is the order of magnitude of the free-energy barrier expected near a critical point, where the system has enough thermal energy $k_B T$ to freely cross the barrier ΔG between the two coexisting phases. The order parameter M characterizing the phase transition is related to the line joining the two minima of Gibbs free energy.

At the critical point the probability distribution of M is $P_N(M) \propto \tilde{p}_d(x)$, i.e. scales as an universal function \tilde{p}_d , characteristic of the Ising fixed point in d dimensions, of $x \equiv B(M - M_c)$, where $B \equiv a_M^{-1} N^{\beta/d\nu}$, β is the critical exponent that governs M , ν is the critical exponent that governs ξ , both defined by the universality class, and a_M is a non-universal system-dependent parameter. We adjust B and M_c so that $P_N(M)$ has zero mean and unit variance.

By combining a set of 3×10^4 MC simulations for ~ 300 state points with $0.04 \leq T \leq 0.07$ and $0.3 \leq P \leq 0.8$ with the multiple histogram reweighting method [142–144] (see section 6), and tuning s , T and P we verify that in the vicinity of the state point A the calculated $P_N(x)$ has a symmetric shape with respect to $x = 0$ (Fig. 3.10). We find $s = 0.25 \pm 0.03$ for our range of N . The resulting critical parameters $T_c(N)$, $P_c(N)$ (Fig. 3.11) and the normalization factor $B(N)$ (Fig. 3.12) follow in fare agreement the expected finite-size behaviors with 2D Ising critical exponents [138–141]. From the finite-size analysis

we extract the asymptotic values $T_c = 0.0597 \pm 0.0001$ and $P_c = 0.555 \pm 0.002$, consistent with the state point A .

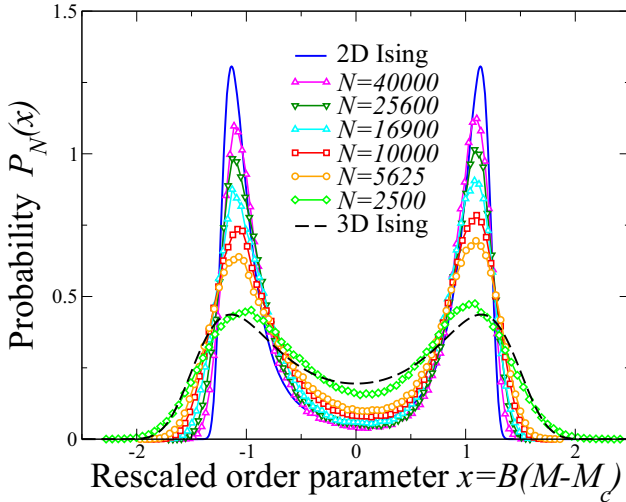


Figure 3.10: The size-dependent probability distribution P_N for the rescaled order parameter x , calculated for $T_c(N)$, $P_c(N)$ and $B(N)$ in Fig. 3.11 and Fig. 3.12, has a symmetric shape that approaches continuously (from $N = 2500$, symbols at the top at $x = 0$, to $N = 40000$, symbols at the bottom) the limiting form for the 2D Ising universality class (full line), maximizing the difference with the 3D Ising universality class (dashed line). Lines connecting the symbols are guides for the eye. Error bars are smaller than the symbols size.

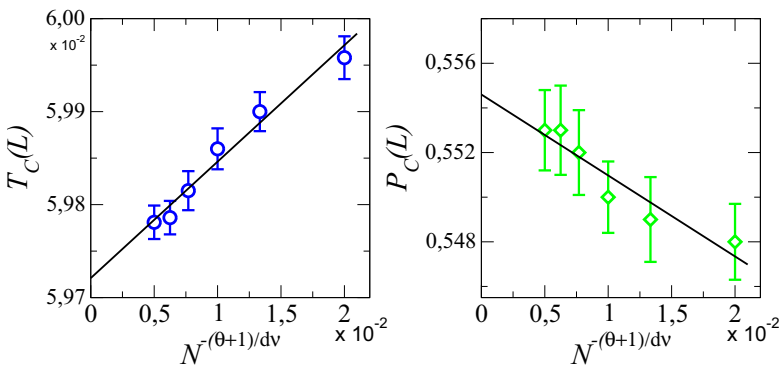


Figure 3.11: The size-dependent LLCP temperature $T_c(N)$ (a) and pressure $P_c(N)$ (b) (symbols), used for best-fitting P_N , extrapolate to $T_c \simeq 0.0597$ and $P_c \simeq 0.555$, respectively, following the expected linear behaviors (lines).

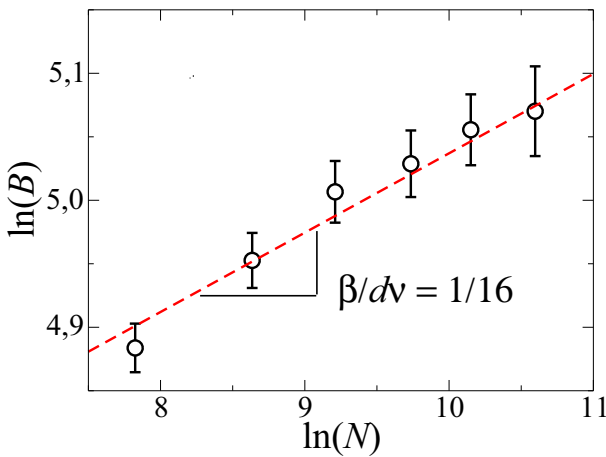


Figure 3.12: The normalization factor $B(N)$ (symbols) follows the power law function (dashed line) $\propto N^{\beta/d\nu}$. We use the $d = 2$ Ising critical exponents: $\theta = 0$ (correction to scaling), $\nu = 1$ and $\beta = 1/8$ (both defined in the text).

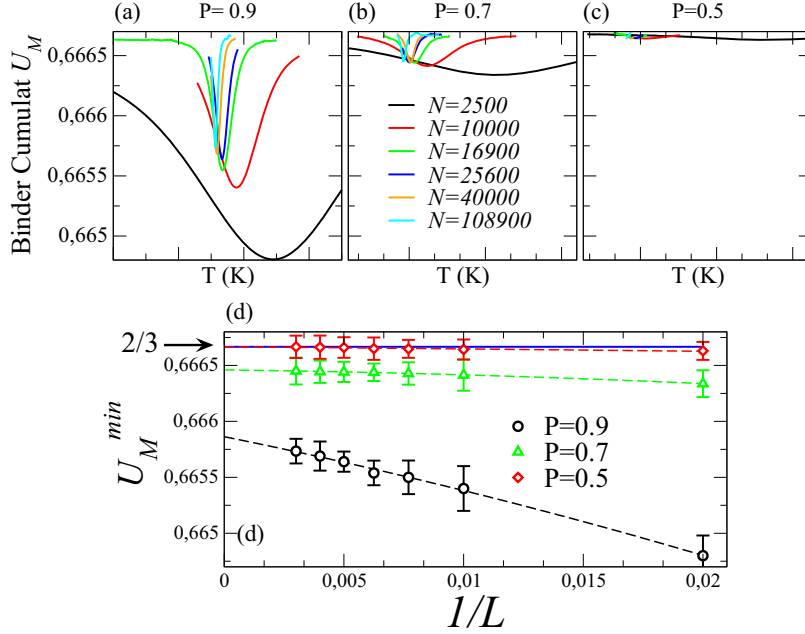


Figure 3.13: Binder cumulant U_M (defined in the text) of the order parameter M for different system sizes, calculated for three pressures: $P = 0.9$ in the panel (a), $P = 0.7$ in the panel (b), and $P = 0.5$ in the panel (c) slightly below the critical point. The curves are obtained changing almost continuously T with the histogram reweighting method. Panel (d): Scaling of the minima of the Binder cumulant. Blue line represents the limit value $2/3$ of binder cumulant, indicating the absence of a first-order phase transition in the thermodynamic limit. Error bars are calculated propagating the statistical error of the simulated histograms.

The presence of a 1st order transition ending in a critical point, with respect the order parameter M , is confirmed by the finite size analysis of the Binder cumulant [145, 146] of M

$$U_M = 1 - \frac{\langle M^4 \rangle_N}{3 \langle M^2 \rangle_N^2} \quad (3.16)$$

where the symbol $\langle \rangle_N$ refers to the thermodynamic average for a N water molecules system. U quantifies the bimodality in $P_N(M)$. The isobaric value of U_M shows a minimum at the temperature where $P_N(M)$ mostly deviates with respect to a symmetric distribution (Fig. 3.13). Minimum of U_M converges to $2/3$ in the thermodynamic limit away from a first order phase transition, while it approaches to a value $< 2/3$ at a first-order phase transition, where the bimodality of $P_N(M)$ indicates the presence of phase coexistence.

These results are consistent with the behavior of Gibbs free energy G (Fig. 3.14). The histogram reweighting method allows to calculate G for simulated state points, as described

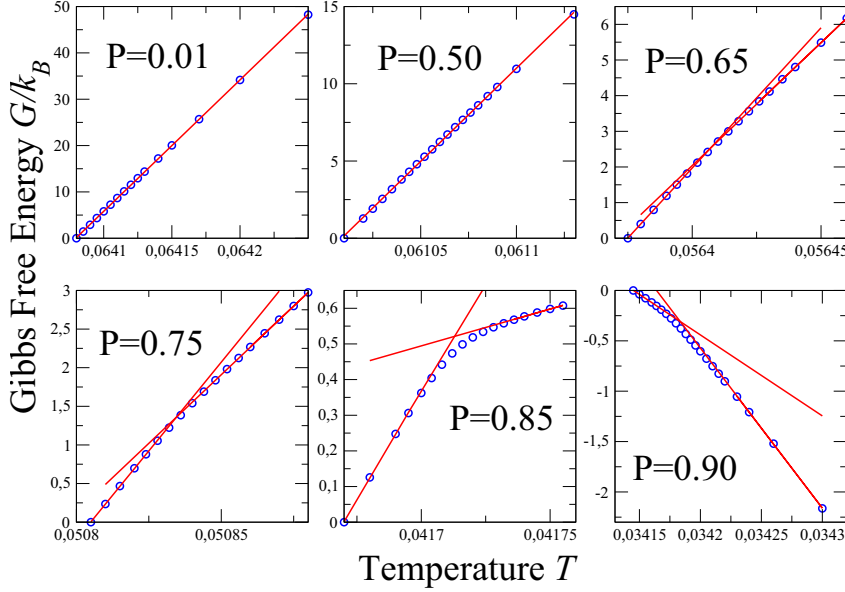


Figure 3.14: Gibbs free energy G along isobars, as function of T . Points are shifted so that $G = 0$ for the lowest T considered. Lines are linear fit of data considering only the tail of the curves. For $P > 0.65$, $G(T)_P$ bends, suggesting that in the thermodynamics limit $N \rightarrow \infty$ the derivative could be discontinuous.

in the caption of Fig. 3.14. In particular, we calculate G along isobars, for T crossing the loci of maxima in ξ and C_P . We find that the isobaric $G(T)_P$ bends for $P > 0.65$ (Fig. 3.14), consistent with the occurrence of a kink in the thermodynamic limit. This behavior would implies a discontinuity in entropy $S = \partial G / \partial T$, that would correspond to the latent heat of a first-order phase transition. Therefore, the calculation of G is consistent with the occurrence of a first-order phase transition at high P that disappears for $P \lesssim 0.65$, consistent with our estimate of a critical point occurring at $P_c \simeq 0.55$.

The distribution $P_N(N)$ adjust well to the data only for large N . We, therefore, perform a more systematic analysis. For each N , we quantify the deviation of the calculated $\tilde{p}(N)$ from the expected \tilde{p}_2 for the 2D Ising. Furthermore, due to the behavior of data for small N in Fig. 3.10, we calculate the deviation from the 3D Ising \tilde{p}_3 [138–141]. We estimate the Kullback-Leibler divergence [147]

$$D_d^{\text{KL}}(N) \equiv \sum_{i=1}^n \ln \left(\frac{\tilde{p}_{d,i}}{\tilde{p}_i(N)} \right) \tilde{p}_{d,i} \quad (3.17)$$

of the probability distribution $\tilde{p}_i(N)$ of x_i from the theoretical value $\tilde{p}_{d,i}$ for x_i , with n total number of points for x , and the Liu et al. deviation [148]

$$W_d(N) \equiv \frac{1}{n} \frac{\sum_{i=1}^n \sqrt{\tilde{p}_i(N)} |\tilde{p}_i(N) - \tilde{p}_{d,i}|}{\tilde{p}_{d,\text{peak}} - \tilde{p}_{d,x=0}} \quad (3.18)$$

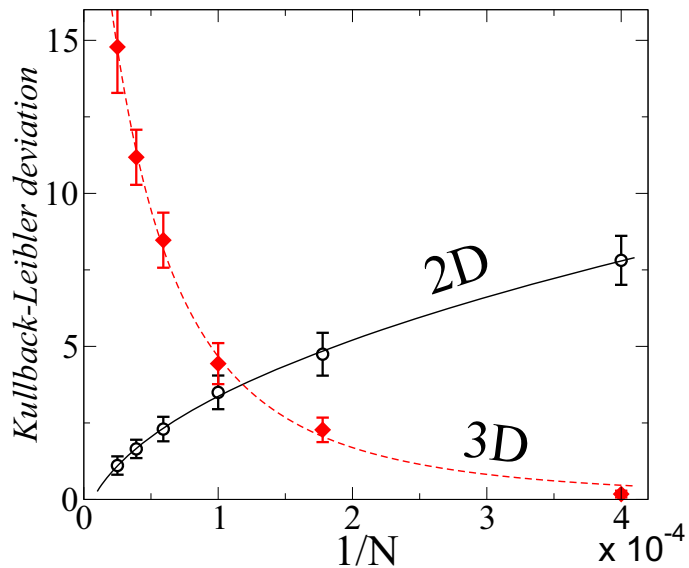


Figure 3.15: Kullback-Leibler divergence $D_d^{\text{KL}}(N)$ of the calculated $\tilde{p}(N)$ from the $d = 2$ (open symbols) and $d = 3$ (closed symbols) Ising universal function \tilde{p}_d , as function of the inverse of the number of water molecules N at constant $\rho \simeq \rho_c$. Lines are power-law fits.

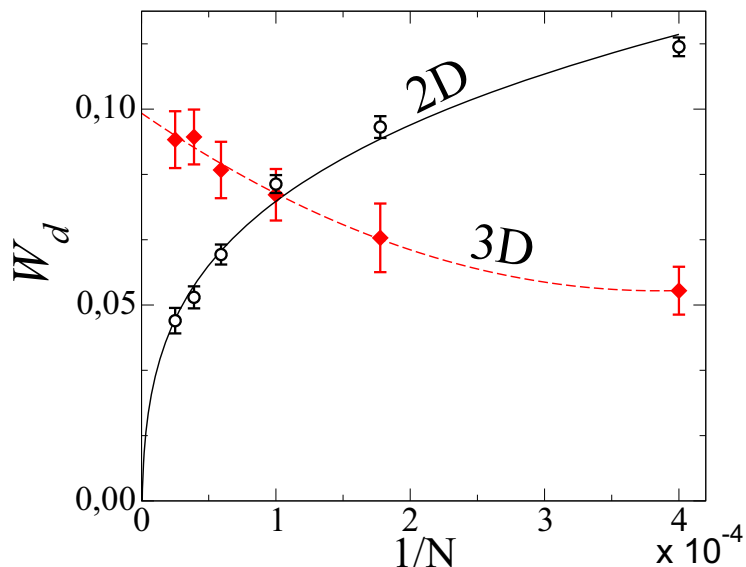


Figure 3.16: Deviations W_d (defined in the text) of the calculated $\tilde{p}(N)$ from the $d = 2$ and $d = 3$ Ising critical distributions with same symbols as in Fig. 3.15. Lines are power law fits.

with $\tilde{p}_{d,\text{peak}} - \tilde{p}_{d,x=0}$ difference between the distribution peak and its value at $x = 0$ (Fig. 3.15 and Fig. 3.16).

We confirm $s \simeq 0.25$ for \tilde{p}_2 and find $s = 0.10 \pm 0.02$ for \tilde{p}_3 for our range of N . For both D_d^{KL} and W_d , with $d = 2$ and $d = 3$, we find minima that become stronger for increasing N and are always close to $T_c \simeq 0.06$ and $P_c \simeq 0.55$, i.e. at approximately constant ρ_c . We find that D_2^{KL} and W_2 decrease with increasing N , vanishing for $N \rightarrow \infty$ (Fig. 3.15 and Fig. 3.16). Therefore, for an infinite monolayer confined between hydrophobic walls separated by $h \approx 0.5$ nm, the system has a LLC that belongs to the 2D Ising universality class, consistent with our coarse-graining of the monolayer in 2D.

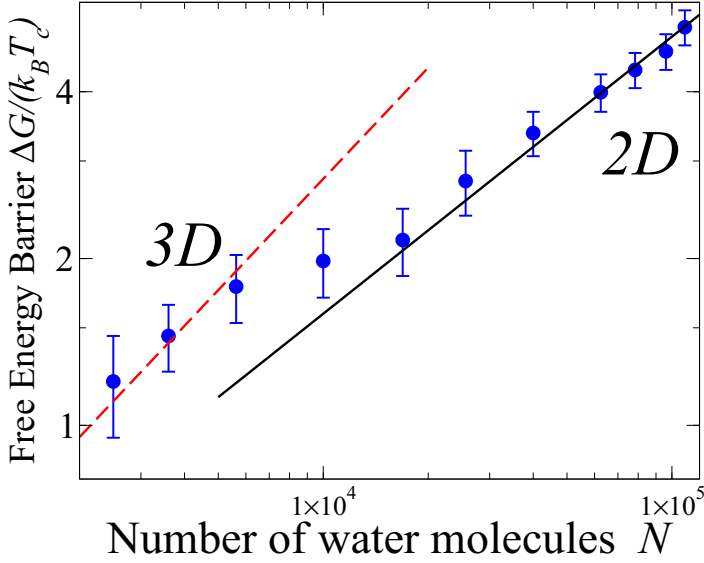


Figure 3.17: The free-energy cost to form an interface between the two liquids coexisting at the LLCPC scales as $\Delta G \propto N^{\frac{d-1}{d}}$ with $d = 3$ for $N < 10^4$ and $d = 2$ for $N > 10^4$.

However, by increasing the confinement, i.e. reducing N and L at constant ρ , D_2^{KL} and W_2 become larger than D_3^{KL} and W_3 , respectively. For $N = 2500$ we find that both D_3^{KL} and W_3 have values approximately equal to those we calculate for a system ten times larger, with $D_3^{\text{KL}} \simeq 0$. In other words, by increasing the confinement of the monolayer at constant ρ , the LLCPC has a behavior that approximates better the bulk [23, 36–38, 46, 149], with a crossover between 2D and 3D-behavior occurring at $N \simeq 10^4$.

This dimensional crossover is confirmed by the finite-size analysis of the Gibbs free energy cost $\Delta G/(k_B T_c)$ to form an interface between the two liquids in the vicinity of the LLCPC, calculated as

$$\Delta G(N) \equiv -k_B T_c(N) [\ln P_N(x = 0) - \ln P_N(x_{\text{MAX}})] \quad (3.19)$$

with P_N reaching a maximum at x_{MAX} . This quantity is expected to scale as $\Delta G \propto N^{\frac{d-1}{d}}$. We find that our data can be fitted as $N^{\frac{2}{3}}$ for small sizes and as $N^{\frac{1}{2}}$ for large sizes with a crossover around $N = 10^4$ (Fig. 3.17). Considering the value of the estimated ρ_c in real units ($\simeq 1\text{g/cm}^3$) [134, 135], the corresponding crossover wall-size is $L \simeq 25$ nm.

Our rationale for this dimensional crossover at fixed h is that, when h/L increases, the characteristic way the critical fluctuations spread over the system, i.e. the universality class of the LLCPC, resembles closely the bulk because the asymmetry among the three spatial dimensions is reduced. A similar result was found recently by Liu et al. for the gas-liquid critical point of a Lennard-Jones liquid confined between walls by fixing L and varying h [148]. However, in the case considered by Liu et al. the crossover was expected because

the number of layers of particles was increased from one to several, making the system more similar to the isotropic 3D case. Here, instead, we consider always one single layer, changing the proportion h/L by varying L instead of h . Therefore, it could be expected that the system belongs intrinsically to the 2D universality class for any L .

Furthermore, the extrapolation of the results for the LJ liquid to the case of a monolayer with $h/r_0 \simeq 1.7$, as in our case, would predict a dimensional crossover at $L/h \lesssim 5$ [148]. For our water monolayer, instead, we find the crossover at $L/h \simeq 50$, i.e. one order of magnitude larger than the LJ case. This implies that the presence of a cooperative HB network and its low coordination number, the main differences between water and a LJ fluid, enhance drastically the spreading of the critical fluctuations along a network that, at least for the first shell, is similar to the one in 3D, lifting the effective dimensionality of the confined monolayer.

Chapter 4

Percolation approach to supercooled water

In the past years different percolating description of water been proposed [152–155] where the dynamic is led back to behavior of cluster of H-bonded molecules. In this chapter we propose a site-bond correlated description, based on a mathematical mapping between physical and geometric properties [156–159], to characterize the formation of HB network in relation with the regions of correlated water molecules.

Before to introduce the the percolation description of the model we briefly resume how percolation theory and statistical physics have woven together. The general problem of the percolation theory concerns with the study of geometrical objects randomly placed, with an occupation probability p , on a d -dimensional lattice. Such objects have a characteristic connectivity radius r such as two objects communicate if their distance is smaller than r . A contiguous region of connected objects is a cluster. Percolation theory studies the geometrical properties of such clusters and, in particular, when the cluster spans the space becoming infinite. It is well known that the percolation problem on large lattices displays the features of a system undergoing a second-order phase transition where p is the order parameter. Indeed it is possible to define quantities which diverge (or vanish), with characteristic critical exponents, as the critical occupation probability is approached [131,160]. It is precisely this aspect of percolation that makes it interesting in the study of critical phenomena and, more in general, in statistical physics.

Theory of condensation proposed by Mayer [161,162] and further developed by Frenkel [163,164], was one of the first attempt to introduce the idea of clusters of particles in the description of phase transition and nucleation. This phenomenological theory, based on perfect gas of clusters model, expresses the equation of state as series expansion in the density in the form $P = \sum_s n_s k_B T$, where n_s is the distribution of clusters of s particles per unit volume (and k_B the Boltzmann constant). Different clusters, assumed

to be compact region of interacting particles, are treated as non interacting objects. In order to recover the critical behavior of particles, Fisher [165] modified the theory listing the properties of such droplets in proximity of LG critical point [131, 166]: i) an infinite droplets is formed only at the critical point; ii) the order parameter of the phase transition is related to the size of the infinite droplet; iii) the compressibility (or susceptibility for magnetic systems) of the order parameter is proportional to mean cluster size; iv) the statistical correlation length ξ , quantifying the spatial extent of thermal fluctuations, is proportional to the average radius of the clusters ξ_c . This picture recovered the expected scaling relations at the critical point, but it remained the problem how to calculate such clusters (or droplets). Even if the simplest definition of cluster could be the compact region of interacting particles - n.n. occupied sites - it has been shown by Sykes and Gaunt [171] that thermodynamic and geometrical critical points do not coincide for the Ising model in three dimensions. After all, using such definition, at infinite temperature we still have cluster with size bigger than one despite that $\xi = 0$. In 1969 and 1972 Kasteleyn and Fortuin (KF) shown that it is possible to map a ferromagnetic Potts model onto a corresponding percolating model [156, 157]. Using a site-bond correlated description of the Ising model, based on the KF theory, Coniglio and Klein [158, 159] (CK) proved the equivalence between the thermodynamic and geometrical critical behaviors. They shown that the critical point (Curie point) coincides with the percolating threshold, that ξ and ξ_c diverge with same critical exponent ν and that the susceptibility and the mean cluster size diverge with the same critical exponent γ . For magnetic system the CK description was further improved by Swendsen and Wang [111] with the introduction of ghost spin external to the system, in order to avoid unphysical percolation lines spreading from the Curie point.

4.1 Site-bond correlated percolation

Following the CK approach, we want to superimpose a percolating description on our water cell model. In general, we can say that it is possible to map the physical system in a percolating system as long as it is possible to find a mathematical function, depending on the Hamiltonian, allowing to build cluster of statistically correlated degrees of freedom. It means that two interacting variables σ have a certain probability, depending on the specific interaction, to belong to the same cluster. In our model the HB interaction is described by two terms, with coupling constants J and J_σ , so we anticipate finding two probabilities, namely p_J and p_{J_σ} . In order to calculate such probabilities lets consider the enthalpy of

the system

$$H = U(r) - J_{\text{eff}} \sum_{\langle i,j \rangle} n_i n_j \delta_{\sigma_{ij}, \sigma_{ji}} - J_{\sigma} \sum_i n_i \sum_{(k,l)_i} \delta_{\sigma_{ik}, \sigma_{il}} + P v_0 \quad (4.1)$$

where we put $J_{\text{eff}} = J - P v_{HB}$. In the NPT ensemble the partition function of the system is

$$Z(\beta, P) = \sum_{\{\sigma\}\{r\}} e^{-\beta H} \quad (4.2)$$

where the sum is over all the possible configurations of variables $\{\sigma\}$ and of cell dimension $\{r\}$. Eq. 4.2 can be rewritten as

$$Z(\beta, P) = e^{-\beta P v_0} \sum_{\{r\}} e^{-\beta U(r)} \times Z_{\{\sigma\}} \quad (4.3)$$

with

$$\begin{aligned} Z_{\{\sigma\}} &= \sum_{\{\sigma\}} e^{\beta J_{\text{eff}} \sum_{\langle i,j \rangle} n_i n_j \delta_{\sigma_{ij}, \sigma_{ji}}} \times e^{\beta J_{\sigma} \sum_i n_i \sum_{(k,l)_i} \delta_{\sigma_{ik}, \sigma_{il}}} = \\ &= \sum_{\{\sigma\}} \prod_{\langle i,j \rangle} [1 + (e^{\beta J_{\text{eff}}} - 1) n_i n_j \delta_{\sigma_{ij}, \sigma_{ji}}] \times \prod_{i=1}^N \left\{ 1 + n_i \prod_{(k,l)_i} [1 + (e^{\beta J_{\sigma}} - 1) \delta_{\sigma_{ik}, \sigma_{il}}] \right\} \end{aligned} \quad (4.4)$$

where $\prod_{\langle i,j \rangle}$, $\prod_{i=1}^N$ and $\prod_{(k,l)_i}$ extend respectively over all next neighbors, all sites and all variables σ of a specific site. To simplify calculations we consider an homogeneous system, such that all cells are occupied ($n_i = 1$ for $i = 1 \dots N$), so eq. 4.4 reduces to

$$Z_{\{\sigma\}} = \sum_{\{\sigma\}} \prod_{\langle i,j \rangle} [1 + (e^{\beta J_{\text{eff}}} - 1) \delta_{\sigma_{ij}, \sigma_{ji}}] \times \prod_{i=1}^N \prod_{(k,l)_i} [1 + (e^{\beta J_{\sigma}} - 1) \delta_{\sigma_{ik}, \sigma_{il}}] . \quad (4.5)$$

The partition function can be equally expressed as a sum over all possible clusters of a given configuration σ [172]. A cluster C is a region of σ variables connected by artificial bonds. The bonds do not affect the interaction energy or the particles distribution, they just define the connectivity between variables σ , independently on the specific bonding state of connected variables [173]. The variables σ , in our coarse-grain description, do not depend on the average distance r between n.n. water molecules (as long as we are in the liquid phase), so we carry out such mapping only on the term $Z_{\{\sigma\}}$. We focus on the first term of the eq. 4.5, $1 + (e^{\beta J_{\text{eff}}} - 1) \delta_{\sigma_{ij}, \sigma_{ji}}$. We can interpret 1 as the factor we have in case of non-bonded configuration, and $(e^{\beta J_{\text{eff}}} - 1) \delta_{\sigma_{ij}, \sigma_{ji}}$ as the factor in case we have a bond b_J between n.n. σ . Similarly, considering the second term of eq. 4.5, for each water molecule

occurs the terms 1 and $(e^{\beta J_\sigma} - 1)\delta_{\sigma_{ik},\sigma_{il}}$, the first for non-bonded configuration and the second for bonded configuration via bond b_{J_σ} . If two σ are connected through a bond, they belong to same cluster. A given configuration $\{\sigma\}$ generally contains a large number of clusters, included isolated variables, each one with q possible states. Actually, in the summation of all σ states, only clusters of variables σ in the same bonding state will give a nonzero contribution. Hence, we can rewrite 4.5 as sum on the cluster configurations $\{C\}$

$$Z_{\{\sigma\}} = \sum_{C \subseteq \{\sigma\}} (e^{\beta J_{\text{eff}}} - 1)^{b_J(C)} (e^{\beta J_\sigma} - 1)^{b_{J_\sigma}(C)} q^{n(C)} \quad (4.6)$$

where $b_J(C)$ and $b_{J_\sigma}(C)$ are respectively the number of bonds b_J and b_{J_σ} in the cluster C , and $n(C)$ the number of cluster of a given configuration $\{\sigma\}$. In particular, choosing the energy to be 0 at $T = 0$ [156, 157], i.e. subtracting the maximum number of interactions J and J_σ , we can write

$$Z_{\{\sigma\}} = [e^{\beta(2J_{\text{eff}} + 6J_\sigma)}]^{N} \sum_{C \subseteq \{\sigma\}} p_J^{b_J(C)} (1 - p_J)^{2N - b_J(C)} p_{J_\sigma}^{b_{J_\sigma}(C)} (1 - p_{J_\sigma})^{6N - b_{J_\sigma}(C)} q^{n(C)} \quad (4.7)$$

where

$$p_J = 1 - e^{-\beta J_{\text{eff}} \delta_{\sigma_{ij}, \sigma_{ji}}} \quad (4.8)$$

$$p_{J_\sigma} = 1 - e^{-\beta J_\sigma \delta_{\sigma_{ik}, \sigma_{il}}} . \quad (4.9)$$

Such transformation replaces each pair n.n. σ variables with a bond on the equivalent system with a probability p_J or p_{J_σ} . In the general case where not all cells are occupied we have $p_J = 1 - \exp(-\beta J_{\text{eff}} n_i n_j \delta_{\sigma_{ij}, \sigma_{ji}})$. The quantities $(1 - p_J)$ and $(1 - p_{J_\sigma})$ are simply the probabilities that no bonds, respectively b_J or b_{J_σ} , exists between n.n. σ and the number of missing bonds are respectively $2N - b_J(C)$ and $6N - b_{J_\sigma}(C)$. In such a way the system is described via site-bond correlated percolation where the clusters act as independent degrees of freedom.

Ultimately we have to say that even if the CK mapping between geometry and thermodynamics is not extensible to metastable systems [174], ours is not the case. The proposed model is adapted to describe highly confined water where crystal phase is no longer permitted [114–116], hence in this approximation the two observed liquid phase are thermodynamically stable.

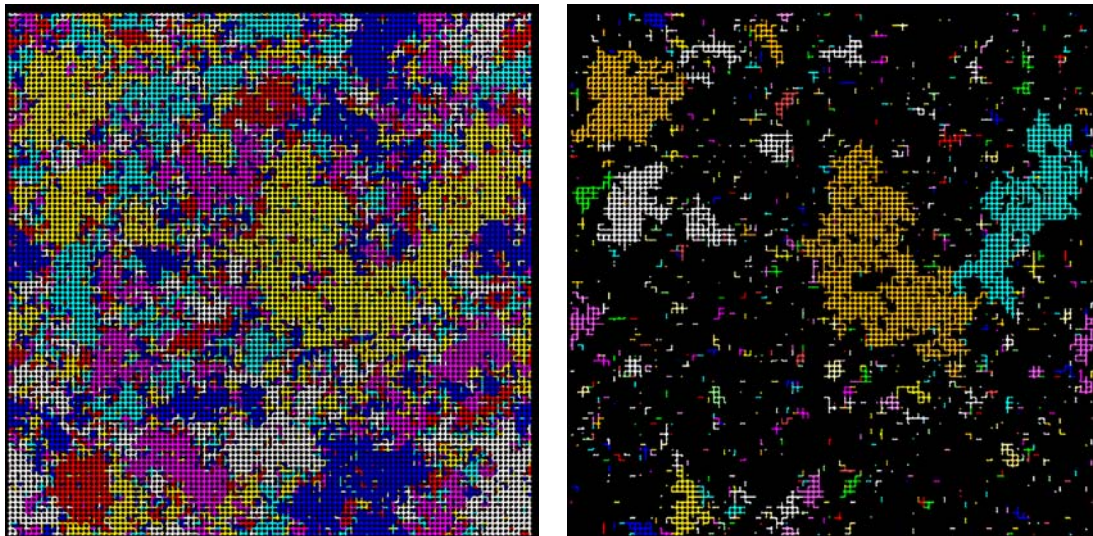


Figure 4.1: **Left panel:** σ configuration for $N = 10^4$ water molecules for $P = 0.6$ and $T = 0.058$. Each color represents a different σ state. **Right panel:** we select all variables in the same bonding state (yellow points of the left panel) and build the clusters of correlated variables (region with the same color) following the prescription given in the text.

4.2 Percolation probability

The size s of a cluster is defined as the number of σ variables belonging to the cluster. Each four σ variable, on average, an entire water molecule belongs to a cluster. In figure 4.1 we show clusters of a specific configuration. The occurrence of a percolating transition is marked by the appear of a percolating cluster, i.e. a clusters connecting two opposite sides of the system. The probability for an arbitrary site to belong to the percolating cluster is

$$P_\infty = 1 - \sum_s sn_s \quad (4.10)$$

where n_s is the average number of non-percolating clusters of size s per site. The probability that an arbitrary variable is part of a cluster of size s is given by $n_s s$. Therefore the probability that an arbitrary variable belongs any non-percolating cluster is $\sum_s n_s s$, as expressed in Eq. (4.10). The quantity P_∞ represents the order parameter for the percolating transition.

The quantity P_∞ increases from 0 to 1 at a temperature that is function of P and displays a clear finite-size effect at any P : its change with T becomes sharper for increasing size L (Fig. 4.2). In particular it approaches a discontinuous change for $P < 1$.

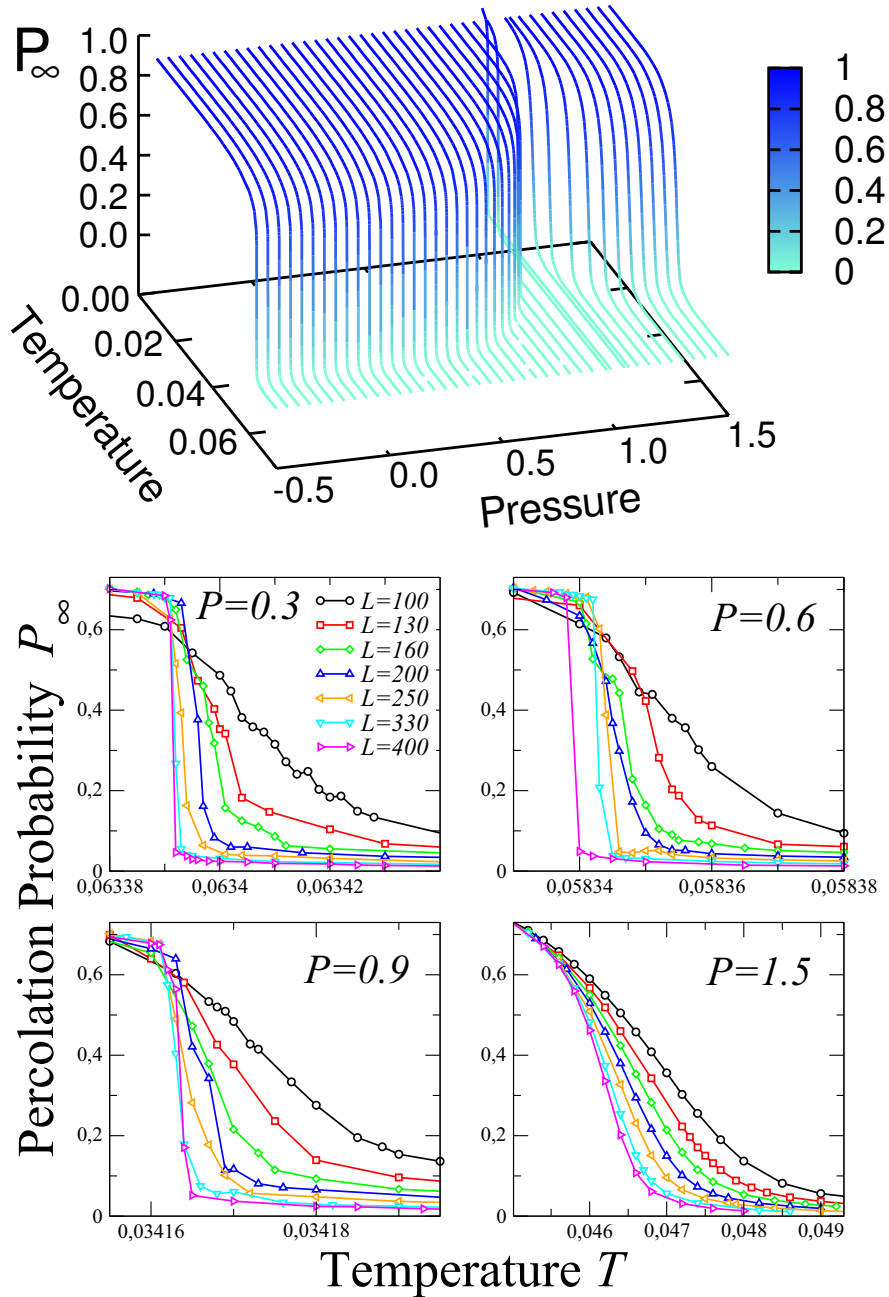


Figure 4.2: **Top panel:** percolating probability P_∞ as function of T for $N = 10^4$ water molecules. The color code along lines represents the value of P_∞ . Lines join simulated state points - $\simeq 150$ for each value of P with a statistic of $\simeq 10^4$ independent configurations. **Bottom panels:** variation of the percolation order parameter P_∞ with temperature T for systems with $L \times L$ molecules, with L going from 100 to 400, for different pressures P . For $P < 1$ the transition appears almost discontinuous, while it becomes smooth for $P > 1$.

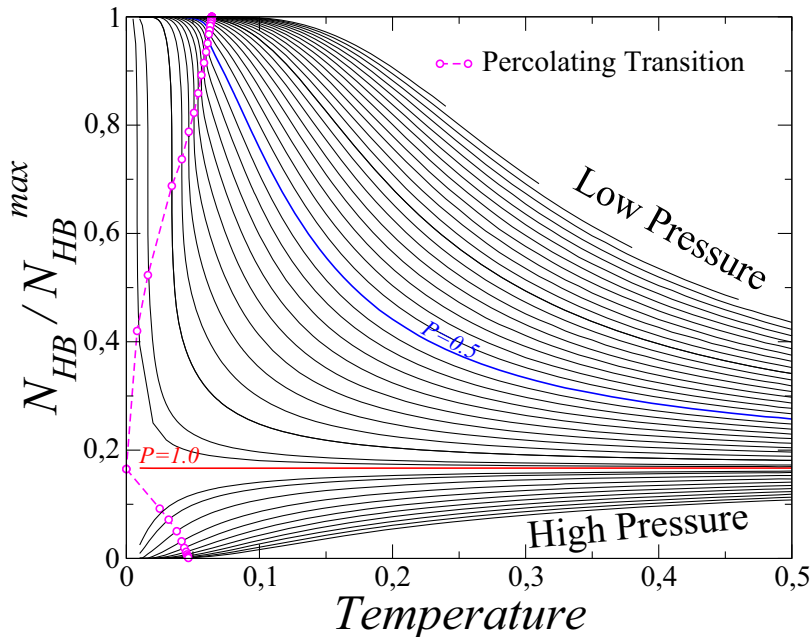


Figure 4.3: Number of HB (normalized to 1) as function of T for $N = 10^4$ water molecules. Lines join simulated state points ($\simeq 150$ for each isobar). Circles mark the occurrence of the percolating transition.

Defining the percolation threshold at fixed P as the T where $P_\infty = 0.5$, we locate the locus of percolation thresholds for different P , the percolation line, in the P - T plane (Fig. 4.4).

For $P < 1$ the percolation line has a negative slope that decreases in absolute value for increasing P , while for $P > 1$ the slope is positive and increases for increasing P . The percolation line extends down to the stability limit of stretched liquid at negative pressure.

Next we show that the percolation line marks the threshold for the formation of a structured network of HBs. N_{HB} increases monotonically in this range of pressures (Fig. 4.3). In particular for $1 < P \lesssim 0.5$ the clusters percolate when the number of HBs increase sharply. The jump in N_{HB} points out an abrupt decrease of density (Fig. 3.1), due to the thermodynamic phase transition between HDL and LDL.

For $P < 0.5$ the HB network is gradually formed and the percolation threshold occurs when the system is highly H-bonded (Fig. 4.5). In this thermodynamic conditions the spanning clusters are associated to a local tetrahedral reordering of HB network. At these pressures the percolation line coincides with the locus of strong maxima in isobaric specific heat and the LL Widom line. When the pressure is approaching the LLC value from lower pressures, the same locus approximate also the strong maxima in isothermal compressibility and the absolute value of the thermal expansivity, as described in Chap. 3.

At $P < 0.5$ the percolation line could be identified with the "Kertész line" or "Coniglio-Klein line" [175, 176], due to the KF percolating approach. The Kertész line starts at the

critical point independently on the dimensionality of the system and no thermodynamic singularity occurs along this line. It is still under debate if the Kertész line has corresponds to a thermodynamic locus. In particular, it has been proposed that this line exists in the supercritical phase of simple fluid [177, 178] and it is related to the locus where vanishes the surface tension of droplets made of the denser fluid. Our results here suggest that the Kertész line coincides with the Widom line of the LLCPP for supercooled water.

We find the percolation lines also for $P > 1$ (Fig. 4.2 and 4.4). At these pressures the percolation line is characterized by a smooth change in the order parameter P_∞ . At these pressures the HB formation is enthalpically disadvantageous and the percolating transition indicates the break down in N_{HB} (Fig. 4.3). This part of the percolation line at $P \geq 1$ represent a second Kertész line extending from a percolation critical point at $T = 0$ and $P = 1$ up to $P = \infty$. Indeed, at $T = 0$ the system is frozen with all σ in the same bonding state and the CK approach falls into bond-percolation problem, undergoing a critical percolation transition [131].

The analysis of probability to find a cluster of size s (Fig. 4.5), confirms the hypothesis on the different mechanism underlying the percolating transition for low pressures (below $P \sim 0.5$) and high pressures ($0.5 \lesssim P < 1$). Clusters of size 1 represent isolated uncorrelated variables σ . Clusters of size 2 are given by two correlated variables σ connected by bond of type b_J or b_{J_σ} . In particular, the analysis of clusters of size 2 reveals that at low P they are composed in large majority by b_J bonds (J -interacting σ), related to the average number of correlated HB. For such pressures, the derivative of 2-size clusters show maxima in correspondence to the C_P maxima, elucidating the connection between 2-size cluster fluctuation and N_{HB} fluctuations. On the contrary, at high P , 2-size clusters are mostly composed by bond b_{J_σ} (J_σ -interacting σ).

More in general all s -size clusters for $P < 0.5$ are mainly composed of b_J bonds, while for $P > 0.5$ they are mainly composed of b_{J_σ} bonds. Hence, the percolation mechanism is leaded by b_J bonds for $P < 0.5$ and by b_{J_σ} bonds for $P > 0.5$.

4.3 Cluster distribution

At the percolation threshold a spanning cluster appears as a fractal object, with linear size comparable with L . Along the percolation lines we observe power law molecule cluster

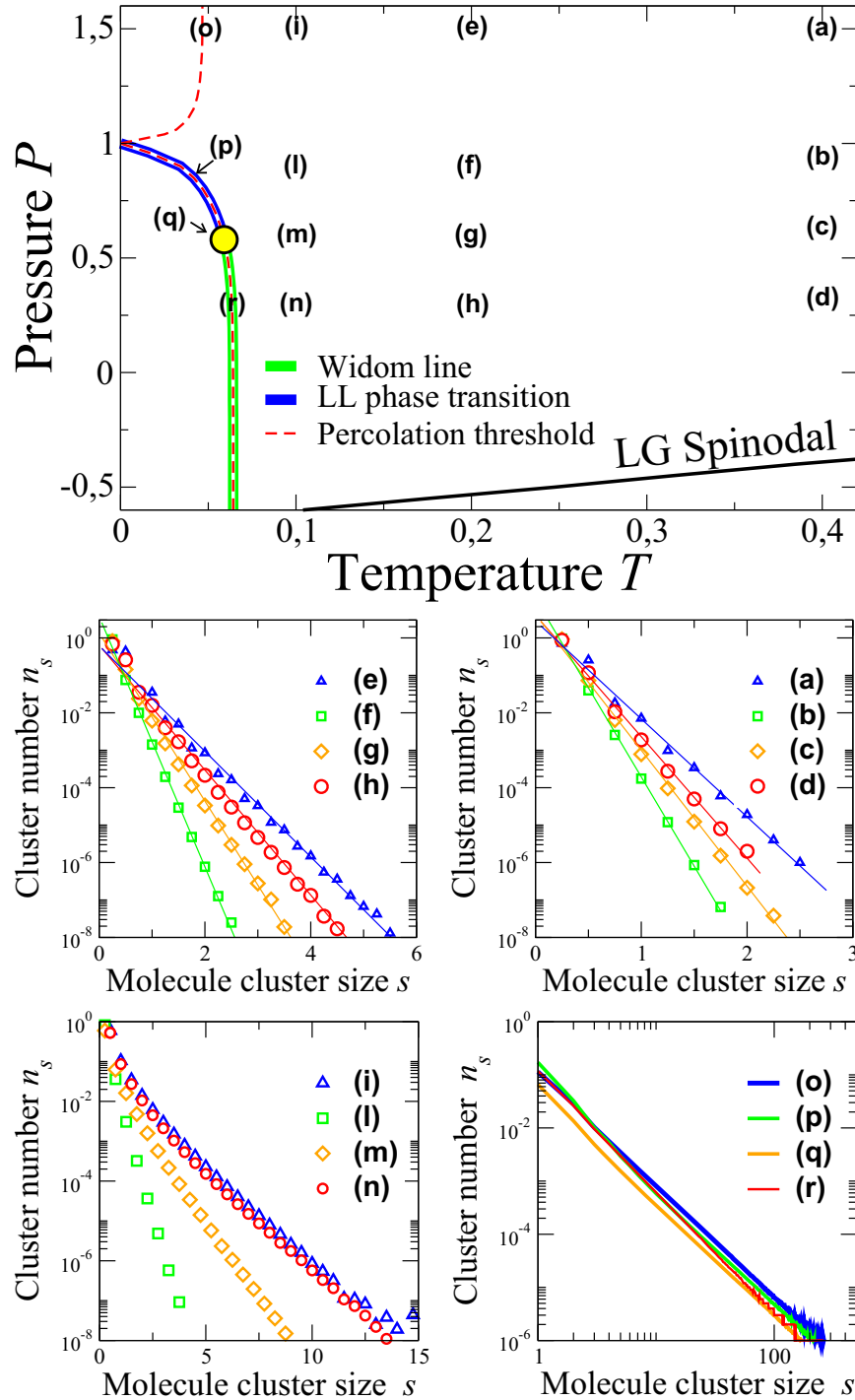


Figure 4.4: **Top panel:** Percolation lines in the $T - P$ plane, for $N = 10000$ system size, compared with LL-phase transition line and Widom line calculated with thermodynamic analysis [179]. Yellow circle identifies the thermodynamic critical point. Letters refer to the thermodynamic state points whose molecule cluster distribution n_s is shown in the bottom panels. **Bottom panels:** we show In particular we show data for pressures $P = 1.5$, $P = 0.9$, $P = 0.6$ and $P = 0.3$ and temperatures $T = 0.4$, $T = 0.2$, $T = 0.1$ and the percolation temperature. Lines in bottom panels are exponential fits of the data. At the percolation threshold data are fitted with power law function giving $\tau = 2.23 \pm 0.05$ for $P = 0.3$ (r), $\tau = 2.06 \pm 0.03$ for $P = 0.6$ (q), $\tau = 2.03 \pm 0.03$ for $P = 0.9$ (p), $\tau = 2.05 \pm 0.02$ for $P = 1.5$ (o).

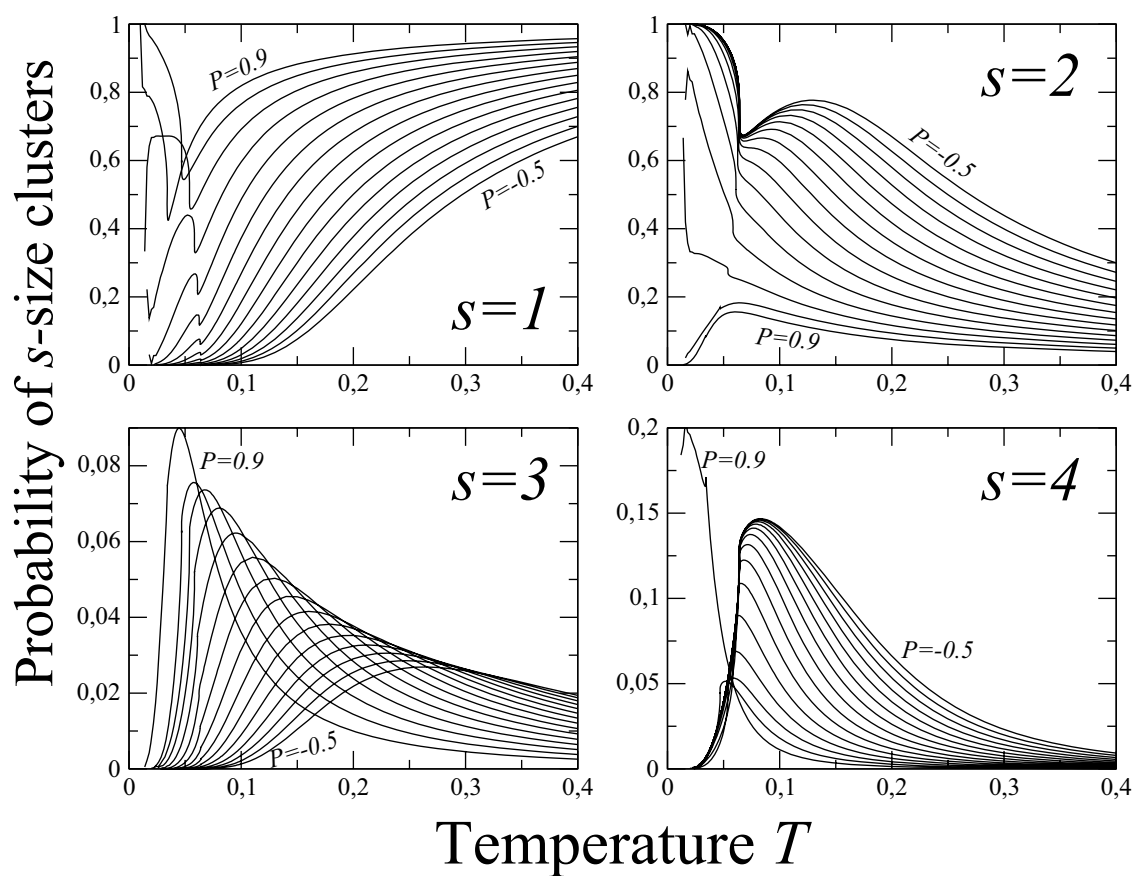


Figure 4.5: Temperature dependence of probability to have cluster of size $s = 1$, $s = 2$, $s = 3$ and $s = 4$, for $P \in [-0.5; 0.9]$. Intermediate curves are separated by $\Delta P = 0.1$. Lines join simulated data (~ 150 for each line).

distribution ¹ (Fig. 4.4), corresponding to the absence of a characteristic size s for the clusters, according to the relation

$$n_s \propto s^{-\tau} \quad (4.11)$$

The exponent τ is related to the fractal dimension D of the clusters by the relation [131]

$$\tau = 1 + \frac{d}{D} \quad (4.12)$$

where $d = 2$ is the effective dimensionality of the system. We find $\tau \sim 2.23 \pm 0.05$ for $P \lesssim 0.5$. For $P \sim P_C$ (~ 0.6) it results $\tau = 2.06 \pm 0.03$ that is consistent with the expected value for Ising universality class in two dimensions [180]. Increasing the pressure τ approaches to ~ 2.0 for $P = 1$. This is consistent with clusters that become more compact as the pressure is increased above the thermodynamic critical pressure. For $P > 1$ we find $\tau \sim 2.05 \pm 0.02$ in agreement with site percolation universality class. Along the LL coexistence line the cluster distribution decays as power law unlike simulation results on simple fluid [166] where no geometrical critical behavior is observed along the LG coexistence line. This result could be related with the cooperative behavior of HB interaction that enhance the spread of fluctuations along the HB network.

Moving away from the percolation threshold at higher T , n_s deviates from the power law behavior (see data **(i)**, **(l)**, **(m)** and **(n)** in Fig. 4.4) and the system appears strongly heterogeneous with the coexistence of large and small clusters. By further increasing T the cluster distribution is well described by exponential decay function $n_s \propto \exp(-s)$ (Fig. 4.4). These temperatures are characterized by a large quantity of small clusters and by a structural correlations among the molecules that extends only to short distances.

At T below the percolation threshold the network of tetrahedrally ordered molecules is built up and the majority of the molecules belongs to a single percolating cluster. and the distribution n_s becomes again exponential. A significant number of small clusters is still present pointing out the heterogeneity of the system.

Cluster configuration at different values of T along the critical isobar are shown in Fig. 4.6.

It is interesting to note that various percolation studies in supercritical water [167–169]

¹We focus on molecule cluster and not on cluster of variables σ for two reasons: i) variables σ are internal degrees of freedom of a molecule having no direct correspondence with a physical observable while we are interested to know the number of correlated molecules; ii) near the percolation threshold the distribution of σ -clusters is bimodal whenever $|J_{\text{eff}}| \gg J_\sigma$ because odd-size σ -clusters are strongly inhibited, introducing a spurious effect on the cluster distribution.

and supercritical water-CO₂ mixture [170], based on a definition of cluster as contiguous region of HB-interacting molecules, show the presence of a percolation line which divide two structurally different fluids. Along this line the distribution of clusters follows a power law decay as we observe at the LL Widom line.

4.4 Mean cluster size

In percolation theory, the physical quantity equivalent to the compressibility for fluid systems (or to the susceptibility for a magnetic system) is represented by the mean cluster size S [131]

$$S \equiv \sum_s s^2 n_s \quad (4.13)$$

that quantifies the average dimension of non-percolating clusters. The percolating transition matches with maxima in the mean cluster size S (Fig. 4.8), sharper for $P < 1$, broader and higher for $P > 1$. The maxima in S increase along the percolation line as T decreases and apparently diverge at $T = 0$ and $P = 1$, highlighting a possible percolating critical point. Moreover the maxima in S remain almost constant for $P \lesssim 0.6$ (in agreement with the thermodynamic critical pressure $P_C \sim 0.55$), showing an elbow in correspondence to the thermodynamic critical point (see the projection of S in the top panel of Fig. [?]) [179]. For $0.6 \lesssim P < 1$ the increase in S is stronger than at lower P as a consequence of the is related the HDL-LDL phase transition. The locus of maxima in S coincides with locus of maxima in isothermal compressibility for $P \gtrsim 0.5$ [179].

The size of the largest non-percolating cluster S^{\max} , shown in bottom panel of Fig. 4.8, is related to the fractal dimension D by the relation [131]

$$S^{\max} \sim N^{\frac{D}{d}} . \quad (4.14)$$

The estimate of D from power law fits of the data are consistent (even if smaller with respect the estimate from power law decay of n_s) with the hypothesis that clusters are more compact as the pressure is increased above P_C . Moreover the scaling analysis confirms the different behavior of S as $P \sim 0.6$ is crossed, consistently with the thermodynamic estimation of critical pressure.

At the critical pressure S diverge with a power law function

$$S \sim |T - T_C|^{-\gamma} \quad (4.15)$$

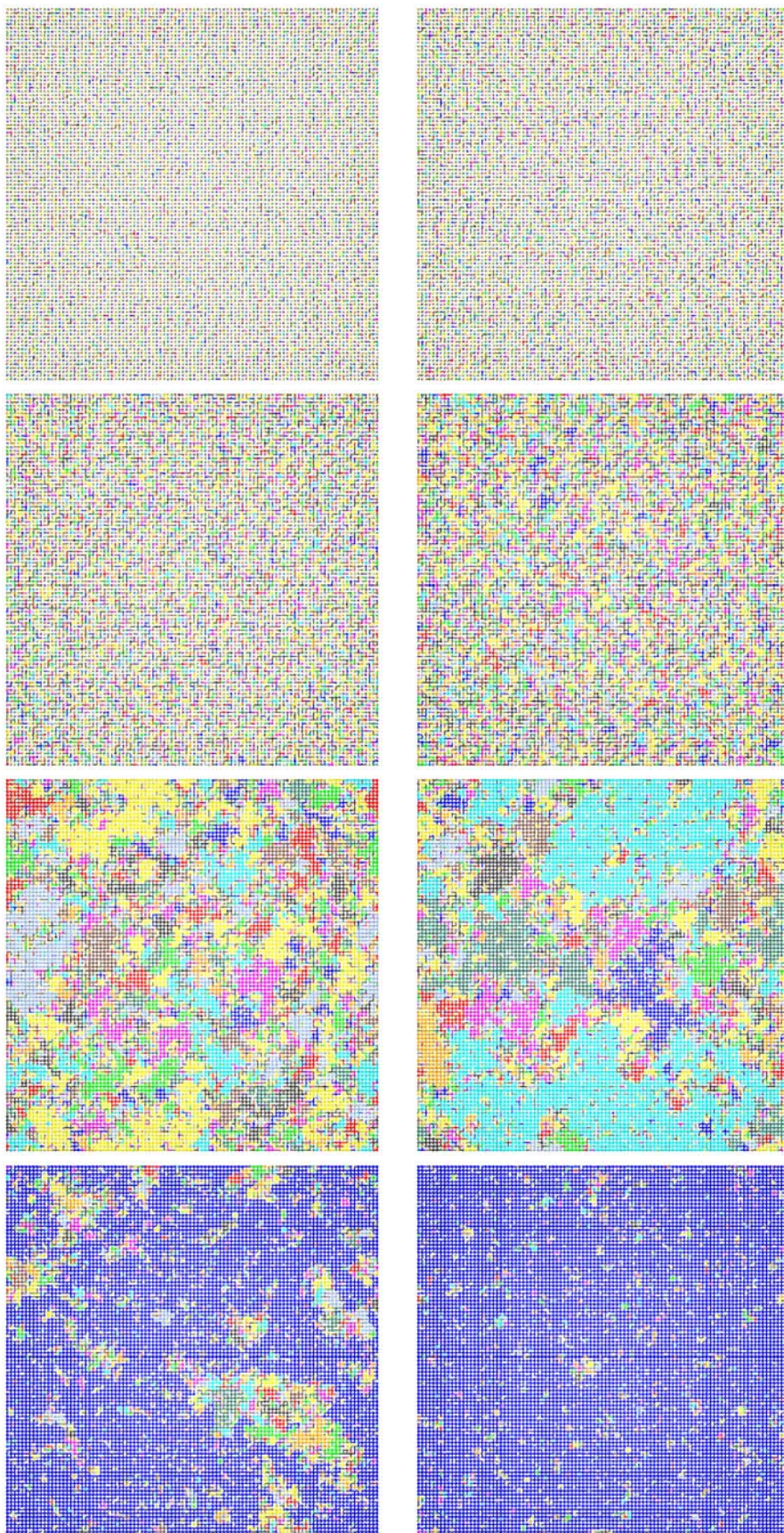


Figure 4.6: Cluster configurations for $N = 10000$ water molecules. Data are taken at $P = 0.6$ for (beginning at the top left): $T = 0.4$, $T = 0.2$, $T = 0.1$, $T = 0.07$, $T = 0.05636$, $T = 0.058354$ (percolation threshold), $T = 0.05834$ and $T = 0.057$.

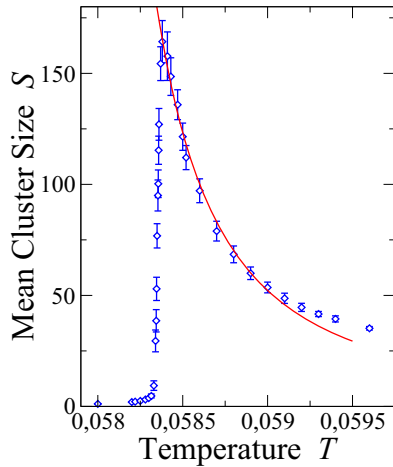


Figure 4.7: Mean cluster size for $P = 0.6$ and $N = 10000$ water molecules. Data are fitted with eq. (4.15) giving $\gamma \sim 1.7$.

where T_C is the critical temperature, where spanning cluster is observed. Estimation of $\gamma = 1.7 \pm 0.15$ is in good agreement with the value of 2D Ising universality class $\gamma = 7/4$, as shown in Fig. 4.7.

4.5 Connectivity length

The connectivity length ξ_C is the average distance between two σ variables belonging to the same non percolating cluster [131]

$$\xi_c^2 \equiv \sum_r P_{ij}(r)r_{ij}^2 \quad (4.16)$$

where P_{ij} is the probability that two molecules i and j , at distance r_{ij} belong to the same cluster. The sum extends over all cells i and j whose distance satisfies $r_{ij} < L/2$. We consider that the distance between variables σ of two molecules is constant. ξ_C sharply increase at the percolating threshold and the maximum value ξ_C^{max} is constant, inside the error bar, along the percolation line. Following the CK approach described in Sec. 4.1, it is possible to show that ξ_C coincides with the statistical correlation length ξ , calculated as

$$\xi^2 \equiv \sum_r G(r)r^2 / \sum_r G(r) \quad (4.17)$$

where

$$G(r) \equiv \frac{1}{N} \sum_{|i-j|=r} \frac{\langle \sigma_i \sigma_j \rangle - \langle \sigma_i \rangle^2}{\langle \sigma_i^2 \rangle - \langle \sigma_i \rangle^2} \quad (4.18)$$

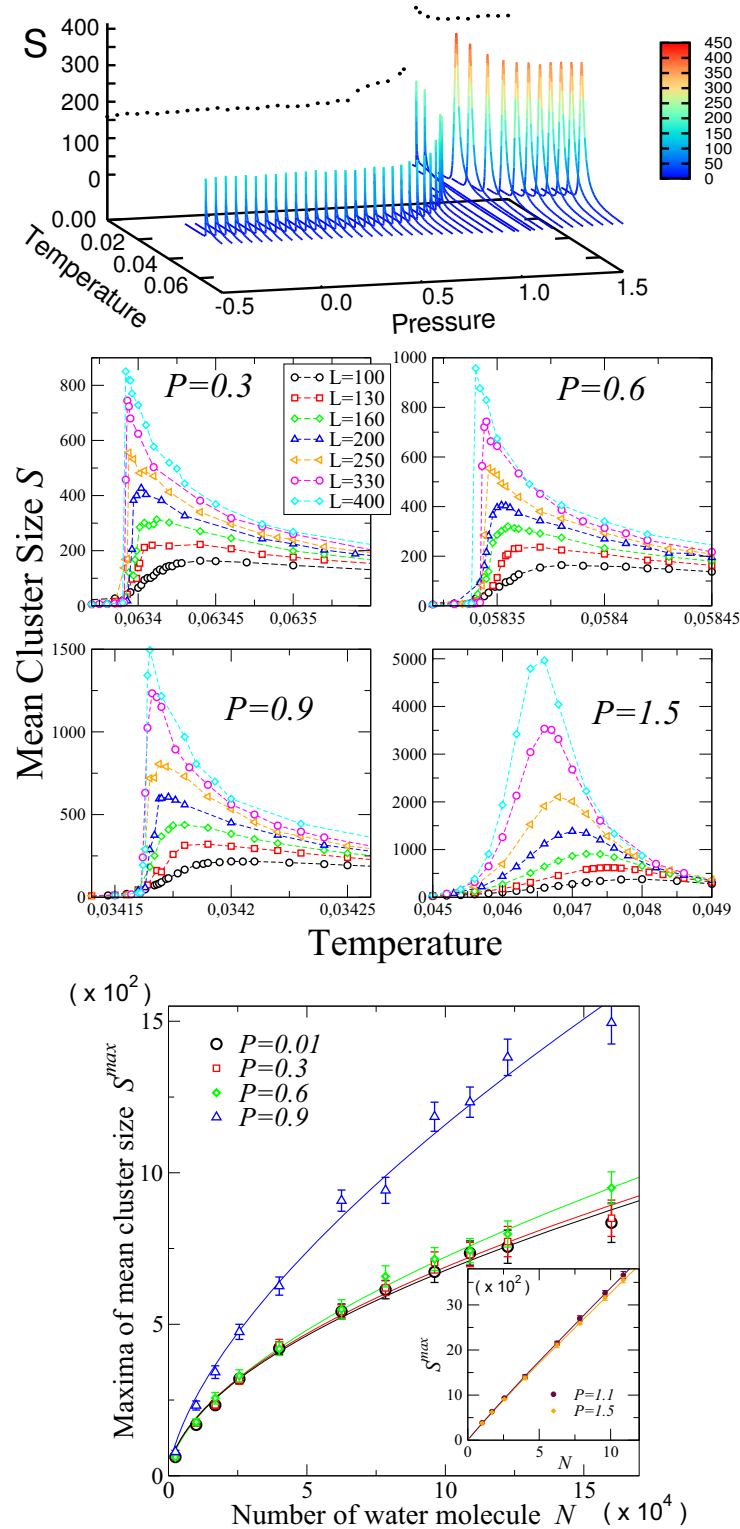


Figure 4.8: **Top panel:** isobaric mean cluster size S as function of temperature for $N = 10^4$ water molecules. The color code along the lines represents the value of S . Black points are the projection of the maxima. **Central panels:** S for different system sizes L and pressures across the percolating transition. Note as the behavior of S for $P = 1.5$ differs completely with respect the ones for $P < 1$. **Bottom panel:** scaling of maxima in S . Lines are power law fits with relation (4.14). We find values of D ranging from $D = 1.15 \pm 0.2$ for $P = 0.01$, to $D = 1.35 \pm 0.20$ for $P = 0.9$. For higher P we have $D = 1.9 \pm 0.1$ consistent with compact clusters.

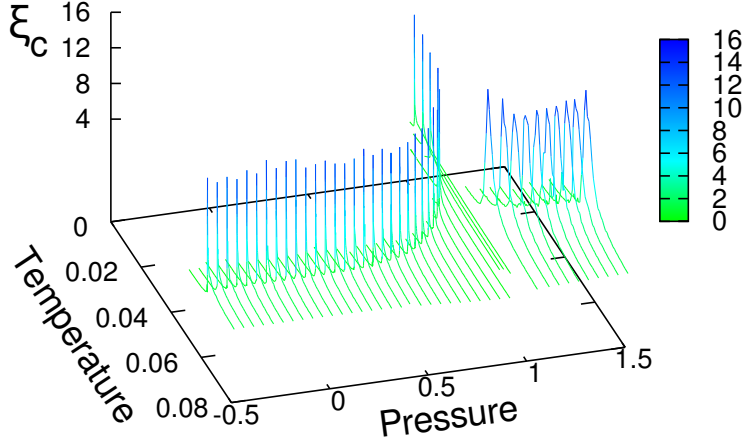


Figure 4.9: Connectivity length ξ_C along isobars for $N = 13225$ water molecules. Values of ξ_C are expressed in cell size unit. Color code represents the value of ξ_C along curve.

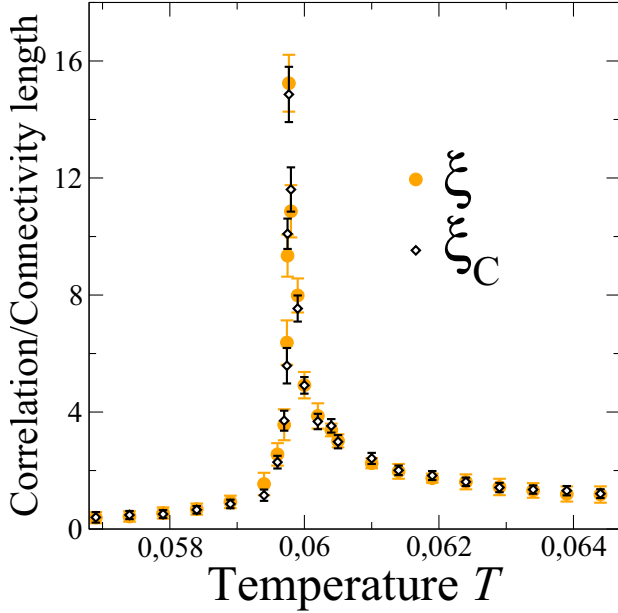


Figure 4.10: Comparison between correlation length ξ and connectivity length ξ_C along the critical isobar ($P = 0.6$) for $N = 13225$ water molecules.

is the correlation function of the σ variables. The loci of maxima of both quantities coincide. Around the critical pressure we find $\xi \sim \xi_C$ for all T , as shown in figure 4.10. At a distance of $\sim 30\%$ away from the critical region ($P \lesssim 0.4$ and $P \gtrsim 0.75$) we find that ξ^{max} is $\sim 30\%$ smaller than ξ_C^{max} , outside the numerical error bar (Fig. 4.11). Moreover at low pressure, maxima in ξ_C are independent on the formation of HB network.

4.6 Scaling analysis

By definition of critical exponents β and γ , at the percolation threshold the following relations hold for P_∞ and S

$$P_\infty \sim |p - p_c|^\beta \quad (4.19)$$

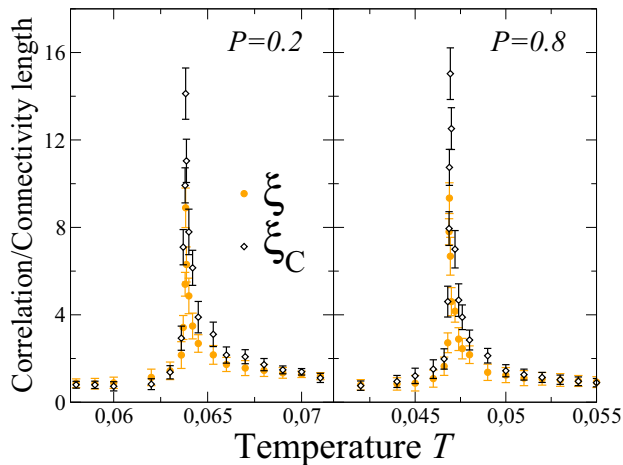


Figure 4.11: Comparison between correlation length ξ and connectivity length ξ_C for $N = 13225$ water molecules away from the critical region, across the Widom line ($P = 0.2$) and the LL-phase transition ($P = 0.8$).

$$S \sim |p - p_c|^{-\gamma} \quad (4.20)$$

where p_c is the critical probability. In our site-bond percolation description we introduce two probabilities, p_J and p_{J_σ} . Around the critical region it is $p_{J_\sigma} < p_J$, hence we adopt p_{J_σ} as relevant field. Moreover p_{J_σ} is associated to the cooperative component of the HB, responsible of spreading of fluctuations along the HB network.

The ansatz for finite size scaling of S and P_∞ in the NPT ensemble are [141, 181]

$$S \sim f_S(|e^{-J_\sigma/T} - e^{-J_\sigma/T_C(N)}|N^{1/d\nu})N^{\gamma/d\nu} \quad (4.21)$$

$$P_\infty \sim f_P(|e^{-J_\sigma/T} - e^{-J_\sigma/T_C(N)}|N^{1/d\nu})N^{-\beta/d\nu} \quad (4.22)$$

where f_S and f_P are universal size-independent functions. Via data collapse we estimate the size-dependent values of the percolation temperature $T_C(N)$ and of the critical exponents β , ν and γ . In figures 4.12 and 4.13 we show the scaling of data respectively at the critical pressure, and for $P = 1.5$ along the Kertész line. Values of critical exponents at the critical point are consistent with the Ising universality class in two dimensions, while along the Kertész line for $P > 1$ they coincides with site percolation exponents [131]. Along the Widom line we find that scaling relation are satisfied, although with smaller values of exponents ν and γ with respect the $2d$ -Ising ones (data not shown). We interpret this deviation as due to the fact that along the Widom line, away from the critical point, the system does not undergoes any phase transition, hence the critical exponent description is no longer valid.

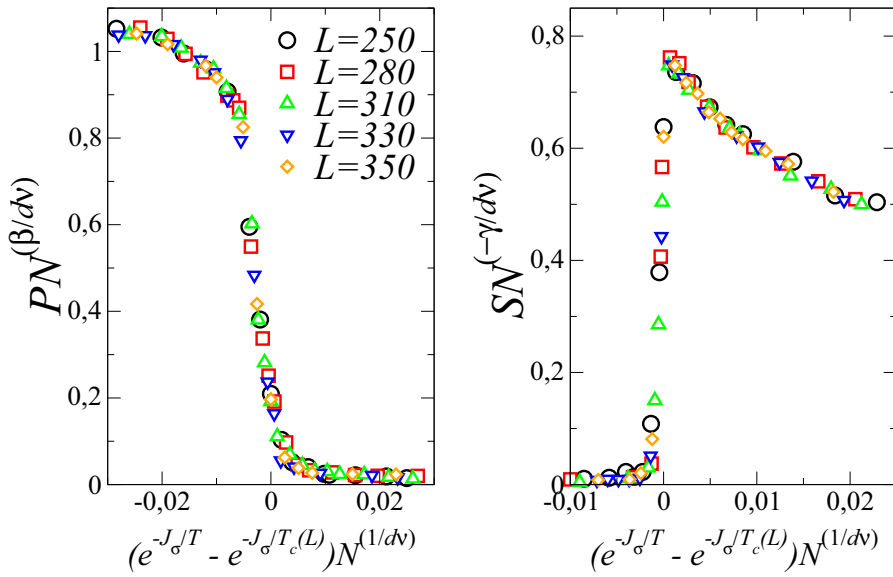


Figure 4.12: Scaling of percolation probability P_∞ and mean cluster size S at the critical point. We estimate $\nu \sim 1.11 \pm 0.15$, $\gamma \sim 1.5 \pm 0.2$ and $\beta = 0.15 \pm 0.05$. Those values are in good agreement with the 2D Ising critical exponents, $\nu = 1$, $\gamma = 7/4$ and $\beta = 1/8$.

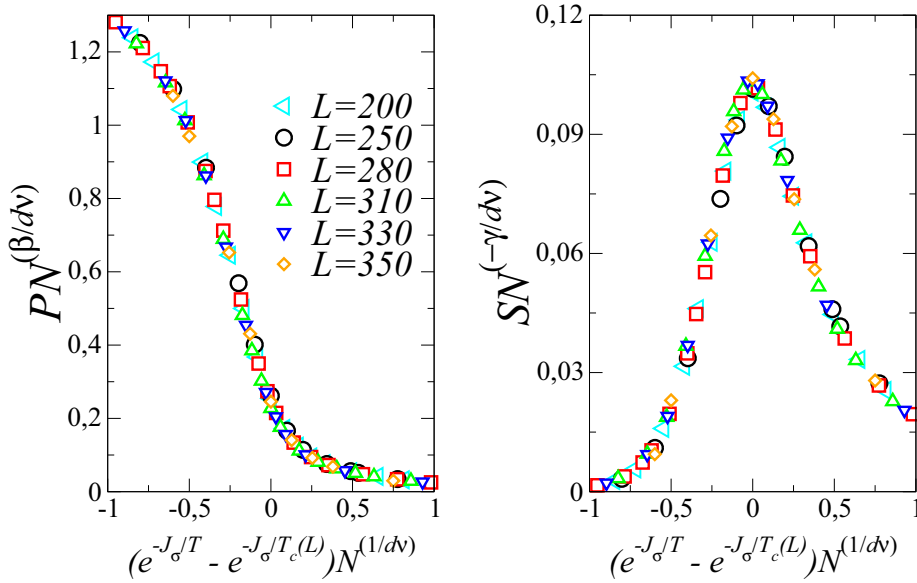


Figure 4.13: Scaling of S and P_∞ for $P = 1.5$. We estimate $\nu \sim 1.33 \pm 0.10$, $\gamma \sim 2.39 \pm 0.11$, $\beta \sim 0.14 \pm 0.04$. These values coincide with the ones of the site percolation universality class, $\nu = 4/3$, $\gamma = 43/18$ and $\beta = 5/36$.

Chapter 5

Role of interfacial HBs on protein stability

The mechanisms of cold- and pressure-denaturation of proteins are matter of debate but it is commonly accepted that water plays a fundamental role in the process. It has been proposed that the denaturation process is related to an increase of hydrogen bonds among hydration water molecules. Other theories suggest that the cause of denaturation are the density fluctuations of surface water, or the destabilization of hydrophobic contacts as a consequence of water molecules inclusions inside the protein, especially at high pressures. In this chapter we review some theories that have been proposed to give insight into this problem, and extend the water cell model for a homopolymer in contact with the water mono-layer in the attempt to understand how the interplay of water cooperativity and interfacial hydrogen bonds affects the protein stability.

5.1 Overview on protein stability

One of the most intriguing challenge in biological physics is the nature of protein folding-unfolding processes. The temperature range of stability of a folded protein is in general small. For example, staphylococcal nuclease (Snase—a small protein containing 149 amino-acids) folds at low pressure approximately between 260 K and 320 K [182].

Heat destabilizes proteins. By increasing the bath temperature T , thermal fluctuations increase and disrupt the folded configurations of proteins. By decreasing T , proteins can crystallize, but surprisingly some proteins unfold at sufficient low temperature instead of crystallizing [182–188]. Cold denaturation seems to be a general phenomenon for proteins, generally occurring well below 0°C, the freezing point of water. In some cases, for example for Snase [182], the cold denaturation cannot be directly observed, but experimental data can be extrapolated to predicted the lower temperature of protein stability. In general,

destabilizing agents can be used to make the cold denaturation observable. Interestingly, Pastore et al. [188] observed that Yeast frataxin under physiological conditions undergoes cold denaturation below 7°C and remains folded up to 30°C. Hence, Yeast frataxin is an excellent prototype for studying folding transition under accessible conditions for both hot- and cold-unfolding. The study could help in understanding the mechanism of cold-unfolding that, as we will discuss in the next sections, is still matter of debate.

Proteins can unfold also by pressurization. It has been observed that the increase of pressure induces the unfolding of protein [189–191]. The pressure-unfolding process can be rationalized by considering that the folded structure usually includes cavities. High pressure can induce elastic response of the protein, deforming its structure and pushing water molecules inside the cavities. The water molecules from inside would swell the protein, with consequent loss of protein functionality [190]. Because it is difficult to separate the protein response to high hydrostatic pressure from the response of the aqueous environment, the understanding of the pressure-unfolding is still under debate.

5.1.1 Thermodynamics of proteins unfolding

By increasing the thermal energy $k_B T$ (k_B is the Boltzmann constant), the protein residues vibrate faster, accessing new possible configurations, i. e. increasing the entropy S of the system. This increase leads to hot denaturation, in the same way an increase of $k_B T$ leads to the melting of a crystal, at expenses of the energy of the system, compensated by an increase of entropy.

The cold denaturation, instead, cannot be explained as the effect of an increase of entropy. By decreasing T , the entropy of the system decreases. Hence, in the case of proteins there must be a complex mechanism that induces the cold denaturation.

General principles of thermodynamics tell us that at any value of T and P the system minimizes its Gibbs free energy, $G \equiv H - TS$, where $H \equiv U + PV$ is the enthalpy of the system, U the internal energy of the system, V the volume and P the pressure. In our case the system is the solution of proteins and water. Hence, the free energy balance must take into account both water molecules and protein residues. The experimental fact that solvated proteins unfolds by decreasing T means that at lower T the difference

$$\Delta G \equiv G_u - G_f \tag{5.1}$$

between the unfolded (u) and folded (f) states is

$$\Delta G = \Delta H - T\Delta S < 0, \quad (5.2)$$

where $\Delta H \equiv H_u - H_f$ and $\Delta S \equiv S_u - S_f$.

The total variation of the entropy of the system is given by $\Delta S = \Delta S_p + \Delta S_w$ where ΔS_p and ΔS_w are the entropy variation of protein residues and water molecules, respectively. By unfolding, the protein entropy increases, $\Delta S_p > 0$. On the other hand, the protein contribution to ΔH is positive, $\Delta H_p > 0$, because the enthalpy of the protein increases when the protein unfolds (H_p decreases when the number of contact points of the protein increases). Therefore, the protein contribution to ΔG does not guarantee that Eq. (5.2) is satisfied, because $\Delta H_p - T\Delta S_p$, could be negative or positive depending on the relative variations at the given T . Hence, water contribution to the total balance of Eq. (5.2) could be relevant. A commonly proposed idea is that the native-folded state is stabilized by the quasi-ordered network of water molecules hydrating the non-polar monomers [192–195].

5.1.2 Protein phase diagram

In this section we summarize the main theoretical calculations, due to Hawley [196] and reviewed by Smeller et al. [197] and Meersman et al. [198], predicting a close stability region (SR) in $P - T$ plane for proteins, consistent with experiments (Fig. 5.1) [182, 183, 185, 186, 188, 199]. Outside the elliptic region the protein unfolds, losing its biological function¹.

Following Hawley [196, 197], we can calculate ΔG of the whole system (protein and water) assuming that a protein can stay in only two distinct states, folded and unfolded as in eq. 5.1. Differentiating G , we get

$$dG = -SdT + VdP \equiv dG(T, P). \quad (5.3)$$

Hence, it is

$$d\Delta G = -\Delta SdT + \Delta VdP \quad (5.4)$$

with $\Delta V \equiv V_u - V_f$. By expanding ΔS and ΔV to the first order around ΔS_0 and ΔV_0 ,

¹Actually there are a few classes of materials which are characterized by elliptically shaped phase diagrams. For instance, in some liquid crystalline materials the phase boundary between the nematic to smectic-A transition falls into this category [200].

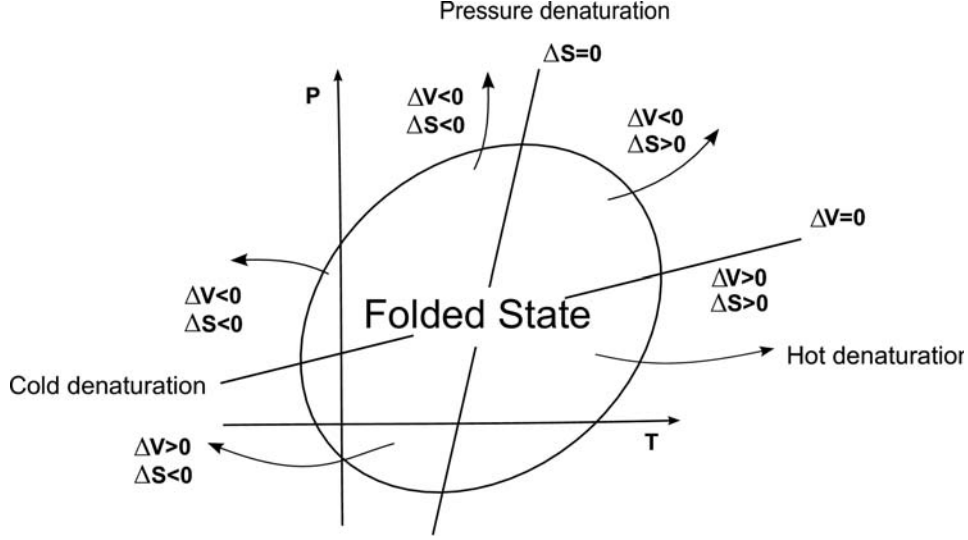


Figure 5.1: Schematic representation of the phase diagram of a protein. Within the elliptic region the protein is folded, while it unfolds by increasing temperature T (hot denaturation), by decreasing T (cold denaturation), by increasing or decreasing pressure P (pressure denaturation). Each folding–unfolding process is characterized by different variation of entropy ΔS and variation of volume ΔV as indicated in the figure. The axes of the ellipse are loci where $\Delta S = 0$ and $\Delta V = 0$ (see text for discussion). Adapted from [190].

we get

$$\Delta S = \Delta S_0 + \left(\frac{\partial \Delta S_0}{\partial T} \right)_P (T - T_0) + \left(\frac{\partial \Delta S_0}{\partial P} \right)_T (P - P_0) \quad (5.5)$$

$$\Delta V = \Delta V_0 + \left(\frac{\partial \Delta V_0}{\partial T} \right)_P (T - T_0) + \left(\frac{\partial \Delta V_0}{\partial P} \right)_T (P - P_0) \quad (5.6)$$

and from Eq. (5.4)–(5.6), by integration,

$$\Delta G(P, T) = \frac{\Delta \beta}{2} (P - P_0)^2 + 2\Delta \alpha (P - P_0)(T - T_0) + \quad (5.7)$$

$$-\Delta C_P [(T - T_0) - T_0 \ln(T/T_0)] + \Delta V_0 (P - P_0) - \Delta S_0 (T - T_0) + \Delta G_0$$

where $\alpha \equiv (\partial V / \partial T)_P = -(\partial S / \partial P)_T$ is the thermal expansivity factor, related to the isobaric thermal expansion coefficient α_P by $\alpha_P = \alpha / V$; $C_P \equiv T(\partial S / \partial T)_P$ is the isobaric heat capacity and $\beta \equiv (\partial V / \partial P)_T$ is the isothermal compressibility factor related to the isothermal compressibility K_T by the relation $K_T = -(\beta / V)$. All the quantities with the subscript equal to zero are usually referred to ambient conditions. By developing the

logarithm to the second order around (T_0, P_0)

$$\ln\left(\frac{T}{T_0}\right) \sim \frac{T - T_0}{T_0} - \frac{(T - T_0)^2}{2T_0^2} \quad (5.8)$$

we get

$$\begin{aligned} \Delta G(P, T) = & \frac{\Delta\beta}{2}(P - P_0)^2 + 2\Delta\alpha(P - P_0)(T - T_0) + \\ & - \frac{\Delta C_P}{2T_0}(T - T_0)^2 + \Delta V_0(P - P_0) - \Delta S_0(T - T_0) + \Delta G_0 . \end{aligned} \quad (5.9)$$

Hence, assuming that the $u \rightarrow f$ is a first order phase transition, along the coexistence line it holds the Clapeyron equation $dP/dT = \Delta S/\Delta V$ and $d\Delta G = 0$, for which the coexistence line is given by

$$\begin{aligned} & \frac{\Delta\beta}{2}(P - P_0)^2 + 2\Delta\alpha(P - P_0)(T - T_0) + \\ & - \frac{\Delta C_P}{2T_0}(T - T_0)^2 + \Delta V_0(P - P_0) - \Delta S_0(T - T_0) + \Delta G_0 = 0 \end{aligned} \quad (5.10)$$

that is the equation of an ellipse, as in Fig. (5.1), given the constraint

$$\Delta\alpha^2 > \Delta C_P \Delta\beta / T_0 . \quad (5.11)$$

This condition is guaranteed by the different sign of ΔC_P and $\Delta\beta$, as can be observed for some proteins, as reported by Hawley [196].

The eq. 5.10 is the Taylor expansion of $\Delta G(P, T)$ arrested to the second order, holding for $\Delta\alpha$, $\Delta\beta$ and ΔC_P independent of T and P . These assumptions are generally valid and adding third order terms in the expansion has minimal effects on the elliptic shape of the SR.

At maximum pressure P_{\max} of stability for the protein, $d\Delta G/dT = \Delta S = 0$, while at the maximum temperature T_{\max} of stability, $d\Delta G/dP = \Delta V = 0$. Therefore, based on Hawley's theory it is possible to make general predictions about the changes of ΔV and ΔS as schematically summarized in Fig. 5.1. This phenomenological theory does not take into account the explicit informations about the protein structure, and makes strong assumptions, such as, for example, that the protein only has two states, or that equilibrium thermodynamics holds during the denaturation. The last assumption, in particular, im-

plies that the whole process would be reversible. Nevertheless, consistency with Hawley's theory is a good test for models of protein unfolding. More details about the arguments summarized here can be found in Ref. [198].

In the next section we review some of these models. The review does not pretend to be exhaustive, but it has the aim of mentioning a number of positive results of the theories formulated to understand protein folding.

5.2 Models for protein unfolding

5.2.1 Hydrophobic effect

To date is widely shared the idea that hydrophobic interactions play an important role in protein folding. A solute is considered hydrophobic if it binds to water in weaker way than water itself.

A model for protein folding taking into account implicitly the hydrophobic effect was proposed in 1989 by Lau and Dill, known as HP model [201]. By assuming that the exposed surface of hydrophobic residues is energetically unfavorable at low T , the model reproduces the folding of the protein (hydrophobic collapse). The protein is represented as a self-avoiding chain on a lattice. The chain is composed by two different categories of amino acids: H (hydrophobic non-polar) and P (polar). The presence of the aqueous environment is taken into account introducing an attractive contact interaction between H monomers. This interaction captures the hydrophobic effect between water molecules and non polar amino acids. No other interactions are present in the system.

Under these hypothesis, the authors show that the features of the folding process depend on the HH energy interaction, the length of the chain, and the specific sequence of H and P monomers. Moreover, for long chains one folded state dominates.

The model has the virtue to reduce the complexity of the folding process to a manageable level. All the electrostatic and chemical properties of each amino-acid are simplified by allowing only two possible states. The degrees of freedom of the solvent are not explicitly included. Nevertheless, the HP model cannot describe cold denaturation. Therefore, the experimental evidence of cold denatured proteins calls for a reconsideration of the hydrophobic interaction and its dependence on temperature and structure of hydration water [184–187].

Back in 1945, Frank and Evans [192] discussed the tendency of water to form ordered structures around non-polar solutes to minimize the free energy cost of solvation. As a

consequence, hydrophobic solutes are “structure makers” for water, facilitating the formation of cages around the solute. The effect of these structures around hydrophobic solutes is to reduce the entropy with respect to the bulk and to compensate, approximately, the enthalpy cost for the creation of a cavity to allocate the solute.

As discussed by Muller in 1990 [194], the compensation of the enthalpy implies that water-water hydrogen bonds (HBs) at the interface with the hydrophobic solute are stronger than those in the bulk. This is consistent with the experimental observation that the excess molar heat capacity for a non-polar solute at infinite dilution in water is positive. This quantity, defined as the difference of the partial molar heat capacity in solution with respect to the heat capacity of the pure liquid solute, is far larger at 25 °C when the solvent is water than for any other solvent [194, 202].

The statement that HBs are stronger at the hydrophobic interface has led to the misconception that water around a hydrophobic solute has an iceberg-like structure. Computer simulations [203, 204], theoretical analysis [205, 206], and neutron scattering studies [207] are inconsistent with iceberg-like structures. Hence, the restructuring of water around a solvent seems not to play a relevant role in the hydrophobic effect. Nevertheless, Muller [194] shown that if hydration HBs are enthalpically stronger but fewer than in bulk, a model with two-states HBs can reproduce the sign reversal of the proton NMR chemical shift with T and the heat capacity change upon hydration.

On the other hand, a common opinion [208] is that the large free-energy change associated to the hydrophobic effect is due to the small size of the water molecules with respect to the solutes, and that the free-energy change associated to the network reorganization around hydrophobic particles is negligible due to compensation of enthalpy and entropy, although it may account for the large heat capacity change upon hydration. This observation apparently ruled out Muller model, where the enthalpy-entropy compensation upon hydration was not present.

Nevertheless, Lee and Graziano in 1996 [209] shown that Muller model can be slightly modified to recover also the enthalpy-entropy compensation upon hydration. The Muller-Lee-Graziano model was further simplified by De los Rios and Caldarelli in 2000 [210, 211] in order to reduce the number of parameters. Simplifying the description of bulk water, they recovered hot and cold denaturation for a protein represented as a hydrophobic homopolymer. A development of this model has been used in 2005 to study the effective interaction between chaotropic agents and proteins [212].

The model of De los Rios and Caldarelli has been generalized by Bruscolini and Casetti

[213,214] in 2001 by allowing each monomer of non-polar homopolymer to be in contact with a cluster of water molecules. Each cluster has an infinite number of possible states and only one state minimizes the free-energy cost of the interaction with the hydrophobic monomers. The model reproduces the trends of thermodynamic averages in accordance with experiments [215] and simulations [195], and predicts the hot and cold denaturation. These results are qualitatively similar to those of the Muller-Lee-Graziano model, further supporting the relevant role of the solvent in the folding-unfolding process.

Cold denaturation and T -dependence of the hydrophobic effect were also observed by Dias et al. in 2008 analyzing a non-polar homopolymer in the Mercedes-Benz (MB) model for water [216]. The MB model, originally introduced by Ben-Naim [217] 1971, represents water molecules as disks in two-dimensions with three possible HBs (arms) as in a Mercedes-Benz logo. Water molecules interact via van der Waals potential and HB interactions. HB interaction is modeled with a Gaussian potential, favoring a fixed value for the water-water distance and aligned arms for facing molecules. Simulations show that the average HB energy is higher for shell water than for bulk water at high T , while is lower at lower T . Therefore, by cooling the solution, is energetically more convenient to increase the protein surface exposed to water, inducing protein unfolding. In this model, the water molecules forming a cage around the protein monomers are strongly H-bonded to each other. The highly ordered structure of the solvent around the monomers decreases the entropy of water, compensating the increase of the entropy associated to the protein unfolding.

This model has been criticized [218] because it assumes, without proof, that the enthalpy gain dominates at low T , giving rise to free-energy gain upon unfolding of the protein. In particular, Yoshidome and Kinoshita in 2009 [218] analyzed by integral equation theory the behavior of a non-polar homopolymer composed by fused hard-spheres of different diameters immersed in smaller hard spheres, with permanent electrostatic multiple moments, representing the solvent [219]. The protein-water interaction is represented by a hard sphere potential and water-water interaction by a hard sphere potential and an electrostatic contribution given by the electrostatic multipole expansion. The author found that denaturation is characterized by large entropy loss and large enthalpy gain. However, these two contributions to the free energy almost completely cancel out and make no significant contribution to the free-energy change. They found that the driving mechanism for cold denaturation is the translational entropic-loss of water due to the large excluded volume of the hydrophobic particles. They observed that at low T water diffuses less, therefore the hydrophobic effect is weaker and the protein unfolds.

In a recent work [220], Matisyak and coworkers present a three-dimensional lattice model for an hydrophobic homopolymer in explicit water. They observe that the T -folding process is due by either attractive interactions between the monomers or by modeling the entropic cost of forming interfacial hydrogen bonds. In particular, cold denaturation is only observed when the enthalpic benefit of forming additional interfacial water molecules overcomes the enthalpic benefit of forming monomermonomer interactions.

A different approach to the role of hydrophobic interaction in polymer collapse and nanoparticles self-assembly is represented by the theory proposed Lum, Chandler and Weeks in 1999 [221], further developed by ten Wolde and Chandler in 2002 [222] and recently by Varilly, Patel and Chandler in 2011 [223]. They start from the observation that, at ambient conditions, the solvation free energy of hard sphere solutes increases: a) with the solute volume for solutes of small radius; b) with the solute surface for solute of large radius.

Hence, the solvation free energy exhibits a crossover between two regimes: for small solute the entropy leads to the dispersion of hydrophobic particles, while for large solute the enthalpy drives to hydrophobic collapse of the particles. The authors associate the enthalpy change responsible for the hydrophobic collapse to dewetting transition, i.e. to a microscopic liquid-gas phase separation of water molecules at the interface with the solute. Therefore, the average number of water molecules in a probe volume close to the solute decreases respect to bulk and a liquid-gas interface is formed near the hydrophobic particles, i.e. the solute is surrounded by vapor bubble. In order to reduce the free energy cost to form a liquid-gas interface, the solutes collapse. To take into account the crossover at different length-scale, the authors propose a mean field model for the water solvent. Water density is modeled as a sum of two scalar field, representing the large and the small length-scale contribution to water density. This decomposition is valid in thermodynamic conditions far away from critical regions of water, where density fluctuations are expected to be strong. The Hamiltonian for the water system is a bilinear form, coupling the two components of the density field. The solute-water coupling is represented by an excluded volume term or by an external tuning potential. The hydrophobic collapse of a polymer [222] and the dewetting transition of confined water [223] are studied at ambient conditions with interesting predictions. In particular, the tendency of vapor formation at the solute interface decreases as the system is moved away from liquid-vapor equilibrium, i.e. by lowering the temperature or increasing the pressure. Therefore, the authors offer a rationale for protein unfolding at low T and high P , as a consequence of destabilization of the

hydrophobic collapse.

5.2.2 Pressure effects

Pressure effects have been also considered in microscopic theoretical models for protein denaturation. For example, in 2003 Marqués and coworkers [224] considered a model in two dimensions with a hydrophobic homopolymer, represented as a self-avoiding random walk, embedded in water at constant P . They adopted the Sastry et al. water model [41] for water–water interactions. They considered that polymer–water interaction is repulsive, hypothesizing that is proportional to the density number of HBs and to the number of missed native contact points among monomers of the protein. The model displays hot denaturation, cold denaturation and denaturation at high pressure, in agreement with stability diagram of some proteins [225]. A peculiarity of this model is that the effective repulsion between protein and solvent is mean field because it depends on the average number of HBs of bulk water, that is an average property of the bulk.

To remove this coupling in 2007 Patel and coworkers [226] proposed a model where water at the interface with protein has a restricted number of accessible orientations for the HBs compared to the bulk. Along with this entropic reduction, the interfacial HBs also have an additional enthalpic bonus with respect to bulk water, following the ideas discussed by Muller, Lee and Graziano. The model displays a stability phase diagram with hot, cold and pressure denaturation. However, it does not reproduce all the expected features of the schematic phase diagram of Fig. (5.1). In particular, the model does not reproduce the elliptic shape of the phase diagram and the low- P region with $\Delta V > 0$ for hot denaturation. These results were confirmed by extending the model to the case with heteropolymers.

5.3 Coarse-graining the water-water interaction at protein interface

Following our discussion about how could be relevant to take into account the HB free energy to explain the lost of stability of folded proteins, we test if the proposed water model could give insight into the mechanism of unfolding.

To this goal we modify the water model to introduce the effect of the protein-water interface. For sake of the simplicity, we will limit our discussion to the case of a single protein embedded into a water mono-layer. Although this case is far from the complex

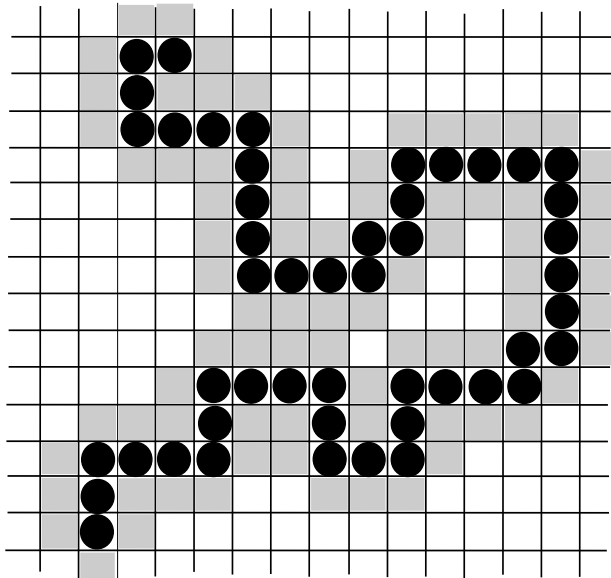


Figure 5.2: Example of configuration of a homopolymer in the coarse-grained model of a protein suspended in water. Each cell is occupied either by a water molecule (white and gray cells) or a hydrophobic homopolymer monomer (cells with a full black circle). The gray cells represents the sites occupied by shell water. The enthalpy gain for HB formation between shell water molecules is larger than that between bulk water molecules, according to the Eq. (5.13). Shell water molecules cannot form hydrogen bonds with nearest neighbor hydrophobic monomers.

studies of a protein embedded into bulk water, the model gives instructive results.

The water Hamiltonian is

$$\mathcal{H} = U(r) - JN_{\text{HB}} - J_{\sigma}N_{\text{coop}} \quad (5.12)$$

Data reproducing elliptic shape of protein SR are usually taken in solution, where a consistent percentage of ions are present. It is known that the structure of water HB network is perturbed by the presence of ions, but a common interpretation on the “structure-maker” or “structure-breaker” role played by ions is still lacking. Some works state that ions lead to a decrease of the average number of HB in the first and second hydration shells [227–230], with small effects observed even in the bulk. Nevertheless, in this conditions the LLCPC is expected to shift at higher T and lower P [231]. According to ref. [49], in our cell model this effect is observed when the ratio J/J_{σ} decreases. We account for this fixing $J/4\epsilon = 0.3$.

The simplest protein that we can consider is a hydrophobic homopolymer, schematized as a self avoiding chain (Fig. 5.2), which monomers occupy nearest-neighbor sites. Each element of the polymer occupies an entire cell without affecting its volume. The protein has no self-interaction aside from excluded volume effects. The polymer interaction with water is through its indirect effect on water-water hydrogen-bonding.

Following the discussion of Muller [194], we require that, consistent with experiment, water molecules in contact with a hydrophobic monomer have larger decrease of enthalpy upon HB formation than bulk water. Also consistent with Muller-Lee-Graziano discussion

[209], the fraction of broken HBs at the hydrophobic interface is larger than the fraction of broken HBs in the bulk.

The first requirement is achieved by adding a term to the water Hamiltonian Eq. (5.12)

$$\mathcal{H}_{\text{surf}} = -\lambda J \sum_{\langle ij \rangle_{\text{surf}}} n_i n_j \delta_{\sigma_{ij}} \delta_{\sigma_{ji}}, \quad (5.13)$$

where the sum is taken over nearest neighbor water molecules in the protein hydration shell (Fig. 5.2), and $\lambda > 0$ is an adjustable parameter accounting for the larger enthalpy decrease for HBs in the hydration shell. Hence, for a HB formed between water molecules in the shell, the energy variation is

$$J_{\text{surf}} \equiv -J(1 + \lambda). \quad (5.14)$$

The presence of the hydrophilic interface entails a decrease of hydration water density [91, 221, 232, 233], a phenomenon that can be interpreted as a dewetting transition, with consequent formation of vapor-like bubbles at the interface. It has been observed that increasing P suppresses formation of such bubbles by reducing water fluctuations in the hydration shell, making the hydration shells of unfolded proteins more compressible than the folded ones [191, 234–237] and shortening the most protein-water HBs [238]. Indicating with v_{surf} the volume increase due to interfacial water-water HB, we incorporate the denser hydration shell upon pressurization with

$$v_{\text{surf}} \equiv \tilde{v} - kP \quad (5.15)$$

where \tilde{v} and k are two adjustable parameters. As initial guess we fix $\tilde{v} = v_{\text{HB}}$ and $k = 0.5$. Hence the enthalpy variation in the hydration shell is $-J_{\text{surf}} + v_{\text{surf}}P$.

The second requirement of Muller-Lee-Graziano approach, i.e. a larger number of broken HBs at the interface, is achieved by volume exclusion. Once a cell of our system is occupied by a protein monomer, it cannot be occupied by a water molecule. Therefore, a water molecule, in the hydration shell cannot form the HB in the direction of the monomer and loses at least one HB (it can lose more if it has more monomers as nearest neighbors, as shown in Fig. 5.2).

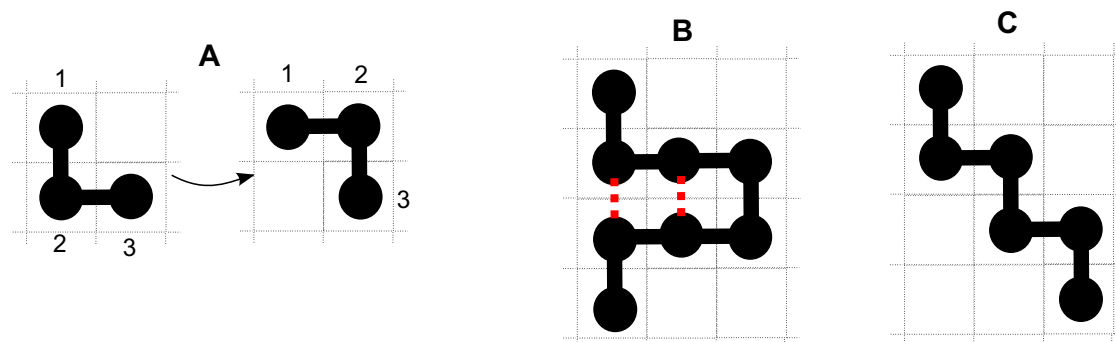


Figure 5.3: A) Monomer 2 is in a corner configuration and can be displaced from the configuration on the left to the configuration on the right and *vice versa*. B) Homopolymer configuration with two contact points, indicated with dotted lines. C) Homopolymer configuration without contact points.

5.3.1 Monte Carlo algorithm

We perform MC simulations in the NPT ensemble for a system size $L = 60$ and a polymer length $l = 30$. In every MC step we choose a cell at random. If it is occupied by a water molecule, we change randomly one of its σ variables. If it is occupied by a monomer and if the monomer is in a corner configuration (Fig. 5.3A) then we swap its position with the position of the water molecules in the cell in the opposite corner. By doing this, we keep the inter-monomer distances constant.

If the cell, picked at random, is occupied by a monomer not in a corner configuration, no displacement is performed because it would change the inter-monomer distance. This limitation is introduced in order to avoid in the enthalpy expression any term accounting for the elastic energy of the homopolymer. The effects of this elastic contribution are for the moment outside of the scope of the present work.

The phase space of a polymer is known to be complex and many local minima of free energy are present. When the free energy barrier is too high the polymer gets trapped. In these cases the exploration of new configurations is strongly inhibited because the system should pass through a series of statistically unlikely conformations before to run into new local minima. To avoid this hurdle, if the polymer configuration remains unchanged for a long series of Monte Carlo steps we allow it to jump directly in a new configuration through random moves of the monomers. Then the water is equilibrated blocking the polymer. The macro-move is accepted according to the global free energy change.

Finally, as in the cases discussed in the previous section, to keep the pressure of the system constant, every N random changes of the cell variables (where N is the total

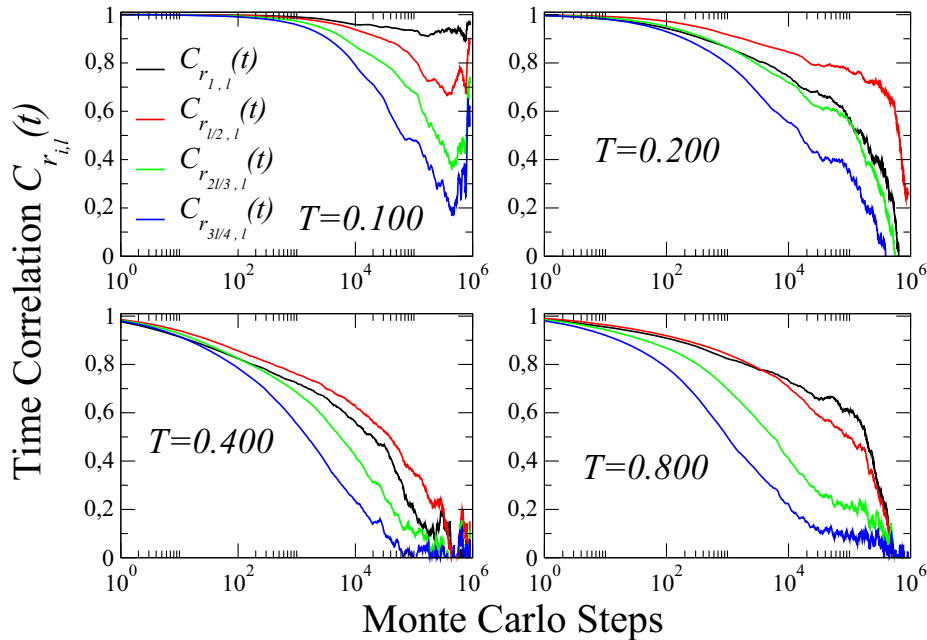


Figure 5.4: Time correlation of quantities $C_{r_{1,l}}(t)$, $C_{r_{\frac{1}{2},l}}(t)$, $C_{r_{\frac{2}{3},l}}(t)$ and $C_{r_{\frac{3}{4},l}}(t)$ for $P = 0.5$.

number of cells in the system), we attempt to rescale all the system volume by a factor that is tuned in a way to guaranty 50% of acceptance ratio. All the MC moves described above are accepted or rejected according to the Boltzmann factor associated to the enthalpy change caused by the move.

Simulations are carried out along isobars, adopting a folded state as initial polymer conformation and random values of variables σ . Each state point (T, P) is sampled with $\sim 10^3 \div 10^4$ independent configurations.

5.4 Phase diagram of a solvated homopolymer

To ensure the right exploration of phase space by the polymer, inside our simulation time, we calculate the time correlation of the cosine between unit vectors $\hat{r}_{i,l}$ joining the i^{th} and the final element of the polymer

$$C_{r_{i,l}}(\tau) \equiv \sum_t \hat{r}_{i,l}(t) \cdot \hat{r}_{i,l}(t + \tau) . \quad (5.16)$$

In particular we consider the vectors $\hat{r}_{1,l}$, $\hat{r}_{\frac{1}{2},l}$, $\hat{r}_{\frac{2}{3},l}$, $\hat{r}_{\frac{3}{4},l}$, where the end-to-end vector $\hat{r}_{1,l}$ is the mode of the polymer that relaxes slower [239]. Data for four T at fixed P are shown

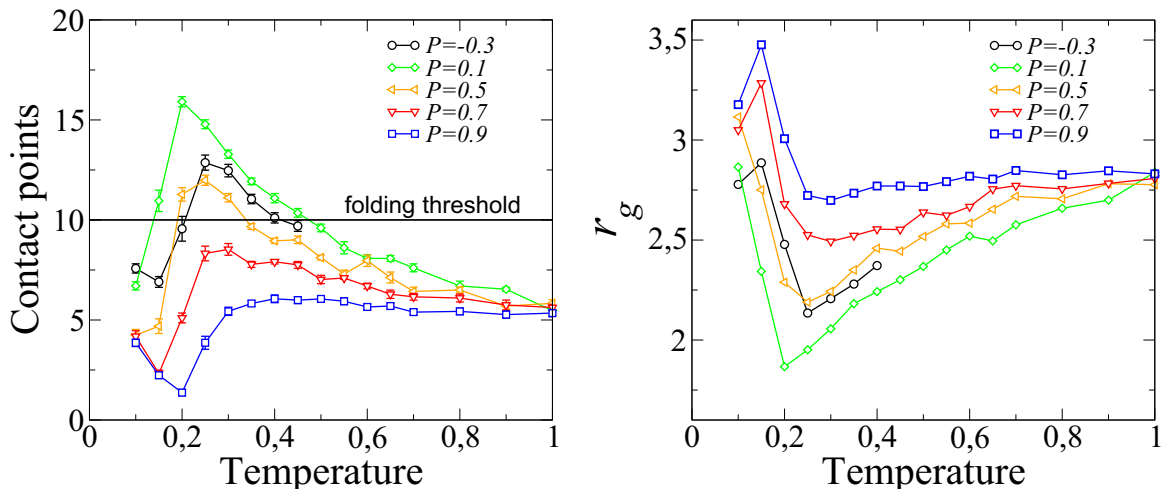


Figure 5.5: **Left panel:** Average number of contact points N_{cpts} as function of T for different pressures. **Right panel:** Average radius of gyration r_g . Error size are twice of symbol dimension.

in Fig. 5.4. For the lowest T the polymer does not relax.

In order to study the folding-unfolding process of the proteins we calculate the number of contact points N_{cpts} as illustrated in Fig. 5.3. In this calculation we do not count the monomers that are adjacent along the homopolymer. We define the folded configuration when $N_{\text{cpts}} \geq \frac{1}{2}N_{\text{cpts}}^{\text{max}}$, being $N_{\text{cpts}}^{\text{max}}$ the maximum number of contact points. In Fig. 5.5 we report N_{cpts} for different isobars. The temperature range, within which the polymer is folded, exhibits a non-monotonic behavior with P , with a maximum range for $P \sim 0.2$. Analogous behavior is observed in the radius of gyration r_g , (Fig. 5.5)

$$r_g^2 \equiv \frac{1}{2l^2} \sum_{i,j=1}^l |\vec{r}_i - \vec{r}_j|^2 \quad (5.17)$$

where \vec{r}_i is the position vector of the i^{th} monomer.

Fig. 5.6 shows the phase diagram with different level curves representing the folded percentages for $J_{\text{surf}} = 0.55$. The native configuration stays inside the 50% curve. The model protein exhibits heat-, cold-, and pressure-unfolding and the shape of the curves is consistent with an ellipse. The folded protein is stabilized by minimizing the exposed surface area of hydrophobic monomers, thereby limiting the number of interfacial water molecules forced to pay an entropic cost for hydrogen-bonding around the protein. This corresponds to the more compact conformations shown in bottom panels of Fig. 5.7. Upon increasing

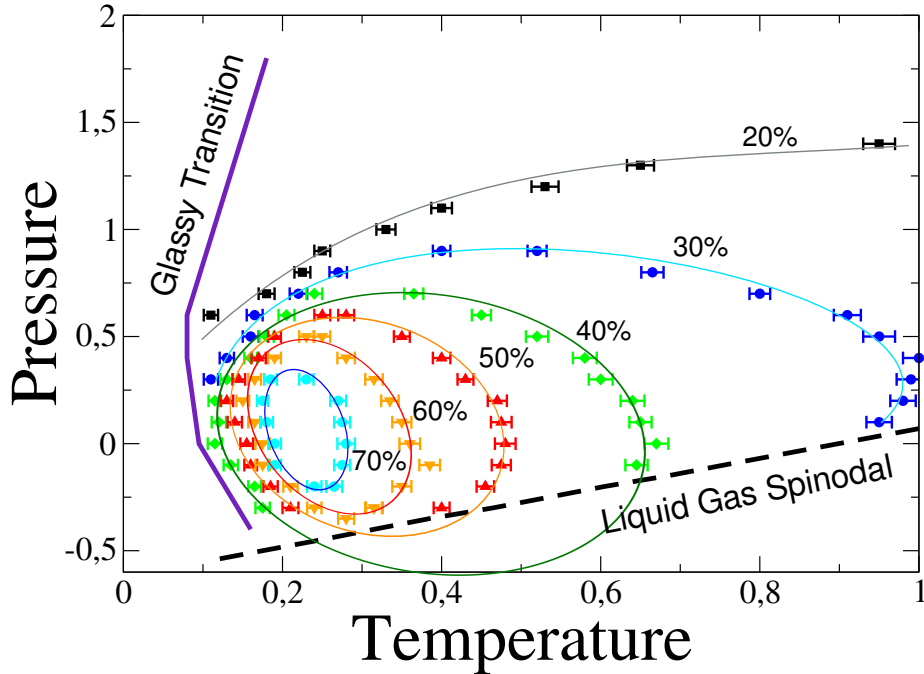


Figure 5.6: Stability region for the initial set of parameters $J = 0.3$, $J_{\text{surf}} = 0.55$, $v_{\text{surf}} = 0.5 - 0.5P$.

temperature, the protein gradually unfolds exposing more hydrophobic monomers to the solvent. Thermal fluctuations dominate the system, overcoming the entropic cost of forming additional interfacial HBs around the exposed monomers. Conformations of thermally denatured protein are shown in top panels of Fig. 5.7. At low T the denaturation process is led by the enthalpy bonus, due to the additional formation of HBs in the hydration shell. The open protein conformation allows to maximize the HB number of the interface.

The change of interfacial density with P makes it increasingly favorable the unfolding because of decrease in enthalpy $-J_{\text{surf}} + P\tilde{v} - kP^2$ upon pressurization and depressurization. Consistently with the theory, at high P the denaturation is accompanied by decrease of volume $\Delta V_{\text{surf}} < 0$ while $\Delta V_{\text{surf}} > 0$ at low P . Actually in our model the unfolding is associated with a break of some HBs in the bulk and with the formation of new HBs in the hydration shell. The corresponding volume change is

$$\Delta V = v_{\text{HB}}\Delta N_{\text{HB}} + \tilde{v}\Delta N_{\text{HB}}^{(s)} - kP\Delta N_{\text{HB}}^{(s)} \quad (5.18)$$

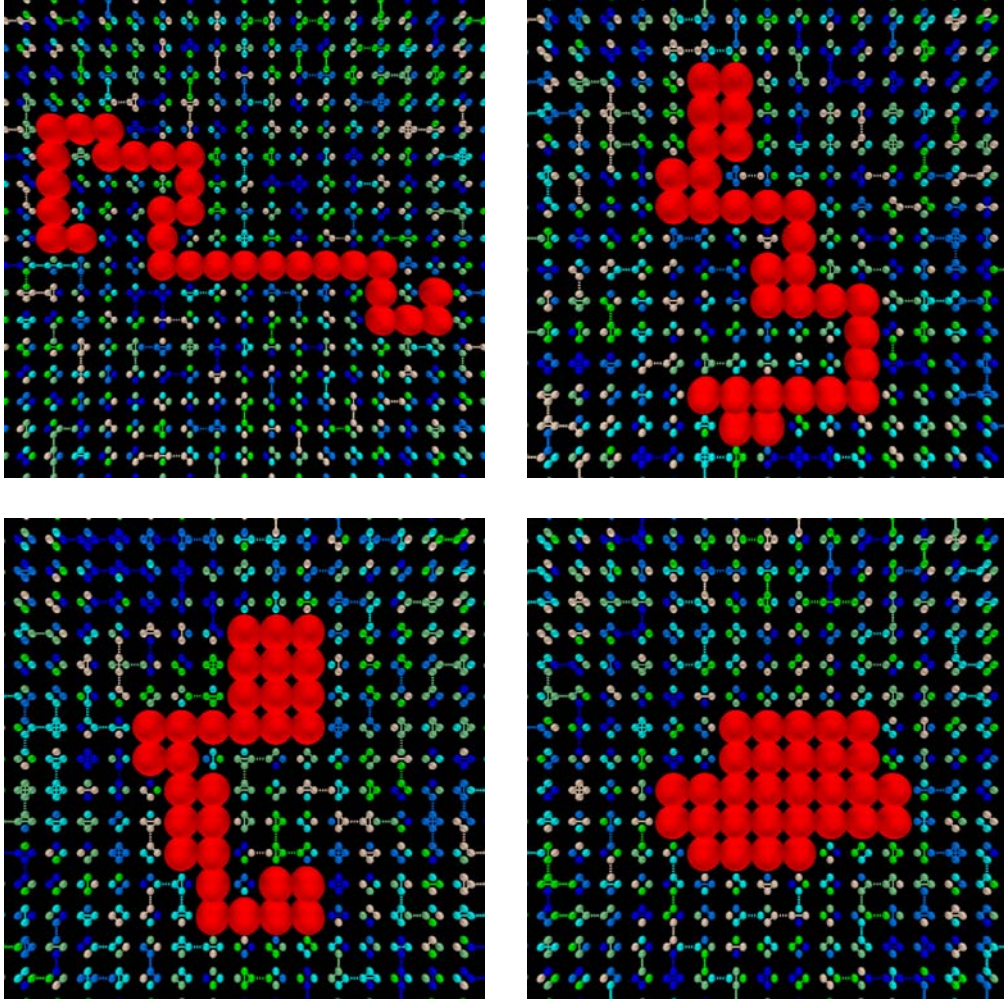


Figure 5.7: Protein configurations with 0%, 25%, 50% and 85% of the possible contact points. Different colors represent different bonding state of σ variables.

where ΔN_{HB} and $\Delta N_{\text{HB}}^{(s)}$ are the change in the HB number respectively in the bulk and at the interface. The sign of ΔV is negative in the limit of high P and turn to be positive in the opposite limit.

It is possible to calculate an analytic expression for the coexistence line. Infact the free energy change $\Delta G \equiv G_u - G_f$ must be zero at the transition point, so that we can write

$$U_u + PV_u - TS_u = U_f + PV_f - TS_f \quad (5.19)$$

Substituting the energy and volume in terms of the Hamiltonian model we find

$$k\Delta N_{\text{HB}}^{(s)}P^2 - (v_{\text{HB}}\Delta N_{\text{HB}} + \tilde{v}\Delta N_{\text{HB}}^{(s)})P + J\Delta N_{\text{HB}} + J_{\text{surf}}\Delta N_{\text{HB}}^{(s)} + J_{\sigma}\Delta N_{\text{coop}} + T\Delta S = 0 \quad (5.20)$$

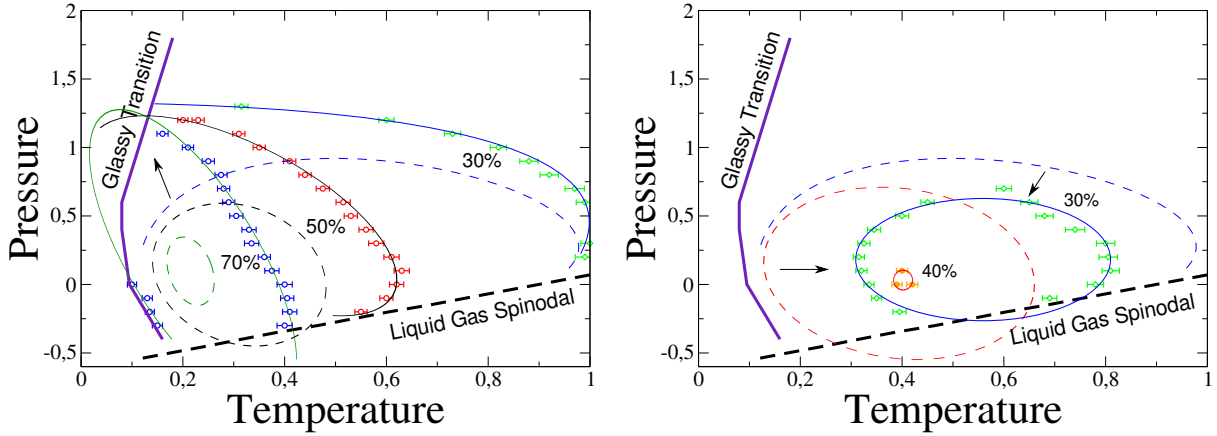


Figure 5.8: Comparison between stability region of Fig. 5.6 (dotted lines) and the stability regions for lower interfacial HB strength $J_{\text{surf}} = 0.20$ (left panel) and for still higher $J_{\text{surf}} = 0.75$ (right panel).

Equation (5.20) explicitly links the transition temperature and pressure with the model parameters and the variation of bulk and interfacial HBs.

5.4.1 Tune of strength of interfacial HB and hydration shell density

The importance of the entropic penalty and the enthalpic bonus in cold and pressure denaturation is given by the combination of two terms J_{surf} and v_{surf} . Changing the strength of the interfacial HB J_{surf} distorts the phase diagram. In Fig. 5.4.1 we evaluate the change of phase diagram considering two values $J_{\text{surf}} = 0.2$ and $J_{\text{surf}} = 0.75$, respectively smaller and bigger with respect to J . In the first case there is no enthalpic gain in the unfolding process as long as $v_{\text{HB}} \sim v_{\text{surf}}$, because interfacial HBs are weaker than bulk HBs. The SR is strongly stretched toward lower T and higher P , increasing the range of T and P where the native state is stable. The eccentricity of the ellipses tends toward 1 and its transverse diameter increases the negative slope. Cold-denaturation is still observable at low P (eventually negative) where the polymer partially opens, while it is lost at high P .

For further increase of J_{surf} the SR is lost, due to the fact that formation of interfacial HBs is even more favorable. The contour lines, while maintaining the shape, are pushed and shifted at higher T .

The density of water molecules in the hydration shell depends on the volume $v_{\text{surf}} \equiv \tilde{v} - kP$ associate to interfacial HBs. Changing the functional form maintaining $dv_{\text{surf}}/dP < 0$

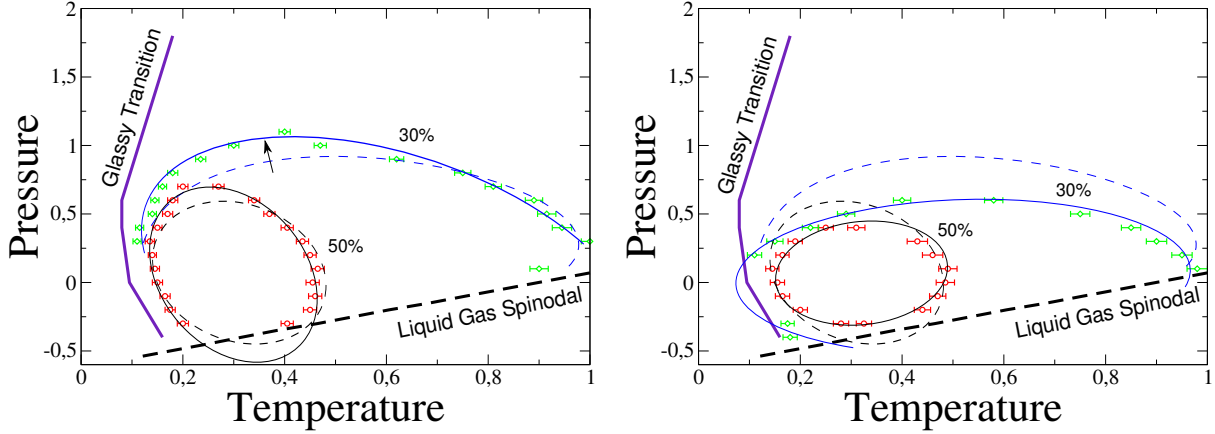


Figure 5.9: Comparison between stability region of Fig. 5.6 (dotted lines) and the stability regions for lower (left panel) and higher (right panel) compressibility factor, related respectively to $k = 0.4$ and $k = 1$.

does not affect substantially the obtained results ². The volume change associate to the $f \rightarrow u$ process is given by eq. 5.18. At high T the thermal denaturation is an entropy driven process and the HB dynamic is not relevant for the process because the average number of HB per molecule is small. So we can approximate $\Delta N_{\text{HB}} \sim 0$ and consider $\Delta N_{\text{HB}}^{(s)}$ as a function slowly varying with the pressure ³ (these approximations are confirmed by simulation results). Then we can relate the parameter k to the compressibility factor β at high T

$$\beta \equiv -\frac{\partial V}{\partial P} \sim 2k\Delta N_{\text{HB}}^{(s)} \quad (5.21)$$

Changing k determines a stretching of the SR along the P direction and a rotation of the ellipse axes. Decrease in compressibility factor (left panel of Fig. 5.4.1) results in an extension of the SR area in the $T - P$ plane, with an increase of the negative slope of the transverse diameter. On the contrary, an increase of k (right panel of Fig. 5.4.1) rotates the coexistence line counterclockwise and reduces the SR area. The lines where $\Delta S = 0$ and $\Delta V = 0$, joining the points where of the slope of the coexistence line is respectively $\partial P/\partial T = 0$ and $\partial P/\partial T = \infty$ (Fig. 5.1), increase the slope turning to be positive, as observed in the experiments [191].

²We considered exponential and quadratic decay of v_{surf} with P getting in both cases a close SR, even if with a distorted shape.

³Actually $\Delta N_{\text{HB}}^{(s)}$ depends on the length l of the protein.

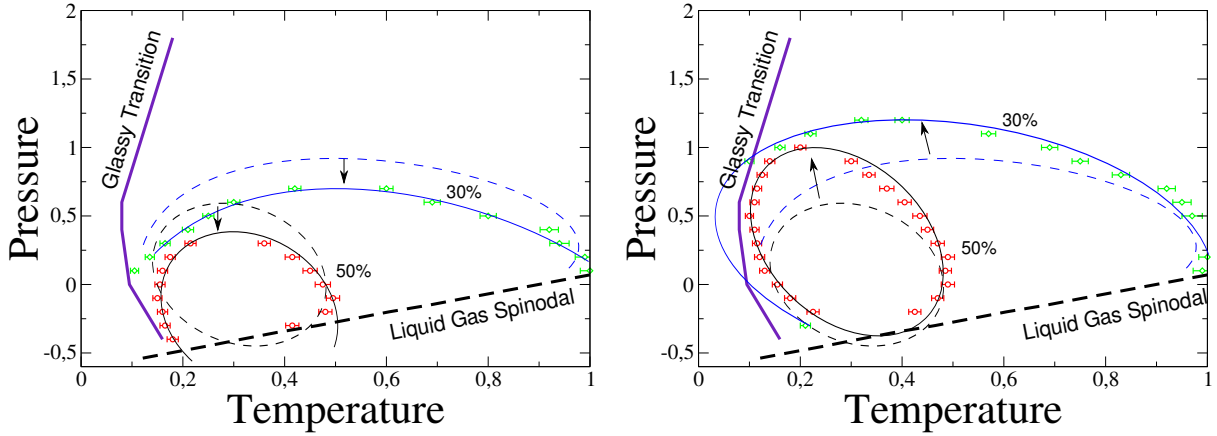


Figure 5.10: Comparison between stability region of Fig. 5.6 (dotted lines) and the stability regions for $\tilde{v} = 0.3$ (left panel) and higher (right panel) $\tilde{v} = 0.7$.

The parameter \tilde{v} represents the volume associate to the HB in the hydration shell at $P = 0$. An increase or decrease of \tilde{v} shifts the SR respectively at higher P (expanding also the SR) and at lower P . In Fig. 5.10 we show the case of $\tilde{v} = 0.3$ (left panel) and $\tilde{v} = 0.7$ (right panel).

If no energetic gain and no pressure change of hydration density are taken into account the SR loses completely its shape. The case $J = J_{\text{surf}}$ and $v_{\text{surf}} = v_{\text{HB}}$, equivalent to embed the polymer in water without affecting its dynamic, is shown in the left panel of Fig. 5.4.1. The SR has a negative slope at low P , turning to infinite slope at high P . No cold denaturation is observed (even if N_{cpts} along isobars shows a maximum at $T \neq 0$) and the folding is completely driven by enthalpy of bulk water.

Interestingly, if we consider that no volume change takes place at the interface ($v_{\text{surf}} = 0$), the cold- and pressure- denaturation is observed, but with a dome in the SR resembling the results of model proposed by Patel et al. [226] (right panel of Fig. 5.4.1). The SR enlarges at higher T as $J_{\text{surf}} > J$. This happens in the model because the effective covalent component of the HBs in the bulk $J - v_{\text{HB}}P$ decreases with pressure while the interfacial bonds are P -independent making the unfolding process energetically favorable whenever $J - v_{\text{HB}}P > 0$. Further decrease of $v_{\text{surf}} < 0$ results in a still broader T -range of the SR and lower value of the its maximum P , shifted at higher T (data not shown).

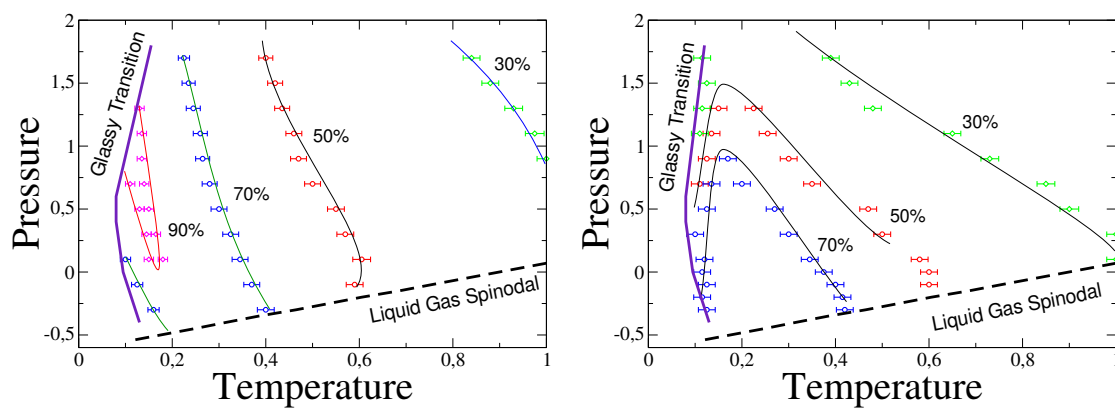


Figure 5.11: **Left panel:** phase diagram of the polymer without any effect on water. **Right panel:** Phase diagram for $J = J_{\text{surf}}$ and $v_{\text{surf}} = 0$.

Chapter 6

Conclusions

In this thesis we presented a coarse-grained model for a mono-layer of water and its extension to the case of solvated proteins. The model takes into account the cooperativity between HBs and has been studied by Monte Carlo simulations.

In chapter 3, we analyze the low- T phase diagram of a water mono-layer confined between hydrophobic parallel walls of size L separated by $h \approx 0.5$ nm. We calculate the loci of temperature of maximum and minimum density, and the locus of maxima in ξ that defines the Widom line. We found two loci of extrema for each thermodynamic response functions: the stronger one at low- T , coinciding with the Widom line, and the weaker and broader one at high- T . Such results about the phase diagram, and the response functions C_P , α_P and K_T of the model and the connection of these quantities with the HBs dynamics are in agreement with experimental results and validate the model. We find a liquid-liquid critical point in the deep supercooled region, at the end of a line of first order transition between two liquid phases characterized by different values of energy and density. The LLCP belongs to the 2D Ising universality class only for $L/h \geq 50$. Surprisingly, we show that by confining the mono-layer within walls with small L one “lifts”, instead of decreasing, the class of the LLCP to 3D, bulk-like, Ising universality. We rationalize this effect as a consequence of (i) the high cooperativity of the HB network and (ii) its low coordination number at low T that makes the mono-layer similar to bulk within the first coordination shell.

In chapter 4, we present a geometric description of correlated region of water molecules to typify the liquid phase. Cluster of molecules are built following the percolation approach proposed by Kastelein-Fortuin and Coniglio-Klein. The probability that two interacting molecules belong to the same cluster depends on the thermodynamic conditions of T and P . We find that the LL-phase transition line and the Widom line are characterized by

continuous percolation line where cluster distribution decays as power law function. This line marks the region where the fluctuations of HB spans all over the network. At low P the percolation, related to local tetrahedral rearrangement of HB network, happens when the system already has formed a great number of HBs. Loci of maxima in correlation and connectivity length point out that in our model Widom line and Kertész line coincide. At high P the percolation is associated to the sharp formation of HBs, giving rise to discontinuous change in density in turn associated to the HDL-LDL phase transition. Scaling of the percolation order parameter and of the mean cluster size at the LLCP agrees with Ising universality class in 2D. The presence of LLCP is also marked by different size behavior of mean cluster size and fractal dimension of the spanning clusters.

In chapter 5, we adapt the water cell model in the context of protein folding. Without entering in the complex mechanism of protein folding we study how the HBs network stabilizes the native state of protein. For the sake of simplicity we consider the case of a protein schematized as a self-avoiding hydrophobic homopolymer and limit our discussion to a 2D model. We assume that the network of HBs is perturbed by the presence of hydrophobic solute with large size leading to interaction among the water molecules at the interface that are stronger than in the bulk, and to a larger number of broken HBs with respect to the bulk. We also assume that the density of hydration shell increase upon pressurization. The model protein denatures at high temperature, low temperature, high pressure and low pressure showing many of the same denaturation characteristics observed in experiments. The stability region, where the native state of protein is stable, has an elliptic-like shape according to theory. We study also the dependence of the stability region on the parameters of the model finding that both energetic gain for interfacial HBs and compressible hydration shell are essentially the underlying mechanism leading to a close stability region in the $T - P$ plane.

Appendix A: Usefull thermodynamic relations

We report here the calculations for the thermodynamic relations in eq. 3.6, 3.8 and 3.10 [41]. To verify the relation 3.10 we calculate the derivative of K_T along isobars

$$\left(\frac{\partial K_T}{\partial T}\right)_P = \frac{\partial}{\partial T} \left(-\frac{1}{V} \frac{\partial V}{\partial P}\right) = \frac{1}{V^2} \left(\frac{\partial V}{\partial T}\right)_P \left(\frac{\partial V}{\partial P}\right)_T - \frac{1}{V} \frac{\partial^2 V}{\partial P \partial T} = \alpha_P K_T - \frac{1}{V} \frac{\partial^2 V}{\partial P \partial T} \quad (6.1)$$

and the derivative of α_P along isotherms

$$\begin{aligned} \left(\frac{\partial \alpha_P}{\partial P}\right)_T &= \frac{\partial}{\partial P} \left(\frac{1}{V} \frac{\partial V}{\partial T}\right) = -\frac{1}{V^2} \left(\frac{\partial V}{\partial P}\right)_T \left(\frac{\partial V}{\partial T}\right)_P + \frac{1}{V} \frac{\partial^2 V}{\partial T \partial P} = \\ &= -\alpha_P K_T + \frac{1}{V} \frac{\partial^2 V}{\partial P \partial T} = -\left(\frac{\partial K_T}{\partial T}\right)_P \end{aligned} \quad (6.2)$$

Following [41, 128] the TMD line is characterized by $d\alpha_P = 0$ and $\alpha = 0$. Hence

$$d\alpha_P = 0 = \left(\frac{\partial \alpha_P}{\partial T}\right)_P dT + \left(\frac{\partial \alpha_P}{\partial P}\right)_T dP = \left(\frac{1}{V} \frac{\partial^2 V}{\partial T^2}\right)_P dT + \left(\frac{1}{V} \frac{\partial^2 V}{\partial P \partial T}\right)_T dP \quad (6.3)$$

which gives the slope $\partial P/\partial T$ of TMD

$$\left(\frac{\partial P}{\partial T}\right)_{TMD} = -\frac{\frac{\partial^2 V}{\partial T^2}}{\frac{\partial^2 V}{\partial P \partial T}} \quad (6.4)$$

from which, using eq. 6.1 for $\alpha_P = 0$, we get rel. 3.6.

To calculate the rel. 3.8 we start from C_P and α_P written in terms of Gibbs free energy

$$\frac{C_P}{T} = -\frac{\partial^2 G}{\partial T^2} \quad , \quad V\alpha_P = \frac{\partial^2 G}{\partial P \partial T} \quad (6.5)$$

from which results

$$\begin{aligned} \frac{\partial}{\partial P} \left(\frac{C_P}{T} \right)_T &= \frac{1}{T} \left(\frac{\partial C_P}{\partial P} \right)_T = -\frac{\partial}{\partial T} (V\alpha_P)_P = -\left(\frac{\partial V}{\partial T} \right)_P \alpha_P - V \left(\frac{\partial \alpha_P}{\partial T} \right)_P = -\frac{\partial^2 V}{\partial T^2} \\ \left(\frac{\partial C_P}{\partial P} \right)_T &= -T \frac{\partial^2 V}{\partial T^2} \end{aligned} \quad (6.6)$$

Substituting in eq. 6.4 we get the rel. 3.8.

Appendix B: Theory of scaling fields

The renormalization group (RG) studies the set of mathematical transformations of coupling constants of a physical system, in correspondence of a change in length (or energy) scale $x \rightarrow x' = x/b$ and in lattice space $a \rightarrow a' = ab$. To each RG transformations is associated a blocking reduction of the degrees of freedom. The basic assumption of RG is that a physical system has different length scales that are locally coupled. It means that fluctuations on a scale of $1 - 2 \text{ \AA}$ influence fluctuations on a scale of $2 - 4 \text{ \AA}$, in turn these influence fluctuations on a scale of $4 - 8 \text{ \AA}$, and so on. For each length scale we have an effective Hamiltonian, characterized by a set of coupling constant. In the renormalization process it is possible that the new Hamiltonian does not have the same functional form of the previous one. This could happen when the set of coupling constant is finite ¹.

Let state with \mathbf{C} the initial set of n coupling constants C_i with $i = 1 \dots n$ of the Hamiltonian $H(s)$. Under RG transformation the old couplings determine the the new ones

$$\mathbf{C}' = \mathbf{R}(\mathbf{C}) \tag{6.7}$$

so that the i th coupling is given by $C'_i = \mathbf{R}_i(\mathbf{C})$. \mathbf{R} in general is a complicated non linear transformation. At length scales smaller with respect the statistical correlation length ξ a system exhibits a symmetry known as scale invariance ². Close a critical point the correlation length ξ diverge and statistical fluctuations spread over all distances and the scale invariance holds at all length scales. The critical phase can be described by a special set of couplings \mathbf{C}^* which are invariant under RG transformation. Hence the condition of criticality is

$$\mathbf{C}^* = \mathbf{R}(\mathbf{C}^*) . \tag{6.8}$$

\mathbf{C}^* is a fixed point in the space of couplings. A fixed point can be determined with a first

¹For this reason it is good to enlarge the set of coupling constants to all those compatible with the nature of the variables and the symmetry of the system.

²This is true as long as we do not consider fluctuations of atomic scales, of the order of lattice space.

order expansion of the eq. 6.7

$$\mathbf{C}^* + \delta\mathbf{C}' = \mathbf{R}(\mathbf{C}^* + \delta\mathbf{C}) \simeq \mathbf{R}(\mathbf{C}^*) + \mathbf{M}\delta\mathbf{C} \quad (6.9)$$

yielding

$$\delta C'_i = \sum_j M_{ij} \delta C_j \quad (6.10)$$

where the matrix \mathbf{M} , defined by

$$M_{ij} = \frac{\partial \mathbf{R}_i}{\partial C_j} \quad (6.11)$$

is not necessary symmetric. To analyze the eq. 6.11 we diagonalize \mathbf{M}

$$\sum_j K_j^i M_{ij} = \lambda^i K^i \quad (6.12)$$

where K^i 's are the eigenvectors given by a linear combination of δC_i and λ^i 's are the eigenvalues (applied on the left of \mathbf{M}). The scaling fields u_i are defined as linear combination of vectors K^i and deviations δC_i

$$u_i \equiv \sum_j K_j^i \delta C_j . \quad (6.13)$$

Apply RG transformation to the fields u_i results in

$$u'_i = \sum_j K_j^i \delta C'_j = \sum_{j,l} K_j^i M_{jl} \delta C_l = \sum_l \lambda^i K_l^i \delta C_l = \lambda^i u_i . \quad (6.14)$$

It means that the renormalization process acts multiplicatively with respect the fields u_i . The corresponding operator, conjugate of the field u_i is given by $\partial/\partial u_i$ (for more details see ref [150]).

The eigenvalues are usually written as λ^{y_i} where the exponent y_i are improperly called eigenvalues. Depending if $y_i > 0$, $y_i = 0$ or $y_i < 0$ the corresponding scaling field is said respectively ‘‘relevant’’, ‘‘marginal’’ or ‘‘irrelevant’’. This naming follows from behavior of these fields under the scale changes of the RG. The relevant fields tend to grow under RG transformation and become more and more important as larger distance scales are reached ³. The irrelevant fields diminish with successive renormalization becoming effec-

³In the standard critical phenomena problem there are three relevant fields: i) the field that breaks the system symmetry, like the magnetic field in the Ising model; ii) the ordering field represented by the temperature; iii) the constant field that scales as λ^d .

tively zero at large scales. These fields makes irrelevant changes to criticality and produce the universality. The marginal fields, if they exist, do not change with the scale breaking the universality.

Case study: Liquid-Gas critical point in Lennard-Jones system

It is known that Ising model, viewed as lattice gas, has a particle-hole symmetry at the critical point. However more realistic models of fluids loose this symmetry. In a Lennard-Jones system, described by the potential

$$U(r) = 4\epsilon \left[\left(\frac{r_0}{r} \right)^{12} - \left(\frac{r_0}{r} \right)^6 \right] \quad (6.15)$$

the LG critical point is described by two non-trivial parameters values, the chemical potential μ_c and the critical well depth ϵ_c . The scaling field which are appropriate to describe the critical behavior are given by a linear combinations of μ and ϵ from their critical values

$$\tau = \epsilon_c - \epsilon + s(\mu - \mu_c) \quad (6.16)$$

$$h = \mu - \mu_c + r(\epsilon_c - \epsilon) \quad (6.17)$$

where s and r are system dependent parameters. We can define two relevant densities which are conjugate to the fields τ and h (conjugate operators)

$$\langle E \rangle = \frac{1}{\langle V \rangle} \frac{\partial \ln Z_N}{\partial \tau} = \frac{1}{1 - rs} (u - r\rho) \quad (6.18)$$

$$\langle M \rangle = \frac{1}{\langle V \rangle} \frac{\partial \ln Z_N}{\partial h} = \frac{1}{1 - rs} (\rho - su) \quad (6.19)$$

where Z_N is the gran canonical partition function. $\langle E \rangle$ and $\langle M \rangle$ are recognizable in the Ising context as the energy density and magnetization respectively. The joint distribution of energy and density is simply related to the joint distribution of the mixed operators:

$$p_L(\rho, u) = \frac{1}{1 - sr} p_L(M, E) . \quad (6.20)$$

At the critical point the the distribution $p_L(M) = \int dE p_L(M, E)$ recovers the right symmetry [138, 139, 141, 151].

Appendix C: Histogram reweighting method

The idea of using histograms to extract information from Monte Carlo simulations was applied with success by Ferrenberg and Swendsen [142, 143] to study critical phenomena. We consider an initial set of n independent simulations in a small range of T and P . For each one we calculate the histograms $h_i(E, V)$ in the energy-volume plane ($i = 1 \dots n$) with common bins. The histograms $h_i(E, V)$ provide an estimation of the equilibrium probability distribution; this estimations become correct in the limit of infinite run. This method allows to calculate histograms, i.e. new probability distribution of the system, for new values of $\beta' = 1/k_B T'$ and P' close the simulated ones. In the case on NPT ensemble, the new histogram $h(V, E, P', \beta')$ is given by relation

$$h(V, E, P', \beta') = \frac{\sum_{i=1}^n h_i(V, E) e^{-\beta'(E+P'V)}}{\sum_{i=1}^n N_i e^{-\beta_i(E+P_iV)-C_i}} \quad (6.21)$$

where N_i is the sum of independent measurements of the run i . The constants C_i , related to the Gibbs free energy value at T_i and P_i , are self-consistently calculated from the equation

$$e^{C_i} = \sum_V \sum_E h(V, E, P_i, \beta_i) \sim Z(P_i, \beta_i) = -G(P_i, \beta_i)/k_B T . \quad (6.22)$$

A good initial set of parameters is $C_i = 0$. Eq. 6.21 and 6.22 are recursively calculated until the difference between values of couples of parameters C_i , calculated at iteration k and $k + 1$, is constants inside the desired numerical resolution.

Bibliography

- [1] C.W. Kern and M. Karplus. *Water: A Comprehensive Treatise*, volume 1, pages 21–91. Plenum Press, New York, 1972.
- [2] G. Franzese and M. Rubi, editors. *Aspects of Physical Biology: Biological Water, Protein Solutions, Transport and Replication*, volume 752 of *Lecture Notes in Physics*. Springer Berlin / Heidelberg, 2008.
- [3] P. Ball. *Life's Matrix: A Biography of Water*. Farrar, Straus and Giroux, 2000.
- [4] S. Zou, J. S. Baskin and A. H. Zewail. Molecular recognition of oxygen by protein mimics: Dynamics on the femtosecond to microsecond time scale. *Proc. Natl. Acad. Sci. USA*, 99(15):9625–9630, 2002.
- [5] P. Ball. Water as an active constituent in cell biology. *Chem. Rev.*, 108(1):74–108, 2008.
- [6] Ken A. Dill, Thomas. M. Truskett, V. Vlachy and B. H.-Lee. Modeling water, the hydrophobic effect and ion solvation. *Annu. Rev. Bioph. Biom.*, 34(1):173–199, 2005.
- [7] L. D. Barron, L. Hecht and G. Wilson. The lubricant of life: a proposal that solvent water promotes extremely fast conformational fluctuations in mobile heteropolypeptide structure. *Biochemistry*, 36:13143–7, 1997.
- [8] V. K.-Siebert, R. Agarwal and J. C. Smith. Hydration-dependent dynamical transition in protein: Protein interactions at 240 k. *Phys. Rev. Lett.*, 100(13):138102, 2008.
- [9] P. Ball. Water: Water — an enduring mystery. *Nature*, 452(7185):291–292, 2008.
- [10] P. G. Debenedetti and H. E. Stanley. Supercooled and glassy water. *Phys. Today*, 56(6):40–46, 2003.

-
- [11] D. Rosenfeld and W. L. Woodley. Deep convective clouds with sustained supercooled liquid water down to -37.5° C. *Nature*, 405(6785):440–442, 2000.
- [12] P. G. Debenedetti. *Metastable Liquids. Concepts and Principles*. Princeton University Press, Princeton, NJ, 1996.
- [13] B. M. Cwilong. Sublimation in a wilson chamber. *Proc. Roy. Soc. Lond. A Mat.*, 190(1020):137–143, 1947.
- [14] H. Kanno, R. J. Speedy and C. A. Angell. Supercooling of water to -92° C under pressure. *Science*, 189(4206):880–881, 1975.
- [15] C. A. Angell. Insights into phases of liquid water from study of its unusual glass-forming properties. *Science*, 319(5863):582–587, 2008.
- [16] P. Needham. Hydrogen bonding: Homing in on a tricky chemical concept. *Stud. Hist. Philos. Sci. A*, 44(1):51–65, 2013.
- [17] J. Poater, X. Fradera, M. Solà, M. Duran and S. Simon. On the electron-pair nature of the hydrogen bond in the framework of the atoms in molecules theory. *Chem. Phys. Lett.*, 369(1-2):248–255, 2003.
- [18] E. D. Isaacs, A. Shukla, P. M. Platzman, D. R. Hamann, B. Barbiellini and C. A. Tulk. Compton scattering evidence for covalency of the hydrogen bond in ice. *J. Phys. Chem. Solids*, 61(3):403–406, 2000.
- [19] A. K. Soper and M. A. Ricci. Structures of high-density and low-density water. *Phys. Rev. Lett.*, 84(13):2881–2884, 2000.
- [20] E. A. Zheligovskaya and G. G. Malenkov. Crystalline water ices. *Russ. Chem. Rev.*, 75:57–76, 2006.
- [21] T. Loerting and N. Giovambattista. Amorphous ice: Experiments and numerical simulation. *J. Phys.: Cond. Mat.*, 18:R919–R977, 2006.
- [22] P. H. Poole, F. Sciortino, U. Essmann and H. E. Stanley. Phase-behavior of metastable water. *Nature*, 360(6402):324–328, 1992.
- [23] H. Tanaka. A self-consistent phase diagram for supercooled water. *Nature*, 380:328–330, 1996.

- [24] L. Xu, P. Kumar, S. V. Buldyrev, S.-H. Chen, P. H. Poole, F. Sciortino and H. E. Stanley. Relation between the Widom line and the dynamic crossover in systems with a liquid-liquid phase transition. *Proc. Natl. Acad. Sci. USA*, 102(46):16558–16562, 2005.
- [25] G. Franzese and H. E. Stanley. The widom line of supercooled water. *J. Phys.: Cond. Mat.*, 19(20):205126, 2007.
- [26] P. F. McMillan and H. E. Stanley. Fluid phases: Going supercritical. *Nat. Phys.*, 6:479–480, 2010.
- [27] B. Widom and J. S. Rowlinson. New model for the study of liquid–vapor phase transitions. *J. Chem. Phys.*, 52(4):1670–1684, 1970.
- [28] B. Widom and F. H. Stillinger. Critical-point thermodynamics of fluids without hole-particle symmetry. *J. Chem. Phys.*, 58(2):616–625, 1973.
- [29] R. J. Speedy. Limiting forms of the thermodynamic divergences at the conjectured stability limits in superheated and supercooled water. *J. Phys. Chem.*, 86(15):3002–3005, 1982.
- [30] P. G. Debenedetti. Supercooled and glassy water. *J. Phys.: Cond. Mat.*, 15(45):R1669–R1726, 2003.
- [31] P. G. Debenedetti and M. C. D’Antonio. Stability and tensile strength of liquids exhibiting density maxima. *AIChE J.*, 34(3):447–455, 1988.
- [32] P. H. Poole, F. Sciortino, T. Grande, H. E. Stanley and C. A. Angell. Effect of hydrogen bonds on the thermodynamic behavior of liquid water. *Phys. Rev. Lett.*, 73(12):1632–1635, 1994.
- [33] H. Tanaka. Phase behaviors of supercooled water: Reconciling a critical point of amorphous ices with spinodal instability. *J. Chem. Phys.*, 105(12):5099–5111, 1996.
- [34] D. Paschek, A. Rüppert and A. Geiger. Thermodynamic and structural characterization of the transformation from a metastable low-density to a very high-density form of supercooled TIP4P-Ew model water. *Chem. Phys. Chem.*, 9(18):2737–2741, 2008.

- [35] Y. Liu, A. Z. Panagiotopoulos and P. G. Debenedetti. Low-temperature fluid-phase behavior of ST2 water. *J. Chem. Phys.*, 131(10):104508, 2009.
- [36] J. L. F. Abascal and C. Vega. Widom line and the liquid-liquid critical point for the TIP4P/2005 water model. *J. Chem. Phys.*, 133(23):234502, 2010.
- [37] Y. Liu, J. C. Palmer, A. Z. Panagiotopoulos and P. G. Debenedetti. Liquid-liquid transition in ST2 water. *J. Chem. Phys.*, 137(21):214505, 2012.
- [38] T. Kesselring, G. Franzese, S. Buldyrev, H. Herrmann and H. E. Stanley. Nanoscale dynamics of phase flipping in water near its hypothesized liquid-liquid critical point. *Sci. Rep.*, 2:474, 2012.
- [39] P. H. Poole, R. K. Bowles, I. S.-Voivod and F. Sciortino. Free energy surface of ST2 water near the liquid-liquid phase transition. *J. Chem. Phys.*, 138(3):034505–7, 2013.
- [40] C. A. Angell. Insights into phases of liquid water from study of its unusual glass-forming properties. *Science*, 319(5863):582–587, 2008.
- [41] S. Sastry, P. G. Debenedetti, F. Sciortino and H. E. Stanley. Singularity-free interpretation of the thermodynamics of supercooled water. *Phys. Rev. E*, 53(6):6144–6154, 1996.
- [42] V. Holten, D. T. Limmer, V. Molinero and M. A. Anisimov. Nature of the anomalies in the supercooled liquid state of the mw model of water. *J. Chem. Phys.*, 138(17):174501–11, 2013.
- [43] V. Molinero and E. B. Moore. Water modeled as an intermediate element between carbon and silicon. *J. Phys. Chem. B*, 113(13):4008–4016, 2009.
- [44] D. T. Limmer and D. Chandler. The putative liquid-liquid transition is a liquid-solid transition in atomistic models of water. *J. Chem. Phys.*, 135(13):134503, 2011.
- [45] F. H. Stillinger and A. Rahman. Improved simulation of liquid water by molecular-dynamics. *J. Chem. Phys.*, 60:1545, 1974.
- [46] F. Sciortino, I. S.-Voivod and P. H. Poole. Study of the ST2 model of water close to the liquid-liquid critical point. *Phys. Chem. Chem. Phys.*, 13:19759–19764, 2011.

- [47] P. H. Poole, S. R. Becker, F. Sciortino and F. W. Starr. Dynamical behavior near a liquid–liquid phase transition in simulations of supercooled water. *J. Phys. Chem. B*, 115(48):14176–14183, 2011.
- [48] E. Lascaris, T. A. Kesselring, G. Franzese, S. V. Buldyrev, H. J. Herrmann and H. E. Stanley. Response functions near the liquid-liquid critical point of ST2 water. *AIP Conf. Proc.*, 1518:520–526, 2013.
- [49] K. Stokely, M. G. Mazza, H. E. Stanley and G. Franzese. Effect of hydrogen bond cooperativity on the behavior of water. *Proc. Natl. Acad. Sci. USA*, 107:1301–1306, 2010.
- [50] A. Faraone, L. Liu, C.-Y. Mou, C.-W. Yen and S.-H. Chen. Fragile-to-strong liquid transition in deeply supercooled confined water. *J. Chem. Phys.*, 121(22):10843–10846, 2004.
- [51] L. Liu, S.-H. Chen, A. Faraone, C.-W. Yen and C.-Y. Mou. Pressure dependence of fragile-to-strong transition and a possible second critical point in supercooled confined water. *Phys. Rev. Lett.*, 95:117802, 2005.
- [52] F. Mallamace, M. Broccio, C. Corsaro, A. Faraone, U. Wanderlingh, L. Liu, C.-Y. Mou and S. H. Chen. The fragile-to-strong dynamic crossover transition in confined water: nuclear magnetic resonance results. *J. Chem. Phys.*, 124(16):161102, 2006.
- [53] S. H. Chen, L. Liu, E. Fratini, P. Baglioni, A. Faraone and E. Mamontov. Observation of fragile-to-strong dynamic crossover in protein hydration water. *Proc. Natl. Acad. Sci. USA*, 103(24):9012–9016, 2006.
- [54] E. Mamontov. Observation of fragile-to-strong liquid transition in surface water in CeO₂. *J. Chem. Phys.*, 123(17):171101, 2005.
- [55] H. Jansson, W. S. Howells and J. Swenson. Dynamics of fresh and freeze-dried strawberry and red onion by quasielastic neutron scattering. *J. Chem. Phys. B*, 110:13786–92, 2006.
- [56] S.-H. Chen, L. Liu, X. Chu, Y. Zhang, E. Fratini, P. Baglioni, A. Faraone and E. Mamontov. Experimental evidence of fragile-to-strong dynamic crossover in dna hydration water. *J. Chem. Phys.*, 125(17):171103, 2006.

- [57] X.-q. Chu, E. Fratini, P. Baglioni, A. Faraone and S.-H. Chen. Observation of a dynamic crossover in rna hydration water which triggers a dynamic transition in the biopolymer. *Phys. Rev. E* , 77(1):011908, 2008.
- [58] G. Franzese, K. Stokely, X. Q. Chu, P. Kumar, M. G. Mazza, S. H. Chen and H. E. Stanley. Pressure effects in supercooled water: comparison between a 2d model of water and experiments for surface water on a protein. *J. Phys.: Cond. Matt.*, 20(49):494210, 2008.
- [59] R. Bergman and J. Swenson. Dynamics of supercooled water in confined geometry. *Nature*, 403(6767):283–286, 2000.
- [60] S. Cervený, J. Colmenero and A. Alegría. Comment on “Pressure dependence of fragile-to-strong transition and a possible second critical point in supercooled confined water”. *Phys. Rev. Lett.*, 97(18):189802, 2006.
- [61] J. Swenson. Comment on “Pressure dependence of fragile-to-strong transition and a possible second critical point in supercooled confined water”. *Phys. Rev. Lett.*, 97(18):189801, 2006.
- [62] S. Pawlus, S. Khodadadi and A. P. Sokolov. Conductivity in hydrated proteins: No signs of the fragile-to-strong crossover. *Phys. Rev. Lett.*, 100(10):108103, 2008.
- [63] M. Vogel. Origins of apparent fragile-to-strong transitions of protein hydration waters. *Phys. Rev. Lett.*, 101(22):225701, 2008.
- [64] Y. Zhang, A. Faraone, W. A. Kamitakahara, K.-H. Liu, C.-Y. Mou, J. B. Le ao, S. Chang and S.-H. Chen. Density hysteresis of heavy water confined in a nanoporous silica matrix. *Proc. Natl. Acad. Sci. USA*, 108(30):12206–12211, 2011.
- [65] A. K. Soper. Density minimum in supercooled confined water. *Proc. Natl. Acad. Sci. USA*, 108(47):E1192, 2011.
- [66] Y. Zhang, A. Faraone, W. A. Kamitakahara, K.-H. Liu, C.-Y. Mou, J. B. Le ao, S. Chang and S.-H. Chen. Reply to soper: Density measurement of confined water with neutron scattering. *Proc. Natl. Acad. Sci. USA*, 108(47):E1193–E1194, 2011.
- [67] P. W. Fenimore, H. Frauenfelder, B. H. McMahon and R. D. Young. Bulk-solvent and hydration-shell fluctuations, similar to α - and β -fluctuations in glasses, control

- protein motions and functions. *Proc. Natl. Acad. Sci. USA*, 101(40):14408–14413, 2004.
- [68] P. W. Fenimore, H. Frauenfelder, B. H. McMahon and R. D. Young. Proteins are paradigms of stochastic complexity. *Physica A*, 351(1):1–13, 2005.
- [69] V. Lubchenko, P. G. Wolynes and H. Frauenfelder. Mosaic energy landscapes of liquids and the control of protein conformational dynamics by glass-forming solvents. *J. Phys. Chem. B*, 109(15):7488–7499, 2005.
- [70] L. Liu, S.-H. Chen, A. Faraone, C.-W. Yen and C.-Y. Mou. Pressure dependence of fragile-to-strong transition and a possible second critical point in supercooled confined water. *Phys. Rev. Lett.*, 95(11):117802, 2005.
- [71] J. Swenson, H. Jansson and R. Bergman. Relaxation processes in supercooled confined water and implications for protein dynamics. *Phys. Rev. Lett.*, 96(24):247802, 2006.
- [72] A. Oleinikova, N. Smolin and I. Brovchenko. Origin of the dynamic transition upon pressurization of crystalline proteins. *J. Phys. Chem. B*, 110(39):19619–19624, 2006.
- [73] I. Brovchenko, A. Krukau, A. Oleinikova and A. K. Mazur. Water percolation governs polymorphic transitions and conductivity of dna. *Phys. Rev. Lett.*, 97(13):137801–4, 2006.
- [74] L. Zhang, L. Wang, Y.-T. Kao, W. Qiu, Y. Yang, O. Okobiah and D. Zhong. From the Cover: Mapping hydration dynamics around a protein surface. *Proc. Natl. Acad. Sci. USA*, 104(47):18461–18466, 2007.
- [75] D. Liu, X.-q. Chu, M. Lagi, Y. Zhang, E. Fratini, P. Baglioni, A. Alatas, A. Said, E. Alp and S.-H. Chen. Studies of phononlike low-energy excitations of protein molecules by inelastic x-ray scattering. *Phys. Rev. Lett.*, 101(13):135501–5, 2008.
- [76] J. M. Zanotti, G. Gibrat and M. C. Bellissent-Funel. Hydration water rotational motion as a source of configurational entropy driving protein dynamics. Crossovers at 150 and 220 K. *Phys. Chem. Chem. Phys.*, 10(32):4865–4870, 2008.
- [77] P. Kumar, Z. Yan, L. Xu, M. G. Mazza, S. V. Buldyrev, S.-H. Chen, S. Sastry and H. E. Stanley. Glass transition in biomolecules and the liquid-liquid critical point of water. *Phys. Rev. Lett.*, 97(17):177802, 2006.

- [78] I. Brovchenko, A. Geiger and A. Oleinikova. Multiple liquid–liquid transitions in supercooled water. *J. Chem. Phys.*, 118(21):9473–9476, 2003.
- [79] G. E. Brown, V. E. Henrich, W. H. Casey, D. L. Clark, C. Eggleston, A. Felmy, D. W. Goodman, M. Grätzel, G. Maciel, M. I. McCarthy, K. H. Nealson, Dimitri A. Sverjensky, M. F. Toney and J. M. Zachara. Metal oxide surfaces and their interactions with aqueous solutions and microbial organisms. *Chem. Rev.*, 99(1):77–174, 1999.
- [80] P. Jungwirth, B. J. F.-Pitts and D. J. Tobias. Introduction: Structure and chemistry at aqueous interfaces. *Chem. Rev.*, 106(4):1137–1139, 2006.
- [81] N. Ji, V. Ostroverkhov, C. S. Tian and Y. R. Shen. Characterization of vibrational resonances of water-vapor interfaces by phase-sensitive sum-frequency spectroscopy. *Phys. Rev. Lett.*, 100(9):096102, 2008.
- [82] A. Poynor, L. Hong, I. K. Robinson, S. Granick, Z. Zhang and P. A. Fenter. How water meets a hydrophobic surface. *Phys. Rev. Lett.*, 97(26):266101, 2006.
- [83] B. M. Ocko, A. Dhinojwala and J. Dailant. Comment on “how water meets a hydrophobic surface”. *Phys. Rev. Lett.*, 101:039601, 2008.
- [84] A. Poynor, L. Hong, I. K. Robinson, S. Granick, P. A. Fenter and Z. Zhang. Poynor *et al.* reply:. *Phys. Rev. Lett.*, 101:039602, 2008.
- [85] S. Granick and S. C. Bae. Chemistry: A curious antipathy for water. *Science*, 322(5907):1477–1478, 2008.
- [86] X. Gao and L. Jiang. Biophysics: Water-repellent legs of water striders. *Nature*, 432(7013):36–36, 2004.
- [87] P. Liu, X. Huang, R. Zhou and B. J. Berne. Observation of a dewetting transition in the collapse of the melittin tetramer. *Nature*, (7055):159162, 2005.
- [88] D. M. Huang and D. Chandler. Temperature and length scale dependence of hydrophobic effects and their possible implications for protein folding. *Proc. Natl. Acad. Sci. USA*, 97(15):8324–8327, 2000.
- [89] V. Bianco, S. Iskrov and G. Franzese. Understanding the role of hydrogen bonds in water dynamics and protein stability. *J. Biol. Phys.*, 38(1):27–48, 2012.

- [90] G. Franzese, V. Bianco and S. Iskov. Water at interface with proteins. *Food Biophys.*, 6:186–198, 2011.
- [91] D. A. Doshi, E. B. Watkins, J. N. Israelachvili and J. Majewski. Reduced water density at hydrophobic surfaces: Effect of dissolved gases. *Proc. Natl. Acad. Sci. USA*, 102(27):9458–9462, 2005.
- [92] Z. Ge, D. G. Cahill and P. V. Braun. Thermal conductance of hydrophilic and hydrophobic interfaces. *Phys. Rev. Lett.*, 96:186101, 2006.
- [93] L. B. R. Castro, A. T. Almeida and D. F. S. Petri. The effect of water or salt solution on thin hydrophobic films. *Langmuir*, 20(18):7610–7615, 2004.
- [94] Y. Takata, J.-H. J. Cho, B. M. Law and M. Aratono. Ellipsometric search for vapor layers at liquid-hydrophobic solid surfaces. *Langmuir*, 22(4):1715–1721, 2006.
- [95] M. Mao, J. Zhang, R.-H. Yoon and W. A. Ducker. Is there a thin film of air at the interface between water and smooth hydrophobic solids?. *Langmuir*, 20(5):1843–1849, 2004.
- [96] Y.-S. Seo and S. Satija. No intrinsic depletion layer on a polystyrene thin film at a water interface. *Langmuir*, 22(17):7113–7116, 2006.
- [97] J. W. G. Tyrrell and P. Attard. Images of Nanobubbles on Hydrophobic Surfaces and Their Interactions. *Phys. Rev. Lett.*, 87:176104, 2001.
- [98] N. Ishida, T. Inoue, M. Miyahara and K. Higashitani. Nano bubbles on a hydrophobic surface in water observed by tapping-mode atomic force microscopy. *Langmuir*, 16(16):6377–6380, 2000.
- [99] E. A. Vogler. Structure and reactivity of water at biomaterial surfaces. *Adv. Colloid. Interfac.*, 74:69–117, 1998.
- [100] M.-C. Bellissent-Funel. Water near hydrophilic surfaces. *J. Mol. Liq.*, 96–97(0):287–304, 2002.
- [101] R. C. Major, J. E. Houston, M. J. McGrath, J. I. Siepmann and X.-Y. Zhu. Viscous water meniscus under nanoconfinement. *Phys. Rev. Lett.*, 96:177803, 2006.

- [102] T.-D. Li, J. Gao, R. Szoszkiewicz, U. Landman and E. Riedo. Structured and viscous water in subnanometer gaps. *Phys. Rev. B*, 75:115415, 2007.
- [103] L. F. Boesel and R. L. Reis. The effect of water uptake on the behaviour of hydrophilic cements in confined environments. *Biomaterials*, 27(33):5627–5633, 2006.
- [104] F. Bresme, E. Chacón, P. Tarazona and K. Tay. Intrinsic structure of hydrophobic surfaces: The oil-water interface. *Phys. Rev. Lett.*, 101(5):056102, 2008.
- [105] N. Giovambattista, C. F. Lopez, P. J. Rossky and P. G. Debenedetti. Hydrophobicity of protein surfaces: Separating geometry from chemistry. *Proc. Natl. Acad. Sci. USA*, 105(7):2274–2279, 2008.
- [106] Y. Zhang, A. Faraone, W. A. Kamitakahara, Kao-Hsiang Liu, Chung-Yuan Mou, Juscelino B. Le ao, Sung Chang and S.-H. Chen. Density hysteresis of heavy water confined in a nanoporous silica matrix. *Proc. Natl. Acad. Sci. USA*, 108(30):12206–12211, 2011.
- [107] M. Majumder, N. Chopra, R. A.s and B. J. Hinds. Nanoscale hydrodynamics: Enhanced flow in carbon nanotubes. *Nature*, 438(7064):44–44, 2005.
- [108] M. Whitby and N. Quirke. Fluid flow in carbon nanotubes and nanopipes. *Nat. Nanotechnol.*, 2:87–94, 2007.
- [109] L. Guillemot, T. Biben, A. Galarneau, G. Vigier and É. Charlaix. Activated drying in hydrophobic nanopores and the line tension of water. *Proc. Natl. Acad. Sci. USA*, 109(48):19557–19562, 2012.
- [110] D. R. Paul. Creating new types of carbon-based membranes. *Science*, 335(6067):413–414, 2012.
- [111] R. H. Swendsen and J.-S. Wang. Nonuniversal critical dynamics in monte carlo simulations. *Phys. Rev. Lett.*, 58:86–88, 1987.
- [112] U. Wolff. Collective monte carlo updating for spin systems. *Phys. Rev. Lett.*, 62:361–364, 1989.
- [113] D. Bouzida, S. Kumar and R. H. Swendsen. Efficient monte carlo methods for the computer simulation of biological molecules. *Phys. Rev. A*, 45:8894–8901, 1992.

- [114] R. Zangi and A. E. Mark. Monolayer ice. *Phys. Rev. Lett.*, 91(2):025502, 2003.
- [115] P. Kumar, S. V. Buldyrev, F. W. Starr, N. Giovambattista and H. E. Stanley. Thermodynamics, structure and dynamics of water confined between hydrophobic plates. *Phys. Rev. E*, 72(5):051503, 2005.
- [116] M. Sharma, D. Donadio, E. Schwegler and G. Galli. Probing properties of water under confinement: Infrared spectra. *Nano Lett.*, 8(9):2959–2962, 2008.
- [117] R. R. Nair, H. A. Wu, P. N. Jayaram, I. V. Grigorieva and A. K. Geim. Unimpeded permeation of water through helium-leak-tight graphene-based membranes. *Science*, 335(6067):442–444, 2012.
- [118] J. E. Lennard-Jones. Wave functions of many-electron atoms. *Math. Proc. Cambridge*, 27:469–480, 1931.
- [119] R. Ludwig. Water: From clusters to the bulk. *Angewandte Chemie International Edition*, 40(10):1808–1827, 2001.
- [120] L. H. de la Peña and P. G. Kusalik. Temperature dependence of quantum effects in liquid water. *J. A. Chem. Soc.*, 127(14):5246–5251, 2005.
- [121] F. Bartha, O. Kapuy, C. Kozmutza and C. Van Alsenoy. Analysis of weakly bound structures: hydrogen bond and the electron density in a water dimer. *J. Mol. Struct.*, 666667(0):117–122, 2003.
- [122] R. C. Dougherty. Temperature and pressure dependence of hydrogen bond strength: A perturbation molecular orbital approach. *J. Chem. Phys.*, 109(17):7372–7378, 1998.
- [123] N. Metropolis, A. W. Rosenbluth, M. N. Rosenbluth, A. H. Teller and E. Teller. Equation of state calculations by fast computing machines. *J. Chem. Phys.*, 21(6):1087–1092, 1953.
- [124] V. Cataudella, G. Franzese, M. Nicodemi, A. Scala and A. Coniglio. Critical clusters and efficient dynamics for frustrated spin models. *Phys. Rev. Lett.* 72(10):1541–1544, 1994.

- [125] F. Mallamace, C. Branca, M. Broccio, C. Corsaro, C.-Y. Mou and S.-H. Chen. The anomalous behavior of the density of water in the range $30\text{ K} < T < 373\text{ K}$. *Proc. Natl. Acad. Sci. USA*, 104(47):18387–18391, 2007.
- [126] V. V. Vasisht, S. Saw and S. Sastry. Liquid-liquid critical point in supercooled silicon. *Nat. Phys.*, 7:549–553, 2011.
- [127] I. S.-Voivod, P. H. Poole and F. Sciortino. Density minimum and liquid-liquid phase transition. *J. Phys.: Cond. Mat.*, 17(43), 2005.
- [128] L. P. N. Rebelo, P. G. Debenedetti and S. Sastry. Singularity-free interpretation of the thermodynamics of supercooled water. II. Thermal and volumetric behavior. *J. Chem. Phys.*, 109(2):626–633, 1998.
- [129] M. G. Mazza, K. Stokely, S. E. Pagnotta, F. Bruni, H. E. Stanley and G. Franzese. More than one dynamic crossover in protein hydration water. *Proc. Natl. Acad. Sci. USA*, 108(50):19873–19878, 2011.
- [130] M. G. Mazza, K. Stokely, H. E. Stanley and G. Franzese. Effect of pressure on the anomalous response functions of a confined water monolayer at low temperature. *J. Chem. Phys.*, 137(20):204502, 2012.
- [131] D. Stauffer and A. Aharony. *Introduction To Percolation Theory*. Taylor & Francis, 1994.
- [132] G. Franzese, M. I. Marqués and H. E. Stanley. Intramolecular coupling as a mechanism for a liquid-liquid phase transition. *Phys. Rev. E*, 67(1):011103, 2003.
- [133] P. Kumar, G. Franzese and H. E. Stanley. Predictions of dynamic behavior under pressure for two scenarios to explain water anomalies. *Phys. Rev. Lett.*, 100(10):105701, 2008.
- [134] F. de los Santos and G. Franzese. Understanding diffusion and density anomaly in a coarse-grained model for water confined between hydrophobic walls. *J. Phys. Chem. B*, 115(48):14311–14320, 2011.
- [135] F. de los Santos and G. Franzese. Relations between the diffusion anomaly and cooperative rearranging regions in a hydrophobically nanoconfined water monolayer. *Phys. Rev. E*, 85(1):010602–6, 2012.

-
- [136] M. G. Mazza, K. Stokely, E. G. Strelakova, H. E. Stanley and G. Franzese. Cluster monte carlo and numerical mean field analysis for the water liquid-liquid phase transition. *Comput. Phys. Commun.*, 180(4):497–502, 2009.
- [137] E. G. Strelakova, M. G. Mazza, H. E. Stanley and G. Franzese. Large decrease of fluctuations for supercooled water in hydrophobic nanoconfinement. *Phys. Rev. Lett.*, 106:145701, 2011.
- [138] A. D. Bruce and N. B. Wilding. Scaling fields and universality of the liquid-gas critical point. *Phys. Rev. Lett.*, 68:193–196, 1992.
- [139] N. B. Wilding. Critical-point and coexistence-curve properties of the lennard-jones fluid: A finite-size scaling study. *Phys. Rev. E*, 52:602–611, 1995.
- [140] R. Hilfer and N. B. Wilding. Are critical finite-size scaling functions calculable from knowledge of an appropriate critical exponent?. *J. Phys. A-Math. Gen.*, 28(10):L281, 1995.
- [141] N. B. Wilding and K. Binder. Finite-size scaling for near-critical continuum fluids at constant pressure. *Physica A*, 231(4):439–447, 1996.
- [142] A. M. Ferrenberg and R. H. Swendsen. New monte carlo technique for studying phase transitions. *Phys. Rev. Lett.*, 61:2635–2638, 1988.
- [143] A. M. Ferrenberg and R. H. Swendsen. Optimized monte carlo data analysis. *Phys. Rev. Lett.*, 63:1195–1198, 1989.
- [144] A. Z. Panagiotopoulos. Monte carlo methods for phase equilibria of fluids. *J. Phys.: Cond. Mat.*, 12(3):R25, 2000.
- [145] K. Binder. Critical properties from monte carlo coarse graining and renormalization. *Phys. Rev. Lett.*, 47:693–696, 1981.
- [146] G. Franzese and A. Coniglio. Phase transitions in the potts spin-glass model. *Phys. Rev. E*, 58(3):2753–2759, 1998.
- [147] S. Kullback and R. A. Leibler. On Information and Sufficiency. *Ann. Math. Stat.*, 22:79–86, 1951.

- [148] Y. Liu, A. Z. Panagiotopoulos and P. G. Debenedetti. Finite-size scaling study of the vapor-liquid critical properties of confined fluids: Crossover from three dimensions to two dimensions. *J. Chem. Phys.*, 132(14):144107, 2010.
- [149] P. H. Poole, R. K. Bowles, I. S.-Voivod and F. Sciortino. Free energy surface of ST2 water near the liquid-liquid phase transition. *J. Chem. Phys.*, 138(3):034505, 2013.
- [150] L. P. Kadanoff. *Statistical Physics: Statics, Dynamics and Renormalization*. World Scientific Publishing Company, Incorporated, 2000.
- [151] N. B. Wilding and A. D. Bruce. Density fluctuations and field mixing in the critical fluid. *J. Phys.: Cond. Mat.*, 4(12):3087, 1992.
- [152] C.-K. Hu. Bond-correlated percolation model and the unusual behaviour of supercooled water. *J. Phys. A-Math. Gen.*, 16(10):L321, 1983.
- [153] H. E. Stanley. A polychromatic correlated-site percolation problem with possible relevance to the unusual behaviour of supercooled H₂O and D₂O. *J. Phys. A-Math. Gen.*, 12(12):L329, 1979.
- [154] H. E. Stanley and J. Teixeira. Interpretation of the unusual behavior of H₂O and D₂O at low temperatures: Tests of a percolation model. *J. Chem. Phys.*, 73(7):3404–3422, 1980.
- [155] Y. I. Naberukhin. Continuum model of water and percolation theory. *J. Phys. A-Math. Gen.*, 19(11):L681, 1986.
- [156] P. W. Kasteleyn and C. M. Fortuin. Phase Transitions in Lattice Systems with Random Local Properties. *J. Phys. Soc. Jpn. Suppl.*, 26:11–14, 1969.
- [157] C. M. Fortuin and P. W. Kasteleyn. On the random-cluster model: I. introduction and relation to other models. *Physica*, 57(4):536–564, 1972.
- [158] A. Coniglio, H. E. Stanley and W. Klein. Site-bond correlated-percolation problem: A statistical mechanical model of polymer gelation. *Phys. Rev. Lett.*, 42:518–522, 1979.
- [159] A. Coniglio and W. Klein. Clusters and ising critical droplets: a renormalisation group approach. *J. Phys. A-Math. Gen.*, 13(8):2775, 1980.

- [160] H. E. Stanley. *Introduction to Phase Transitions and Critical Phenomena*, volume 40. Oxford University Press, 1971.
- [161] J. E. Mayer. The statistical mechanics of condensing systems. I. *J. Chem. Phys.*, 5(1):67–73, 1937.
- [162] J. E. Mayer and P. G. Ackermann. The statistical mechanics of condensing systems. II. *J. Chem. Phys.*, 5(1):74–83, 1937.
- [163] J. Frenkel. Statistical theory of condensation phenomena. *J. Chem. Phys.*, 7(3):200–201, 1939.
- [164] J. Frenkel. A general theory of heterophase fluctuations and pretransition phenomena. *J. Chem. Phys.*, 7(7):538–547, 1939.
- [165] M. E. Fisher. The theory of condensation and the critical point. *Physics*, 3:255, 1967.
- [166] N. Sator. Clusters in simple fluids. *Phys. Rep.*, 376(1):1–39, 2003.
- [167] L. B. Partay and P. Jedlovszky. Line of percolation in supercritical water. *J. Chem. Phys.*, 123(2):024502, 2005.
- [168] L. B. Partay, P. Jedlovszky, I. Brovchenko, and A. Oleinikova. Formation of mesoscopic water networks in aqueous systems. *Phys. Chem. Chem. Phys.*, 9:13411346, 2007.
- [169] M. Bernabei, A. Botti, F. Bruni, M. A. Ricci, and A. K. Soper. Percolation and three-dimensional structure of supercritical water. *Phys. Rev. E*, 78:021505, 2008.
- [170] A. Botti, F. Bruni, R. Mancinelli, M. A. Ricci, F. Lo Celso, R. Triolo, F. Ferrante, and A. K. Soper. Study of percolation and clustering in supercritical water-CO₂ mixtures. *J. Chem. Phys.*, 128:164504, 2008.
- [171] M. F. Sykes and D. S. Gaunt. A note on the mean size of clusters in the Ising model. *J. Phys. A-Math. Gen.*, 9(12):2131, 1976.
- [172] C.-K. Hu. Percolation, clusters and phase transitions in spin models. *Phys. Rev. B*, 29:5103–5108, 1984.
- [173] A. Coniglio and F. Peruggi. Clusters and droplets in the q-state potts model. *J. Phys. A-Math. Gen.*, 15(6):1873, 1982.

- [174] C. P. Schioppa, F. Sciortino and P. Tartaglia. Coniglio-Klein mapping in the metastable region. *Phys. Rev. E*, 57:3797–3803, 1998.
- [175] J. Kertész. Existence of weak singularities when going around the liquid-gas critical point. *Physica A*, 161(1):58–62, 1989.
- [176] J. Adler and D. Stauffer. Search for liquid-gas transition above the critical temperature. *Physica A*, 175(2):222–228, 1991.
- [177] X. Campi and H. Krivine. Clustering in supercritical nuclear matter: a lattice-gas approach. *Nucl. Phys. A*, 620(1):46–54, 1997.
- [178] X. Campi, H. Krivine and N. Sator. Percolation line of self-bound clusters in supercritical fluids. *Physica A*, 296(12):24–30, 2001.
- [179] V. Bianco and G. Franzese. Critical behavior of a water monolayer under hydrophobic confinement. *ArXiv e-prints*, 2012.
- [180] T. B. Liverpool and S. C. Glotzer. Fixed-cluster acceleration algorithm for spin systems. *Phys. Rev. E*, 53:R4255–R4258, 1996.
- [181] G. Franzese. Cluster analysis for percolation on a two-dimensional fully frustrated system. *J. Phys. A-Math. Gen.*, 29(23):7367–7375, 1996.
- [182] R. Ravindra and R. Winter. On the temperature-pressure free-energy landscape of proteins. *Chem. Phys. Chem.*, 4(4):359–365, 2003.
- [183] P. L. Privalov. Cold denaturation of proteins. *Crit. Rev. Biochem. Mol. Biol.*, 25(4):281–305, 1990.
- [184] K. Goossens, L. Smeller, J. Frank and K. Heremans. Pressure-tuning the conformation of bovine pancreatic trypsin inhibitor studied by fourier-transform infrared spectroscopy. *Eur. J. Biochem.*, 236(1):254–262, 1996.
- [185] D. P. Nash and J. Jonas. Structure of the pressure-assisted cold denatured state of ubiquitin. *Biochem. Biophys. Res. Commun.*, 238(2):289–291, 1997.
- [186] D. P. Nash and J. Jonas. Structure of pressure-assisted cold denatured lysozyme and comparison with lysozyme folding intermediates. *Biochemistry*, 36(47):14375–14383, 1997.

- [187] F. Meersman, L. Smeller and K. Heremans. Pressure-assisted cold unfolding of proteins and its effects on the conformational stability compared to pressure and heat unfolding. *High Pressure Res.*, 19(1-6):263–268, 2000.
- [188] A. Pastore, S. R. Martin, A. Politou, K. C. Kondapalli, T. Stemmler and P. A. Temussi. Unbiased cold denaturation: low- and high-temperature unfolding of yeast frataxin under physiological conditions. *J. A. Chem. Soc.*, 129(17):5374–5375, 2007.
- [189] G. Hummer, S. Garde, A. E. García, M. E. Paulaitis and L. R. Pratt. The pressure dependence of hydrophobic interactions is consistent with the observed pressure denaturation of proteins. *Proc. Natl. Acad. Sci. USA*, 95(4):1552–1555, 1998.
- [190] F. Meersman, C. M. Dobson and K. Heremans. Protein unfolding, amyloid fibril formation and configurational energy landscapes under high pressure conditions. *Chem. Soc. Rev.*, 35:908–917, 2006.
- [191] M. Gross and R. Jaenicke. Proteins under pressure. *Eur. J. Biochem.*, 221(2):617–630, 1994.
- [192] H. S. Frank and M. W. Evans. Free volume and entropy in condensed systems iii. entropy in binary liquid mixtures; partial molal entropy in dilute solutions; structure and thermodynamics in aqueous electrolytes. *J. Chem. Phys.*, 13(11):507–532, 1945.
- [193] T. E. Creighton. Protein folding. *Biochem. J.*, 270(1):1–0, 1990.
- [194] N. Muller. Search for a realistic view of hydrophobic effects. *Accounts Chem. Res.*, 23(1):23–28, 1990.
- [195] K. A. T. Silverstein, A. D. J. Haymet and Ken A. Dill. A simple model of water and the hydrophobic effect. *J. A. Chem. Soc.*, 120(13):3166–3175, 1998.
- [196] S. A. Hawley. Reversible pressure-temperature denaturation of chymotrypsinogen. *Biochemistry*, 10(13):2436–2442, 1971.
- [197] L. Smeller. Pressure-temperature phase diagrams of biomolecules. *Biochim. Biophys Acta - Struct M.*, 1595(1-2):11–29, 2002.
- [198] F. Meersman, L. Smeller and K. Heremans. Protein stability and dynamics in the pressure-temperature plane. *Biochim. Biophys Acta - Proteins Proteom.*, 1764(3):346–354, 2006.

- [199] S. Kunugi, H. Yamamoto, M. Makino, T. Tada and Y. Uehara-Kunugi. Pressure-Assisted Cold-Denaturation of Carboxypeptidase Y. *B. Chem. Soc. Jpn.*, 72:2803–2806, 1999.
- [200] P. S. Pershan and J. Prost Landau theory of the reentrant nematic-smectic a phase transition. *J. Physique Lett.*, 40(2):27–30, 1979.
- [201] K. F. Lau and K. A. Dill. A lattice statistical mechanics model of the conformational and sequence spaces of proteins. *Macromolecules*, 22(10):3986–3997, 1989.
- [202] D. Mirejovsky and E. M. Arnett. Heat capacities of solution for alcohols in polar solvents and the new view of hydrophobic effects. *J. A. Chem. Soc.*, 105(5):1112–1117, 1983.
- [203] A. Geiger, A. Rahman and F. H. Stillinger. Molecular dynamics study of the hydration of lennard-jones solutes. *J. Chem. Phys.*, 70(1):263–276, 1979.
- [204] D. Van Belle and S. J. Wodak. Molecular dynamics study of methane hydration and methane association in a polarizable water phase. *J. A. Chem. Soc.*, 115(2):647–652, 1993.
- [205] B. Lee. Solvent reorganization contribution to the transfer thermodynamics of small nonpolar molecules. *Biopolymers*, 31(8):993–1008, 1991.
- [206] B. Madan and B. Lee. Role of hydrogen bonds in hydrophobicity: the free energy of cavity formation in water models with and without the hydrogen bonds. *Biophysical Chemistry*, 51(23):279–289, 1994.
- [207] J. L. Finney and A. K. Soper. Solvent structure and perturbations in solutions of chemical and biological importance. *Chem. Soc. Rev.*, 23:1–10, 1994.
- [208] L. E. S. de Souza and D. Ben-Amotz. Hard fluid model for molecular solvation free energies. *J. Chem. Phys.*, 101(11):9858–9863, 1994.
- [209] B. Lee and G. Graziano. A two-state model of hydrophobic hydration that produces compensating enthalpy and entropy changes. *J. A. Chem. Soc.*, 118(22):5163–5168, 1996.
- [210] P. De Los Rios and G. Caldarelli. Putting proteins back into water. *Phys. Rev. E*, 62(6):8449–8452, 2000.

- [211] G. Caldarelli and P. De Los Rios. Cold and warm denaturation of proteins. *J. Biol. Phys.*, 27(2-3):229–241, 2001.
- [212] G. Salvi, P. De Los Rios and M. Vendruscolo. Effective interactions between chaotropic agents and proteins. *Proteins*, 61(3):492–499, 2005.
- [213] P. Bruscolini and L. Casetti. Lattice model for cold and warm swelling of polymers in water. *Phys. Rev. E*, 61:R2208–R2211, 2000.
- [214] P. Bruscolini and L. Casetti. Model for the hydration of nonpolar compounds and polymers. *Phys. Rev. E*, 64:051805, 2001.
- [215] P. L. Makhatadze and G. I. Privalov. Energetics of protein structure. *Adv. Protein Chem.*, 47:307–425, 1995.
- [216] C. L. Dias, T. Ala-Nissila, M. Karttunen, I. Vattulainen and M. Grant. Microscopic mechanism for cold denaturation. *Phys. Rev. Lett.*, 100(11):118101–4, 2008.
- [217] A. Ben-Naim. Statistical mechanical study of hydrophobic interaction. I. Interaction between two identical nonpolar solute particles. *J. Chem. Phys.*, 54(3):1387–1404, 1971.
- [218] T. Yoshidome and M. Kinoshita. Hydrophobicity at low temperatures and cold denaturation of a protein. *Phys. Rev. E*, 79:030905, 2009.
- [219] P. G. Kusalik and G. N. Patey. The solution of the reference hypernetted-chain approximation for water-like models. *Mol. Phys.*, 65(5):1105–1119, 1988.
- [220] S. Matysiak, P. G. Debenedetti and P. J. Rossky. Role of hydrophobic hydration in protein stability: A 3d water-explicit protein model exhibiting cold and heat denaturation. *J. Phys. Chem. B*, 116(28):8095–8104, 2012.
- [221] K. Lum, D. Chandler and J. D. Weeks. Hydrophobicity at small and large length scales. *J. Phys. Chem. B*, 103(22):4570–4577, 1999.
- [222] P. R. ten Wolde and D. Chandler. Drying-induced hydrophobic polymer collapse. *Proc. Natl. Acad. Sci. USA*, 99(10):6539–6543, 2002.
- [223] P. Varilly, A. J. Patel and D. Chandler. An improved coarse-grained model of solvation and the hydrophobic effect. *J. Chem. Phys.*, 134(7):074109, 2011.

- [224] M. I. Marqués, J. M. Borreguero, H. E. Stanley and N. V. Dokholyan. Possible mechanism for cold denaturation of proteins at high pressure. *Phys. Rev. Lett.*, 91:138103, 2003.
- [225] J. Zhang, X. Peng, A. Jonas and J. Jonas. Nmr study of the cold, heat and pressure unfolding of ribonuclease a. *Biochemistry*, 34(27):8631–8641, 1995.
- [226] B. A. Patel, P. G. Debenedetti, F. H. Stillinger and P. J. Rossky. A water-explicit lattice model of heat-, cold- and pressure-induced protein unfolding. *Biophys. J.*, 93:4116–4127, 2007.
- [227] A. Chandra. Effects of ion atmosphere on hydrogen-bond dynamics in aqueous electrolyte solutions. *Phys. Rev. Lett.*, 85:768–771, 2000.
- [228] B. Hribar, N. T. Southall, V. Vlachy and K. A. Dill. How ions affect the structure of water. *J. A. Chem. Soc.*, 124(41):12302–12311, 2002.
- [229] H. A. Patel, E. B. Nauman and S. Garde. Molecular structure and hydrophobic solvation thermodynamics at an octane–water interface. *J. Chem. Phys.*, 119(17):9199–9206, 2003.
- [230] A. Nag, D. Chakraborty and A. Chandra. Effects of ion concentration on the hydrogen bonded structure of water in the vicinity of ions in aqueous nacl solutions. *J. Chem. Sci.*, 120(1):71–77, 2008.
- [231] D. Corradini and P. Gallo. Liquidliquid coexistence in nacl aqueous solutions: A simulation study of concentration effects. *J. Phys. Chem. B*, 115(48):14161–14166, 2011.
- [232] D. Schwendel, T. Hayashi, R. Dahint, A. Pertsin, M. Grunze, R. Steitz and F. Schreiber. Interaction of water with self-assembled monolayers: neutron reflectivity measurements of the water density in the interface region. *Langmuir*, 19(6):2284–2293, 2003.
- [233] T. R. Jensen, M. Ø. Jensen, N. Reitzel, K. Balashev, G. H. Peters, K. Kjaer and T. Bjørnholm. Water in contact with extended hydrophobic surfaces: Direct evidence of weak dewetting. *Phys. Rev. Lett.*, 90:086101, 2003.

-
- [234] S. Sarupria and S. Garde. Quantifying water density fluctuations and compressibility of hydration shells of hydrophobic solutes and proteins. *Phys. Rev. Lett.*, 103:037803, 2009.
- [235] T. Sumi and H. Sekino. Possible mechanism underlying high-pressure unfolding of proteins: formation of a short-period high-density hydration shell. *Phys. Chem. Chem. Phys.*, 13:15829–15832, 2011.
- [236] P. Das and S. Matysiak. Direct characterization of hydrophobic hydration during cold and pressure denaturation. *J. Phys. Chem. B*, 116(18):5342–5348, 2012.
- [237] R. Sarma and S. Paul . Effect of pressure on the solution structure and hydrogen bond properties of aqueous n-methylacetamide. *Chem. Phys.*, 407(0):115–123, 2012.
- [238] H. Li, H. Yamada and K. Akasaka. Effect of pressure on individual hydrogen bonds in proteins. Basic pancreatic trypsin inhibitor. *Biochemistry*, 37(5):1167–1173, 1998.
- [239] M. Doi and S. F. Edwards. *The Theory of Polymer Dynamics*. Oxford University Press, 1988.

Curriculum Vitae

Address

Valentino Bianco

Departament de Física Fonamental

Universitat de Barcelona

Martí i Franquès 1, 08028 Barcelona, Spain

Email: vbianco283@gmail.com

Personal data

Date of birth: 19th of February 1983

Place of birth: San Giuseppe Vesuviano (NA), Italy

Nationality: Italian

Education

- 20012005 Degree in Physics (general curriculum) at University of Naples Federico II.
Final work: Violation of CP-symmetry in non leptonic decays of K mesons.
Supervisor: Dr. Luigi Cappiello, Dr. Giancarlo D'Ambrosio.
- 2006-2009 Master degree in Physics, theoretical physics curriculum, at University of Naples Federico II.
Title of the thesis: Analysis of pairing mechanism of X chromosomes in tetraploid cells at onset of X inactivation.
Supervisor: Dr. Mario Nicodemi, Dr. Luca Peliti.
- 20102013 PhD in physics, University of Barcelona UB , Spain.
Project: Statistical Physics of Water in Hydrophobic Nano-Confinement and at Proteins Interfaces.
Supervisor: Dr. Giancarlo Franzese.

List of Publications

- G. Franzese, V. Bianco, S. Iskov, Water at interface with proteins, *Food Biophysics* 6, 186 (2011).
- V. Bianco, S. Iskov, G. Franzese, Effect of hydrogen bonds on protein stability, *Journal of Biological Physics* 38, 27 (2012).
- V. Bianco, G. Franzese, R. Ruberto, S. Ancherbak, Chapter: Water and anomalous liquids, in Book: *Varenna Proceedings of the 2010 Enrico Fermi School on Complex Systems*, edited by F. Mallamace and H. E. Stanley, Società Italiana di Fisica (2012).
- V. Bianco, A. Scialdone, M. Nicodemi, Colocalization of Multiple DNA Loci: a Physical Mechanism, *Biophysical Journal* 23, 2223 (2012).
- V. Bianco, O. Vilanova, G. Franzese, Confined water and critical behavior, to appear in *Proceedings of Barcelona Postgrad Encounters on Fundamental Physics*, (2013).
- V. Bianco, G. Franzese, O. Vilanova, Polyamorphism and polymorphism of a confined water monolayer: liquid-liquid critical point, liquid-crystal and crystal-crystal phase transitions, *Proceedings of Perspectives and Challenges in Statistical Physics and Complex Systems for the Next Decade: A Conference in Honor of Eugene Stanley and Liacir Lucena*.
- G. Franzese, V. Bianco, Water at biological and inorganic interfaces, accepted in *Food Biophysics* (2013).
- V. Bianco, G. Franzese, Critical behavior of a water monolayer under hydrophobic confinement, <http://arxiv.org/abs/1212.2847>, to be submitted to *Scientific Reports* (2013).
- V. Bianco, G. Franzese, The Widom line in water, to be submitted to *Journal of Physics: Condensed Matter*.
- V. Bianco, G. Franzese, Percolation in supercooled water, to be submitted.
- V. Bianco, G. Franzese, A water-polymer coarse grain model for elliptic shape of protein stability region, to be submitted.

Contribution at conferences**Talks**

- Structural Analysis of Supercooled Water at Interface with Proteins, Workshop on Self-Assembly, Barcelona, Spain, April 18-19 (2011).
- Strong confinement of a water monolayer induces 3D-like behavior, Barcelona Post-grad Encounters on Fundamental Physics, Barcelona, Spain, October 17-19 (2012).

Posters

- Cluster analysis approach to the phase transition of water in supercooled region, Jornada IN2UB, Barcelona, Spain, October 13 (2010).
- Percolative analysis of nanoconfined supercooled water, XVII Congreso de Física Estadística (FisEs 2011), Barcelona, Spain, June 2-4 (2011).
- Phase diagram of supercooled water nanoconfined between hydrophobic walls: cluster analysis, CECAM Workshop on Models for bulk, confined water and aqueous solutions upon supercooling: State of the art and future perspectives in understanding water anomalies by computer simulations, Lausanne, Switzerland, July 4-6 (2011).
- Strong confinement of a water monolayer induces 3D-like behavior, Complexicat.CAT, Barcelona, Spain, May 2-4 (2012).
- Strong confinement of a water monolayer induces 3D-like behavior, XXIII Sitges Conference On Statistical Mechanics Understanding and Managing Randomness in Physics, Chemistry and Biology, Sitges, Spain, June 4-8 (2012).
- Phase diagram of confined water, Gordon Research Seminar Water & Aqueous Solutions, Holderness, USA, August 11-12 (2012).
- Phase diagram of confined water, Gordon Research Conference Water & Aqueous Solutions, Holderness, USA, August 13-18 (2012).
- Critical behavior of a water monolayer under hydrophobic confinement, workshop WaterSpain 2013, Zaragoza, Spain, February 8-9 (2013).
- Effect of confinement in supercooled water, workshop Joint CRM-Imperial College School and Workshop in Complex Systems, Bellaterra, Spain, April 8-13 (2013).